NASA/CR—1998-206594

Study of a Wake Recovery Mechanism in a High-Speed Axial Compressor Stage

Dale E. Van Zante
Iowa State University, Ames, Iowa

Prepared under Grant NAG3–1302

National Aeronautics and
Space Administration

Lewis Research Center

February 1998

Acknowledgments

The author wishes to express his gratitude to Dr. Ted Okiishi for the opportunity to do this research project at NASA and for being a great mentor and friend. Also a huge thankyou to all the people at NASA Lewis that made this project possible: Drs. Tony Strazisar and John Adamczyk for guidance, technical advice, and many hours of their time in making this project a success, to Mr. Jerry Wood for all of his insight and suggestions in data analysis, to Dr. Ken Suder for invaluable assistance with the laser anemometer system, to Mark Celestina and Richard Mulac for assistance with the numerical simulations, and to all of the people that actually keep the rig and the electonics running, Mike McGhee, Mike Goin, Dave Williams, Bob Gronski, Glenn Christman, and Rob Bruckner. And finally I would like to acknowledge the NASA Lewis Research Center which provided the facilities and funding for the program under grant NAG3–1302.

Trade names or manufacturers' names are used in this report for identification only. This usage does not constitute an official endorsement, either expressed or implied, by the National Aeronautics and Space Administration.

Copyright 1997 by Dale E. Van Zante. All rights reserved.

Available from

NASA Center for Aerospace Information
800 Elkridge Landing Road
Linthicum Heights, MD 21090-2934
Price Code: A08

National Technical Information Service
5287 Port Royal Road
Springfield, VA 22100
Price Code: A08

TABLE OF CONTENTS

LIST OF FIGURES

LIST OF TABLES

ABSTRACT

This work addresses the significant differences in compressor rotor wake mixing loss which exist in a stage environment relative to a rotor in isolation. The wake decay for a rotor in isolation is due solely to viscous dissipation which is an irreversible process and thus leads to a loss in both total pressure and efficiency. Rotor wake decay in the stage environment is due to both viscous mixing and the inviscid strain imposed on the wake fluid particles by the stator velocity field. This straining process, referred to by Smith (1993) as recovery, is reversible and for a 2D rotor wake leads to an inviscid reduction of the velocity deficit of the wake.

A model for the rotor wake decay process is developed and used to quantify the viscous dissipation effects relative to those of inviscid wake stretching. The model is verified using laser anemometer measurements acquired in the wake of a transonic rotor operated in isolation and in a stage configuration at near peak efficiency and near stall operating conditions. Additional insight is provided by a time-accurate 3D Navier Stokes simulation of the compressor stator flow field at the corresponding stage loading levels. Results from the wake decay model exhibit good agreement with the experimental data. Data from the model, laser anemometer measurements, and numerical simulations indicate that for the rotor/stator spacing used in this work, which is typical of core compressors, rotor wake straining (stretching) is the primary decay process in the stator passage with viscous mixing playing only a minor role. The implications of these results on compressor stage design are discussed.

1. INTRODUCTION

One of the primary goals of current compressor design is to achieve high efficiency and pressure ratio using fewer more highly loaded stages. Although stages can be designed with existing tools, an improved understanding of the flow field could lead to reduced effort and increased accuracy of the design process and development of better computational tools. Additionally, the performance of compressors and sophistication of analysis tools for compressors have reached a level such that less well understood flow mechanisms are gaining importance to designers. The impact on compressor performance of many of these mechanisms, such as blade row interactions, is not typically addressed in current design systems. Although early in compressor research attempts were made to quantify the impact of these interactions (for example Kemp and Sears, 1956), measurement and computational methods have only recently advanced to an extent to allow a more definitive analysis of these mechanisms.

There are many phenomena in the category of unsteady flow and bladerow interaction effects. See Hathaway (1986) for an excellent overview of a wide range of unsteady flow effects and bladerow interaction effects. The discussion which follows will focus on a specific phenomenon which results from blade rows moving relative to each other: the impact of a downstream stator row on the decay of rotor wakes. To introduce the different aspects from which to study this phenomenon the discussion is organized into four topic areas: bladerow interaction effects, rotor wake decay, rotor wake transport, and rotor wake stretching/recovery. Before the detailed discussion of these topic areas, a few comments will be made to clarify their inter-relationships, since their relation to each other may not be entirely clear to the reader.

The motivation for this report comes from observations that bladerow interactions do affect compressor performance by somehow altering the losses that occur relative to isolated blade row losses. One of the losses that affects compressor performance is the rotor wake mixing loss which occurs downstream of the rotor trailing edge. Much work has been done to pre-

dict rotor wake decay and its associated mixing loss with the assumption that the mixing loss can be determined by treating the rotor as an isolated blade row. In a stage environment, it is known that the rotor wakes are chopped and transported through the downstream blade row. Early research efforts assumed that the rotor wake transport which occurs in this downstream blade row only redistributes losses and does not have any influence on the rotor wake mixing loss. A more recent concept is that the rotor wake stretching which occurs due to the wake transport within a stator does lead to a reversible reduction of velocity gradients and thus mixing losses, known as recovery. The focus of the current research effort is the study of rotor wake recovery for a viscous compressible flow in a high-speed compressor stage.

1.1 Interaction Effects

The effects of bladerow interactions on compressor performance were noted in early compressor measurements. Smith (1970) in a study of the performance of a four-stage low-speed compressor found that, for a series of tests with different aspect ratio blades, peak pressure rise correlated with tip clearance/staggered spacing ratio and axial gap/spacing ratio. He suggested that more information on the effects of axial gaps is needed to establish why deviation angles and loss coefficients are apparently lower when axial gaps are small. He speculated that the cause was the circumferential variation of total pressure caused by the downstream blade row imposing non-uniform back pressure on the upstream rotor.

In compressor design, interaction effects are dealt with by empirical means often without a clear knowledge of underlying mechanisms. Koch and Smith (1976) again mention blade row interaction as having a performance impact. A downstream blade row moving relative to an upstream row was thought to reduce static pressure in regions of low axial velocity such as thick wakes in the casing boundary layer. This increases the velocity for the same total pressure, but also increases total pressure by reducing losses thus enhancing the velocity increase and reducing the boundary layer thickness. Although the mechanisms were not understood, the importance of the interactions to accurate performance predictions was considered important enough to attempt a correlation. The report contains an empirically generated curve which relates the change in boundary layer displacement thickness to axial gap/tangential spacing ratio. Additionally the report authors speculate that higher unsteadiness, which impacts wake

growth, could be totally/partly responsible for the performance improvement instead of the boundary layer thinning arguments. The important mechanism for the performance impact is unclear.

On a somewhat different line of thinking, Smith (1966) proposed an interaction mechanism which would reduce wake mixing loss in a reversible way and thus improve performance. This mechanism occurs due to a wake being stretched in the downstream blade row due to the relative motion and loading of the downstream row. This work is mentioned here in the context of interaction effects and will be discussed in more detail later.

Advances in measurement and computational methods now allow more direct observation of interactions. Early laser anemometer measurements by Ding (1982) suggested that there is a high level of unsteadiness in the rotor/stator gap. He noted violent flow accelerations and deflections in a short axial distance in the rotor/stator gap of a high speed compressor. Only two axial positions were measured with three circumferential points at each position so the data were too sparse to draw any further conclusions. These measurements hinted at the strong wake/blade interactions present in high-speed closely-coupled machines.

Williams (1988) acquired laser anemometer measurements in a high speed multistage compressor. The measured velocity downstream of a stator row showed the influence of the downstream rotor and the upstream rotor which had a different blade count. Using FFT techniques Williams extracted additional information about hardware related periodicities in the flow. Performance impact was not assessed in the paper, but the measurements clearly show the extent of bladerow interactions in a multistage machine.

Adamczyk et al. (1996b) used steady and unsteady numerical simulations to study the effects of wake induced unsteady flows on blade row performance and the wake rectification process. Wake rectification refers to the attenuation of a wake velocity deficit by mechanisms other than viscosity. Major performance differences were found between a rotor operating in isolation and a rotor operating downstream of a stator when the rotor had the same time average inlet flow condition. Use of a mixing plane in the stator/rotor gap improved agreement between the steady rotor simulation and the unsteady rotor simulation. Adamczyk's average passage model which includes the deterministic stress fields of surrounding blade rows provided far better agreement with the full unsteady rotor calculation. A dynamic wake rectifica-

tion process was also identified which occurs as the wake convects past the leading edge of the downstream rotor. This numerical study showed that interactions are important to predicting compressor performance and need to be correctly modeled.

The above investigations all show either directly or indirectly the presence and possible impact of interaction effects. In general most of the thinking about wake mixing losses considered the wakes of isolated blade rows. Along that line of thinking a brief summary of turbomachinery wake decay research is presented next.

1.2 Wake Decay

Wake decay by viscous dissipation results in the accrual of mixing loss and is therefore an important contributor to loss production. However, all of the wake decay work discussed below deals with wake decay in the absence of a downstream blade row moving relative to the wake generating row.

Several studies have considered the decay of wakes downstream of rotors or cascades of cambered airfoils. Kool and Hirsch (1982) developed a scheme for rotor wake decay prediction. They postulated the presence of a separation bubble at the trailing edge creating a free stagnation point that induces a pressure gradient which effects wake decay. The decay of axial and tangential velocity is based on an assumed profile shape and an eddy viscosity concept. The agreement of the model with available experimental data was fair.

Raj and Lakshminarayana (1973) measured the far and near wake of a plane cascade of airfoils to determine the mean velocity, turbulence intensity, and Reynold's stress profiles of the wakes. They found that the wake is asymmetrical past 3/4 of a blade cord downstream and that the decay of the defect is strongly dependent on the wake edge velocity. The decay rate of the wake defect was slower than that of a flat plate wake at zero incidence.

Hobbs et al. (1982) measured a plane cascade of airfoils and used the data to improve the computation of airfoil wakes with the intent of better loss predictions. A displacement surface determined from experimental measurements was added to the trailing edge of the airfoil in the computation to alter the trailing edge conditions of the computation. This was an attempt to adjust the computation to achieve a more accurate wake profile shape prediction. Again, the airfoil trailing edge conditions were important to predicting the wake shape and thus the loss

predicted due to wake mixing.

Accurate prediction of turbomachine near wake decay is difficult because wake decay is highly dependent on the boundary layer condition near the blade trailing edge and this in itself is difficult to measure or predict (see also Denton (1993)). Investigators have concentrated on predicting the correct wake profile so that an accurate mixing loss could be calculated and charged to that blade row.

All of the above studies considered wake decay without the presence of a downstream blade row. This assumes that the presence of a downstream blade row does not have an effect on the wake mixing loss. Although the research efforts discussed next still deal with wakes in the absence of a downstream blade row, they do consider the effects of pressure gradients and/ or curvature which begin to mimic some of the effects that a downstream blade row may have on an upstream blade row wake.

The effects of curvature and pressure gradient on a small defect wake were measured by Nakayama (1987) in a low speed wind tunnel. Small perturbations to the potential flow were found to significantly change the strain field of the small defect wake so that shear strain was no longer dominant. This occurred because viscous wake decay is dictated by shear stress which is proportional to the velocity defect squared and can be overcome by pressure or inertia forces which are proportional to the absolute velocity squared. The findings suggest that processes such as flow turning and pressure gradients in the stator could have large impacts on rotor wake decay.

Denton and Cumpsty (1987) considered the effect of downstream conditions on the mixing loss of a wake. It is shown that entropy generation during mixing greatly depends on the velocity at the point of mixing and entropy generation is greatly reduced by accelerating the wake prior to mixing. The trends of this process are not highly influenced by compressibility. The relevance to unsteady mixing in a downstream blade row was not clear but the authors suggest that the decelerating flow in a compressor might result in increased losses. The process of wake stretching in a stator passage was not considered by the authors in making this statement.

Denton (1993) revisits the topic of wake mixing more extensively. The loss associated with wake mixing is dependent on the velocity and conditions at which the wake mixes.

Accelerating a wake isentropically and then mixing it is shown to decrease the mixing loss coefficient while an isentropic deceleration and then mixing increases loss. The overall benefit of accelerating a wake prior to mixing will be affected by viscous dissipation of the wake which is occurring concurrently with the pressure gradient effects.

For a control volume approach to mixing the exact mechanisms of mixing need not be known to calculate the correct loss. Denton (1993) performed a viscous numerical calculation of a compressor cascade for three cases for which the blade boundary layer and trailing edge conditions were held constant, but the area downstream of the cascade was changed by 0% and +/- 25%. The calculation showed about one third of the total loss occurred downstream of the trailing edge. The change in area during mixing only affected losses by +/- 5%. A decrease in area would correspond to an accelerating flow and stretching of the wake before mixing and thus yields a decrease in losses. However, the current study will show that the wake stretching in real machines is larger than the amount implied by Denton's study, thus the reduction in mixing loss due to wake stretching is potentially greater, depending on viscous effects, than the 5% considered here.

Hill et al. (1963) studied the effect of pressure gradient on the decay of turbulent wakes. Wakes in adverse pressure gradients decay more slowly and there is a critical adverse pressure gradient above which the wake grows instead of decaying. Wakes in favorable pressure gradients decay more rapidly. The work of Hill et al. is used extensively in the development of the wake decay model in the present effort and will be discussed in detail later.

Wake transport in the stator is discussed next in the context that wake transport only redistributes losses.

1.3 Wake Transport

Kerrebrock and Mikolajczak (1970) used a kinematic analysis to look at the influence of upstream rotor wakes on the flow field of a downstream stator row in a compressor stage. The rotor wake fluid has a lower relative velocity than the surrounding free stream fluid. From velocity triangle arguments it can be shown that in the stator passage the rotor wake fluid will have a drift velocity toward the stator pressure surface relative to the free stream fluid. As the rotor wakes are chopped by the stator row, the higher total temperature rotor wake fluid drifts

toward and piles up on the stator pressure surface and leads to circumferential non-uniform total temperature distribution at the stator exit. Using these wake drift ideas, rotor performance was inferred from measurements downstream of the stator row. This model considers only the convective transport of wakes.

The kinematic model does not account for other unsteady effects such as the effect of the fluctuating static pressure on the total pressure redistribution as noted by Mikolajczak (1975) in a survey publication. Static pressure changes are expected to be largest near the blade surfaces such that large total pressure changes should appear in these regions. These changes have been observed in rotating rigs but are usually ignored. Mikolajczak (1975) noted that large changes in total pressure relative to the stator inlet plane were measured at the third stage stator exit near the stator surfaces of a highly loaded three stage compressor. Unsteady flow thus impacts losses in downstream blade rows and can also redistribute losses. More work to understand the importance of unsteady wake transport, potential field interactions and wake mixing is needed before the accurate prediction of the behavior of closely spaced compressors is possible.

Unusual total pressure distributions downstream of the second stage of a two stage research compressor were also observed by Tweedt et al. (1985). The distributions were explained by the interaction of the first stage stator and the second stage rotor using the transport ideas of Smith (1955,1966) and Kerrebrock and Mikolajczak (1970).

There are now some measurements of wake transport in the stage environment. Laser anemometer measurements of the stator flow field of a high-speed fan stage by Hathaway et al. (1987) and Hathaway (1986) directly show the transport of wakes in the stator. They found the kinematics of wake transport are largely controlled by the mean potential flow field and the separation distance between wake segments exiting the stator passage is predicted well by linear disturbance theory. There were also indications that rotor wake chopping by the stator promotes mixing. The stage was loosely coupled for noise reasons so the rotor wakes were very mixed out before entering the stator row. It is not clear what to expect from a close coupled stage where the rotor wakes are less mixed when entering the stator row.

Stauter et al. (1991) used laser anemometry to measure rotor wake behavior in the second stage of a two-stage low-speed research compressor. The compressor had axial gaps much

larger than would be used in production machines to allow detailed measurements. Measurements were acquired between the second rotor and second stator and also downstream of the second stator. Strong interactions between the rotor wakes and the stator potential field were noted. Wake decay was rapid in the rotor/stator gap but the authors still saw a significant rotor wake enter the stator passage. An exponential fit of the wake decay fit the data well but the authors questioned how widely applicable the results were. High unsteadiness was also observed in the stator wake. This was attributed to the stator blade interfering with the wake decay and to the upstream rotor wakes gathering in the stator boundary layer because of wake drift. The authors concluded that interactions were strong, significant, and likely to be stronger in machines with closer axial spacing.

Poensgen and Gallus (1990) studied the decay of wakes from a cylindrical rod rotor through midpitch of an annular stator cascade. The rod wake decay was measured first in isolation. The decay of the rod wakes was markedly different in the stage environment in that the decay of the wake velocity deficit was faster. The more rapid decay was attributed to the accelerating flow at the inlet to the stator passage and not to wake stretching. They did not consider the effect of their finding on loss.

The above research works dealt with the transport of wakes and/or the redistribution of losses due to the unsteady flow. The efforts discussed below address the impact of wake transport on wake decay.

1.4 Wake Stretching/Recovery

Smith (1966) proposed a mechanism for wake attenuation by a non-viscous and thus reversible means. A wake is chopped by a downstream blade row and a segment of mass of the wake is tracked. Smith considered the case of a compressor stator wake being chopped by a rotor. To illustrate this he used a stream of dye to represent the stator wake as shown in Figure 1 from his paper. The stream of dye is chopped by the rotor and the dye segments are rotated and stretched in the rotor passage. Smith postulated that this stretching process would lead to a reduction of the wake deficit as follows. If the fluid is considered 2D, incompressible, and inviscid, the vorticity of each fluid particle is constant by Kelvin's theorem. The wake segment is stretched in the downstream blade passages shown in Figure 2, but the circulation around

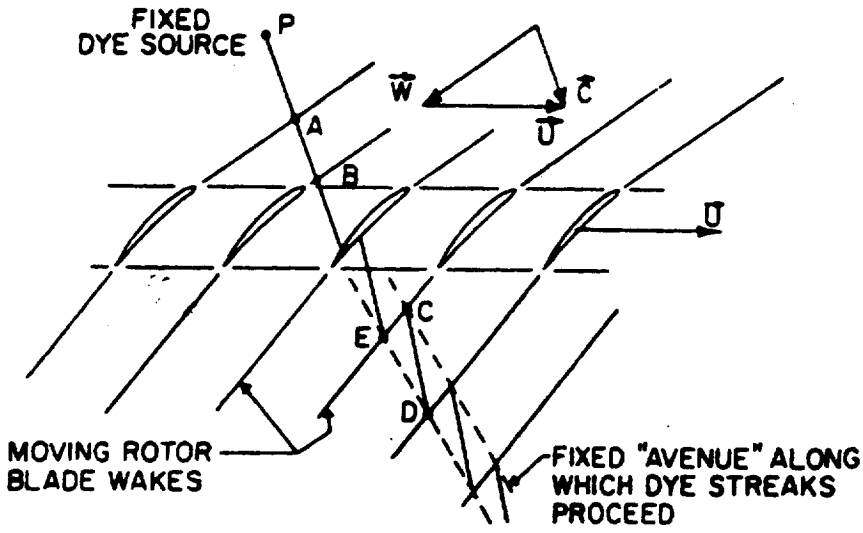

Figure 1. Dye source used to illustrate chopping of a stator wake by a downstream rotor (from Smith 1966).

the contour C is constant as the contour length increases. When the constant value of circulation is combined with mass conservation, one finds that the velocity difference between the wake and free stream decreases in inverse proportion to the wake length. Thus, as the wake is stretched the wake deficit is attenuated. The process is called wake recovery and is defined as the attenuation (or amplification) of the wake velocity profile by processes other than viscous dissipation occurring inside a blade row.

Smith (1993) related wake recovery to performance benefit and found that ingesting wake fluid through the propulsor or rotor reduced losses. He concluded that to obtain the maximum recovery benefit the propulsor should ingest the viscous wake before it dissipated significantly. He suggests that this could explain why multistage turbomachinery has higher performance with closer axial spacing.

Deregal and Tan (1996) used a first of a kind numerical simulation to investigate the link between unsteady flow induced by the rotor wakes and the steady state compressor performance as first proposed by Smith. A time accurate, 2D, incompressible simulation was used for geometries representative of modern compressors. The results showed that mixing loss was reduced due to wake stretching in the stator passage. Also, overall pressure rise was larger

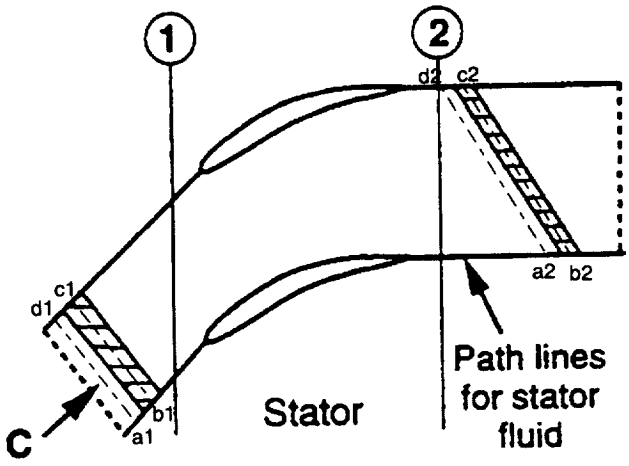

Figure 2. Overall kinematics of rotor wake in stator passage (from Deregal and Tan, 1996).

due to the reduction of unsteady kinetic energy in the stator passage.

Adamczyk (1996) performed an analytic investigation of the recovery of the total pressure deficit of a wake by a reversible process which is unsteady and associated with the kinematics of wake transport. The benefits of wake recovery were estimated from linear theory assuming 2D incompressible inviscid flow. Results from the computations showed that recovery can reduce wake mixing loss by 70%.

All of the above wake recovery work was done using incompressible and inviscid assumptions. The benefit of wake recovery in turbomachines of practical interest must be determined with information from a viscous compressible flow which is the goal of the present investigation.

1.5 Motivation for Current Project

The intent of this work is to assess the role of wake recovery in the decay of a rotor wake in the stator passage of a high speed compressor stage. The decay of a high-speed rotor wake in isolation and in a stage environment is measured to assess the impact of a stator blade row on rotor wake mixing in a compressible viscous flow. In addition, a 3D time accurate Navier Stokes simulation of the stator passage is done to aid in the interpretation of the data and in establishing errors due to unmeasured effects. The work of Adamczyk puts an upper bound on the benefits of wake recovery. In a real machine the benefits of wake recovery will be reduced

due to viscous dissipation and compressibility effects. The measurements are used to identify the role of viscosity and to establish the near wake decay and the inlet wake profile to the stator passage. A model for the rotor wake decay in the stator passage which includes the effects of wake stretching and viscosity is also developed based on the work of Hill et al. Results from the model are compared to experimental data to verify the model. The model is then used to assess the impact of viscosity on wake recovery and to draw conclusions related to stage design.

This dissertation is organized as follows. Chapters 2 and 3 discuss the research facility and some details of the experimental data acquisition. Chapter 4 introduces the numerical codes used to simulate the stage. Chapter 5 contains the development of the wake stretching and wake decay models. Also included is background on quantifying wake decay and mixing loss using the kinetic energy of the wake when treated as a disturbance relative to the free stream. Chapter 6 presents the data and analysis including first a discussion of the importance of effects which are not included in the model. Results from the model are presented and compared to data. Chapter 7 discusses the implications of the research results for stage design.

2. RESEARCH FACILITY

The experimental data in this dissertation was acquired in the single-stage axial-flow compressor test facility of the National Aeronautics and Space Administration (NASA) Lewis Research Center. This chapter describes the test facility, research compressor stage, the laser fringe anemometer (LFA) system, and the steady-state instrumentation.

This facility and measurement systems are described extensively in previous reports. The reader is referred in the text to these reports if greater detail is required.

2.1 Compressor Test Facility

Figure 3 shows a schematic diagram of the single stage test facility. The facility uses an open loop airflow scheme. Atmospheric air is drawn into the facility from an inlet on the roof. The air passes through a thin plate orifice flow measuring station, through the inlet butterfly valve and into the plenum chamber. The seed injection nozzles for the laser anemometer system are located in the vertical inlet piping just ahead of the plenum chamber. The air is accelerated through a nozzle into the compressor test section. The air exits the test section through a sleeve throttle valve which is located inside of the collector. This throttle valve is used to set the compressor mass flow. The air is then cooled and exhausted back to the atmosphere. The compressor is driven by a 3000 hp electric motor with a variable frequency power supply. The compressor speed is controllable from 1760 rpm to 20,000 rpm.

2.2 Research Compressor Stage

The research compressor stage hardware consisted of blading which was designed at NASA Lewis as the inlet stage to a core compressor. Four inlet stages were originally designed and were designated stages 35, 36, 37, and 38. Stages 36 and 38 are high aspect ratio blading and are not representative of current blading design practice. Stages 35 and 37 have a rotor aspect ratio and pressure ratios which are representative of current blade design practice.

The original test stage, Stage 37, consisted of NASA Rotor 37 and NASA Stator 37. Early

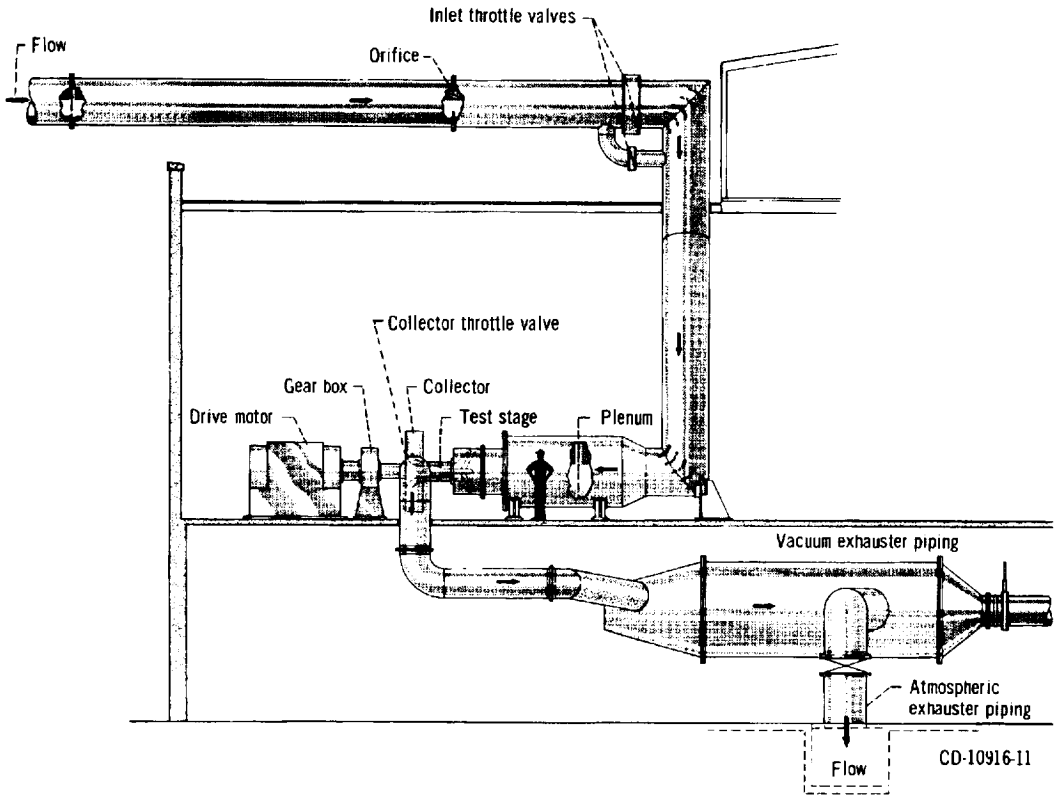

Figure 3. Schematic diagram of the NASA Lewis singe-stage compressor test facility.

in the test program, Rotor 37 was damaged due to the implosion of an optical access window. Stator 37 had been modified to allow optical access for detailed flow field measurements. In order to retain Stator 37, NASA Rotor 35, which uses the same flow path contour, was substituted for Rotor 37. However, Rotor 35 has a lower design pressure rise than Rotor 37. Due to the lower static pressure rise, there was a possibility that Stator 37 could not pass the mass flow without choking. To avoid this potential problem, the stage was operated at 80% design speed and the Stator 37 blades were re-staggered to increase the stator throat area. An Average Passage Code analysis (Adamczyk 1985) of Rotor 35/Stator 37 indicated that a 4.0 degree re-stagger open (decrease the setting angle) would give the best stage performance and the stator blades were installed with this re-stagger. A complete description of the aerodynamic design and geometry of Rotor 35 and Stator 37 is contained in Refs. (Reid and Moore, 1978a) and (Reid and Moore, 1978b) respectively.

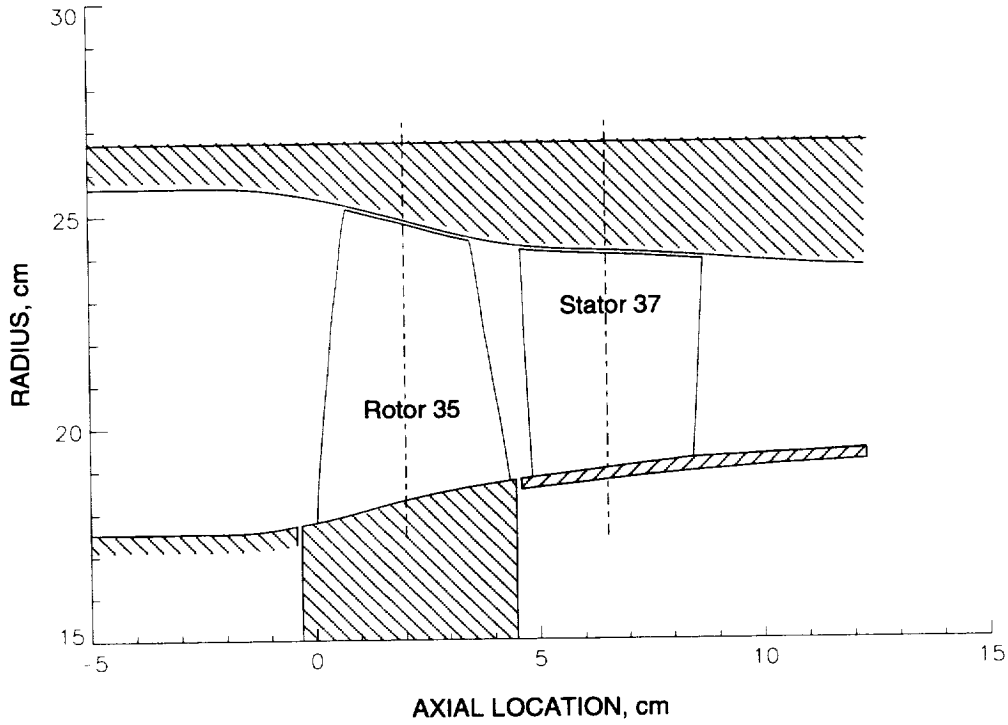

Figure 4. Meridional view of compressor flow path.

Figure 4 shows a meridional view of the compressor stage. This is a closely coupled transonic stage. The relative flow velocity is supersonic at the rotor blade tip and subsonic at the rotor blade hub. Table 1 contains a summary of the geometric stage design parameters.

The original Stator 37 blades are mounted from a trunion to the compressor casing. To gain optical access to the stator flow field, the four stator blades which are visible through the optical access window were redesigned to mount from the compressor hub as the stator is shown in Figure 4. For structural reasons it was necessary to thicken the profile of the hub mounted blades near the hub. Four "guard blades" were also built with the thicker profile but were casing mounted like the original Stator 37 blades. Two of these guard blades were mounted on either side of the hub mounted blades. This ensures that the rotor flow field has adjusted to the differing stator blade back pressure and is periodic within the hub-mounted blades. The flow field periodicity is discussed in Appendix A.

Because the rotor tip clearance gap has an impact on compressor performance, efforts were made to maintain nearly the same gap, within practical limits, for the rotor only and stage tests. The rotor tip clearance gap was measured with a Rotodata touch probe. The rotor

Table 1: Summary of stage design parameters.

	Rotor 35		Stator 37	
Number of blades	36		46	
Blade section profile	Multiple Circular Arc		Double Circular Arc	
Stack point	2.03 cm		6.57 cm	
Aspect ratio	1.19		1.26	
	Hub	Tip	Hub	Tip
Blade aero chord	5.622	5.609	3.834	4.273
Blade axial chord	4.118	2.610	3.571	4.059
Solidity	1.765	1.292	1.474	1.296
	Inlet	Exit	Inlet	Exit
Hub radius	17.78	18.72	18.84	19.24
Hub/tip radius ratio	0.70	0.76	0.78	0.80

tip clearance gap was 0.79 mm for the rotor only case and 0.69 mm for the stage case.

2.3 Laser Anemometer System

Detailed flow measurements were acquired in the compressor stage with a two-channel laser fringe anemometer (LFA) system. The LFA system measures axial and tangential velocities simultaneously. Suder (1996) assembled the system from current state of the art optical components.

The LFA measurement volume is created by crossing two laser beams at a point in space. At the crossing point, an interference or fringe pattern is formed. The fringe spacing is determined from the optical configuration and the wavelength of the laser light. Upstream of the compressor, the flow is seeded with very small particles. These particles scatter light from the fringe pattern as they pass through the measurement volume. The LFA system collects the scattered light and determines the velocity of the particle from the Doppler frequency of the scattered light and the fringe spacing. A brief description of the optical access window, LFA

system, traverse mechanism, and flow seeding follow. For a detailed LFA system description, see Suder (1996) and for more detail on LFA application to turbomachinery, see Hathaway (1986) and Strazisar (1985).

A large window, which conformed to the 3D shroud contour provided optical access to the flow field from one chord upstream of the rotor to one chord downstream of the stator. Figure 5 shows the casing cutout for the window with LFA system moved into its measurement position. The window is 2.54 mm thick alumina silica glass and is molded to the 3D flow path contour in a process described by Verhoff (1992) so that the correct rotor tip clearance gap is maintained when the window is installed in the casing.

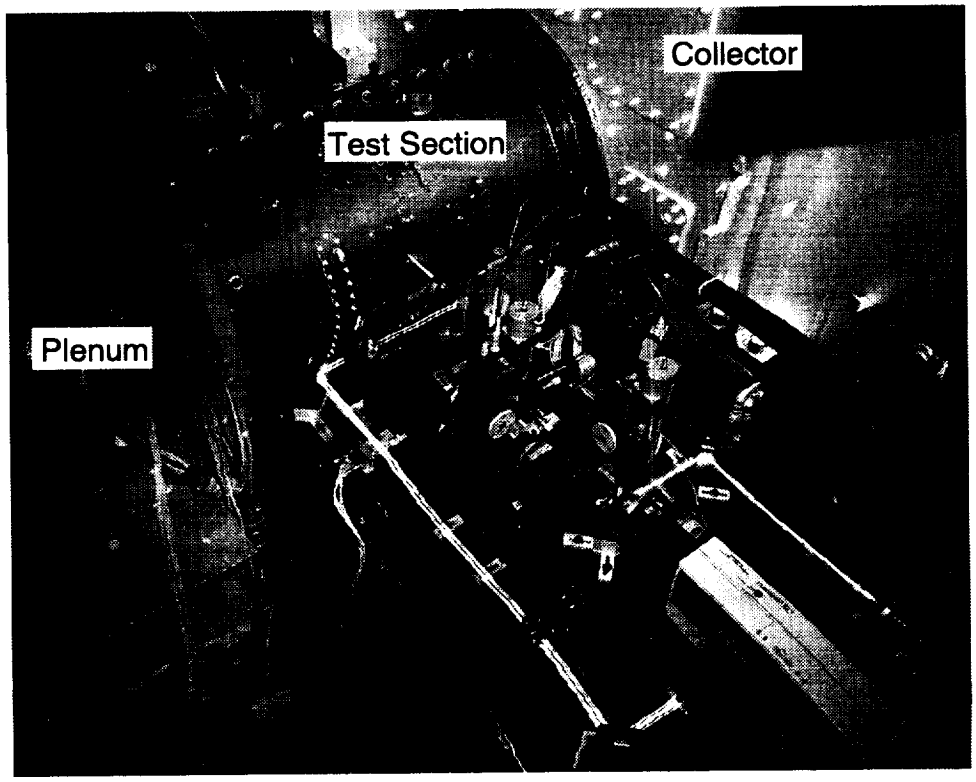

Figure 5. Laser fringe anemometer system in its measurement position.

Due to space and optical access limitations, the LFA optics layout was designed specifically for this application as shown in Figure 6. The system is 'powered' by a 6 watt Argon-ion laser that emits a single multi-colored beam in the visible spectrum. The beam is directed through a collimator which reduces the divergence of the beam and locates the minimum

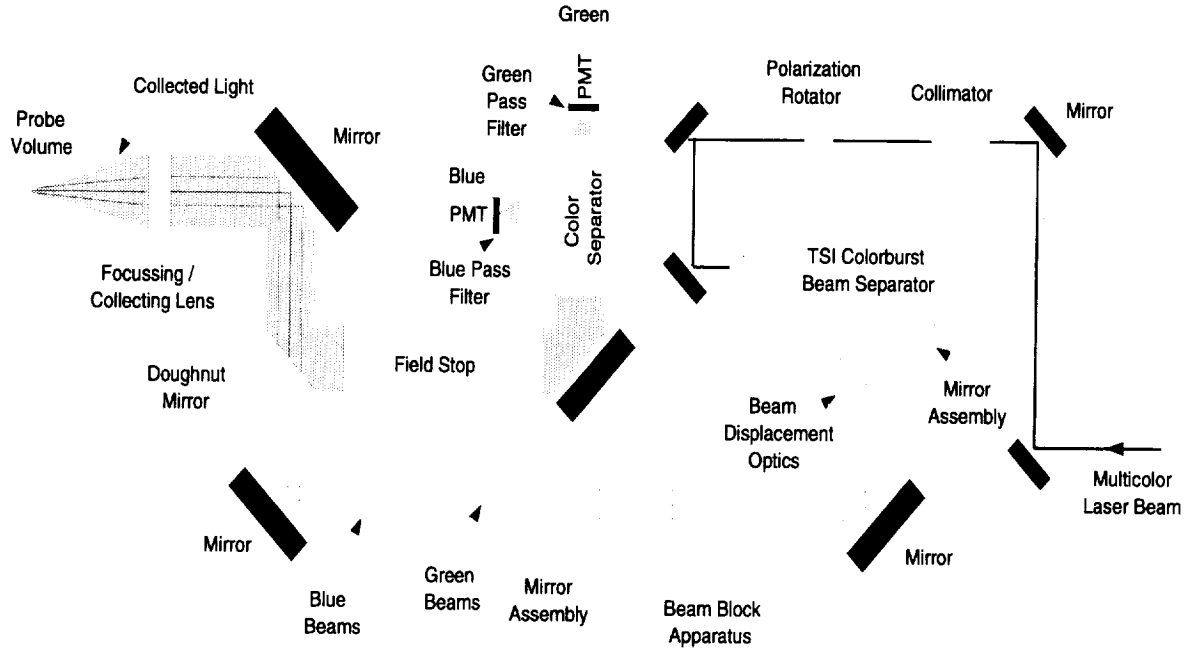

Figure 6. Schematic of optical components layout for the LFA system (Suder 1996).

beam waist diameter at the probe volume. Next the polarization rotator adjusts the beam polarization direction such that the TSI Colorburst beam separator works at its maximum efficiency.

The Colorburst contains on acousto-optic cell (Bragg cell) and a color separator. The Bragg cell generates two multi-colored beams; one with a 40 MHz frequency shift and the other unshifted. The frequency shift either adds to (if the shift is against the flow direction) or subtracts from (if the shift is with the flow direction) the measured Doppler shift frequency. This allows flow reversals to be detected. Both the shifted and unshifted beams are then passed through dispersion prisms which separate the beams into blue (488 nm), green (514.5 nm), and violet (476.5 nm) wavelengths. Only the blue and green beams were used in this case to measure axial and tangential velocity respectively. Since the Colorburst is designed for use with fiber optic components, the output beams are passed through a series of optics that space each pair of beams 22 mm apart so that conventional optics can be used for the remainder of the system.

The four beams pass through a beam block apparatus which is used for system alignment and checkout and then into a mirror assembly. The mirror assembly reverses the shift direction

of the vertical (green) beams without changing the shift direction of the blue beams. The change is necessary because of the tangential velocity direction in the compressor stage. The beams are passed through a pierced (doughnut) mirror and directed through the focussing/collection lens.

The focussing lens is a short focal length f2 lens which causes all four beams to cross at the lens focal point thus forming the measurement volume. Because of the short focal length lens and masks in the collection optics, the effective length of the measurement volume (probe volume) is reduced. The probe volume has an effective length of 0.5 mm, which is less than 1% of blade span, and a diameter of 60 micrometers.

The focussing lens also acts as the collection lens which captures light scattered by particles passing through the probe volume and directs the collected light back along the axis of the transmitted beams. This is known as backscatter collection. The collected light is reflected into the field stop by the pierced mirror.

The field stop allows only the light coming from the focussing lens focal point to pass. The field stop contains a mask and pinhole which effectively shorten the length of the probe volume. The collected light then enters a color separator which separates the blue and green collected light. The blue light is focussed through a pinhole and blue pass filter onto a photomultiplier tube (PMT). The green light is focussed through a pinhole and green pass filter and onto another PMT. The PMTs convert the light to an electrical signal which is passed to the laser anemometer counter processor and data acquisition computer.

The LFA system is mounted onto a three axis traverse system, shown in Figure 7, which allows positioning of the probe volume at any point and orientation in the compressor flow field. The optics breadboard and laser are mounted onto three positioning tables which move the probe volume in the axial, radial, and vertical directions to within an uncertainty of 0.02 mm. The focussing lens and final turning mirror are mounted on a goniometric stage which allows movement of the probe volume in an arc in the radial/circumferential plane (the plane perpendicular to the compressor shaft axis).

For the rotor only measurements, the probe volume need only be traversed in the radial and axial directions. Each velocity measurement is tagged with the rotor angular position using a shaft angle encoder as described by Hathaway (1986). The rotor sweeping by the

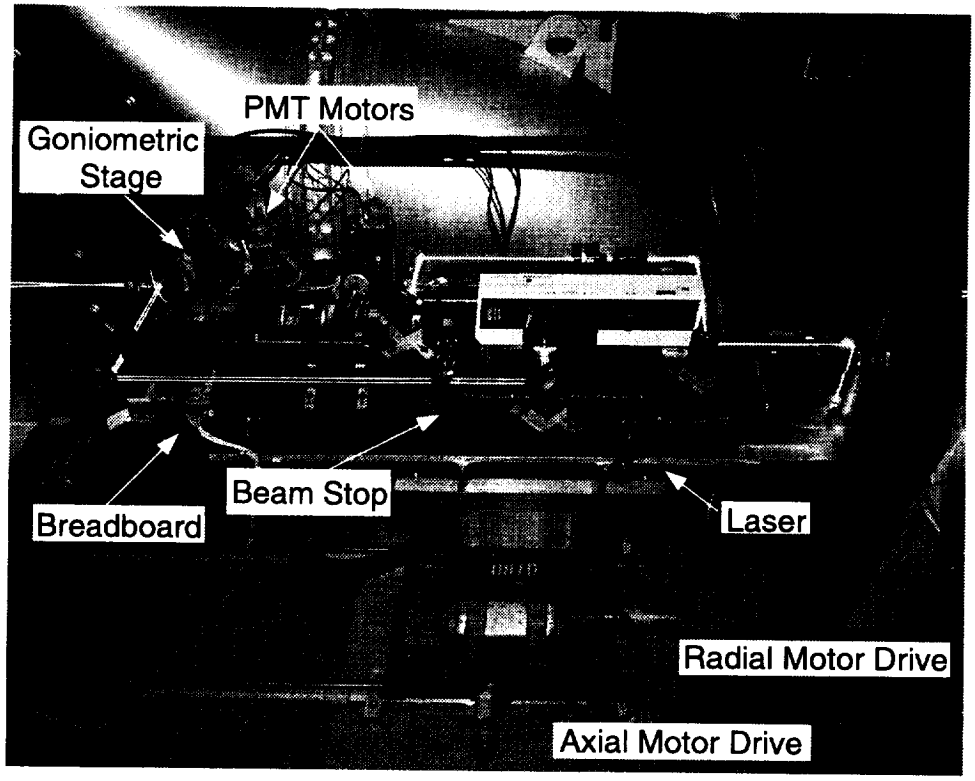

Figure 7. The laser anemometer system and its traverse mechanism.

probe volume thus generates a pitchwise flow field survey so that the velocity variation across a rotor blade pitch is measured. The LFA optical axis is aligned with the radial direction. The goniometric stage, which can be used to deflect the optical axis in an off-radial direction, which was not used except to change the probe volume orientation to avoid blade shadowing or window contamination problems.

For the stage measurements the probe volume must be traversed in the radial, axial, and circumferential directions so that the velocity variation across a rotor blade pitch is measured for all desired positions relative to the stator blade. Further information about the measurement positions is contained in the next chapter. For each measurement position the probe volume is placed at the correct axial/radial/circumferential location in the compressor and the goniometric stage is rotated such that the axis of the probe volume is on a radial line. This is necessary so that the velocity components measured are axial and tangential velocity.

The LFA technique requires the addition of seed particles to the flow field. Poly-Styrene Latex (PSL) particles were used for this research. PSL spheres can be reliably grown to a

specified size and the size variation within a batch is small. Particle sizes used in this investigation were 0.6 to 1.0 micrometers as determined from scanning electron microscope photographs of each batch of PSL particles. Particles must be small enough to follow the flow but large enough to scatter sufficient light for the LFA system to measure. The inability of particles to follow flow gradients is called particle lag and is discussed in detail relative to transonic turbomachinery applications by Suder (1996). Particle sizes used in this investigation do not compromise the results. The measurement accuracy of the LFA system is +/- 1.0 m/s in velocity and +/- 0.5 degree in flow angle.

To seed the flow field, the PSL spheres are first suspended in alcohol. The alcohol and seed solution is sprayed through atomizing nozzles into the inlet piping upstream of the plenum. The alcohol evaporates and leaves the PSL particles suspended in the flow.

2.4 Steady-state Instrumentation

The compressor facility includes steady-state instrumentation for monitoring the compressor operating point and measuring compressor performance.

The compressor operating point is set by wheel speed and mass flow. The mass flow is measured by the sharp-edged thin-plate orifice in the inlet piping to an accuracy of 0.05 kg/s. The compressor also has rotor tip static pressure taps. A more precise way to set the operating point from day to day is to match the rotor tip static pressures. Other pressures and temperatures are continuously monitored throughout the compressor. For example, the plenum pressure and temperature are recorded with the LFA data and are used to standard day correct the measured velocities.

Overall compressor performance was measured with conventional aerodynamic probes which are traversed radially upstream of the compressor and radially and circumferentially downstream of the compressor. Cobra probes are used to measure total pressure, total temperature, and flow angle. Wedge probes are used to measure static pressure and, redundantly, flow angle. The probes are traversed at axial stations -4.24 cm and 10.6 cm where 0 cm is the rotor leading edge/hub intersection as seen in Figure 4. Measurement accuracies are: flow angle 1.0 degrees, total pressure 0.01 N/cm^2, total temperature 0.6 K. See Appendix A for detailed aero performance measurements.

3. EXPERIMENTAL PROCEDURE AND DATA REDUCTION

The purpose of the experimental procedure was to acquire spatially and temporally resolved measurements of rotor wakes starting at the rotor trailing edge and continuing through the stator passage. For comparison, the wakes of the rotor in isolation were also surveyed. This chapter describes the compressor aerodynamic performance, the LFA measurement locations, the LFA system setup procedure, and the LFA data reduction procedures.

3.1 Compressor Aerodynamic Performance

The compressor rotor was operated at 80% of its design speed for this study. Figure 8 shows the compressor operating map for the rotor only and stage tests. LFA data was acquired for two rotor loading levels, near peak efficiency (PE) and near stall (NS). Table 2 is a summary of the operating conditions. For the rotor only case, overall operating conditions were determined from radial surveys of total pressure, total temperature, static pressure and flow angle at 18 radial locations. The total temperatures are mass averaged over the span and the total pressures are converted to their enthalpy equivalents and then mass averaged over the span. Adiabatic efficiency is calculated from the total pressure and total temperature ratios. See Appendix A for more details.

As described in the previous chapter, the stator blade geometry surveyed with the LFA were hub mounted while the remaining stators were casing mounted. Therefore, care was

Table 2: Summary of rotor only and stage test operating conditions.

		Mass Flow, kg/s	PR	TR	Efficiency, %
Rotor Only	PE	17.3	1.44	1.12	92.0
	NS	14.8	1.54	1.15	85.5
Stage	PE	17.2	1.40	1.11	88.5
	NS	15.1	1.49	1.15	80.8

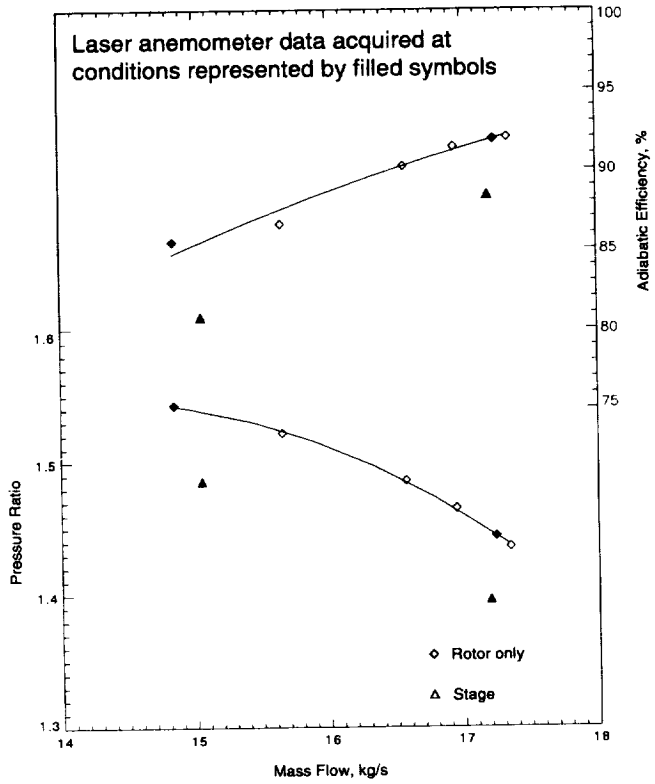

Figure 8. Compressor performance map for rotor only and stage tests.

taken to achieve blade to blade flow periodicity in the stator passage surveyed in the stage experiment. Appendix A contains the details of the periodicity measurements. For stage performance, the downstream cobra probe was traversed radially and circumferentially downstream of the hub mounted stators. Static pressure was assumed constant downstream of the stators so the wedge probe was not traversed circumferentially. The cobra probe was traversed over one stator pitch circumferentially with the stator wake contained within the survey. The survey grid contained 16 radial points and 21 circumferential points. Total temperature was mass averaged and total pressure was converted to enthalpy equivalents and mass averaged in the circumferential direction to obtain radial profiles. The radial profiles were then averaged in the same way as the rotor only data to obtain overall performance.

Equivalent operating conditions were set for the rotor only and stage tests so that wake behavior differences could be attributed primarily to the presence of the downstream blade row. To set operating conditions for the stage experiment, the rotor tip static pressure at the

rotor exit was matched to the static pressures measured in the rotor only experiment. Since the rotor tip static pressure is a measure of rotor work input, this approach insured that the LFA measurements were acquired in the rotor only and stage cases at approximately constant rotor work input. This approach also proved to be a more accurate and consistent method for resetting compressor operating point following shutdowns to clean the window and from day to day than relying solely on mass flow. The stage stalled at a slightly higher mass flow than the rotor in isolation. Therefore, at the NS condition, stage data was acquired at a higher mass flow than the rotor only data.

3.2 LFA Measurement Locations

Figure 9 shows the LFA measurement locations for the rotor only and stage tests. Since acquiring stage LFA data is far more time consuming than rotor only data, only limited data was taken in the stage environment. The survey grid was created using a CFD grid generation package and the Rotor 35 and Stator 37 geometry. Only the 75% span geometric stream surface was surveyed in the stage environment. Both pitchwise and streamwise surveys were acquired on this streamsurface. Pitchwise surveys were concentrated in the region between the rotor trailing edge and 20% stator chord.

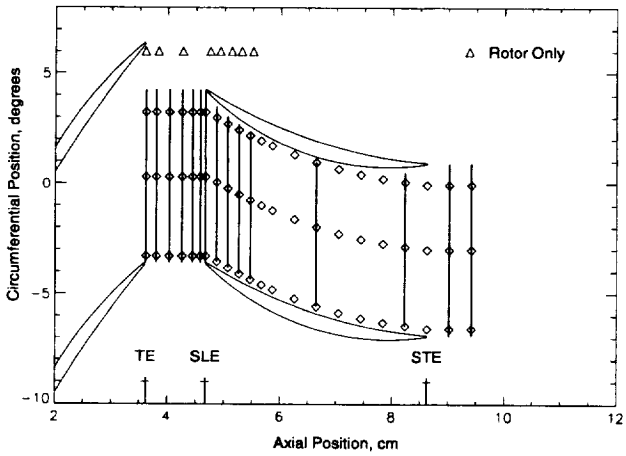

Figure 9. LFA measurement locations on the 75% span streamsurface for the rotor only and stage experiments.

Streamwise surveys were done at 4.2, 50.0, and 87.5% of stator pitch. In addition to the axial positions of the pitchwise surveys, the streamwise surveys also included 25, 30, 40, 50, 60, 70, 80, and 100% stator chord.Pitchwise surveys were also done at 50%, 100%, 90%, 110%, and 120% stator chord, to measure the remnants of rotor wakes exiting the stator passage. Each pitchwise survey contained 15 to 20 measurement locations in the pitchwise direction. Table 3 is a complete list of the axial measurement positions for the rotor only and stage data used in this experiment.

Table 3: LFA survey locations (in % stator axial chord) for the rotor only and stage experiment.

Rotor Only Surveys	
PE	-20.8, -10.1, 1.8, 6.7, 11.5, 16.4, 21.3, 118.7
NS	-26.6, -20.8, -10.1, 1.8, 6.7, 11.5, 16.4, 21.3, 118.7
Stage Pitchwise Surveys	
PE	-26.6, -22.0, -10.4, -5.8, 0.0, 5.0, 10.0, 15.0, 20.0, 50.0, 90.0, 110.0, 120.0, 150.0
NS	-26.6, -22.0, -16.2, -10.4, -5.8, -2.3, 0.0, 5.0, 10.0, 15.0, 20.0, 90.0, 110.0, 120.0, 150.0
Stage Streamwise Surveys	
PE	-26.6, -22.0, -10.4, -5.8, 0.0, 5.0, 10.0, 15.0, 20.0, 25.0, 30.0, 40.0, 50.0, 60.0, 70.0, 80.0, 90.0, 100.0, 110.0, 120.0, 150.0
NS	-26.6, -22.0, -10.4, -5.8, -2.3, 0.0, 5.0, 10.0, 15.0, 20.0, 25.0, 30.0, 40.0, 50.0, 60.0, 70.0, 80.0, 90.0, 100.0, 110.0, 120.0, 150.0

3.3 LFA Setup

At the start of the research program, the survey grid coordinates must be aligned to the compressor hardware. The LFA system was used to locate the stator leading edge blade tip by focussing the probe volume onto the tip of the blade. The circumferential coordinates of the grid were then adjusted so that the circumferential position of the stator blade in the survey grid matched the measured position of the rig hardware. The axial and radial positions of the

probe volume were adjusted by locating the upstream edge of the stator platform with the probe volume. The positioning system radial and axial offset values were then adjusted so that the indicated position matched the rig hardware location. These offsets were re-checked periodically during the test program. The positioning system was accurate to within 1% span, 1% pitch, and 1% chord.

Each day the LFA system optics were aligned for optimum performance and the transmitted beam power levels were checked. Both the blue and green beam crossing angles were checked and input to the data acquisition software. The current batch of seed in use was noted in order to document seed particle size. The system was then ready for use.

After the rig was started, two reference measurements were taken with the LFA system. With the rig at 60% design speed and maximum mass flow, a data point was acquired upstream of the rotor potential field. The measured flow should be axial with no (or small) variation with rotor position. This measurement served to check for proper LFA system alignment. Another reference measurement was acquired downstream of the rotor with the rig at the proper operating conditions. This measurement was used to check the rotor wake profile and distribution of measurements across the wake. See appendix B for a more detailed analysis of day-to-day wake differences.

On humid days the wake profile would be altered and the measurement distribution significantly skewed from their normal dry day profiles. These problems were most likely due to the alcohol carrier not evaporating completely from the seed material. This would result in oversize particles which would not track the flow field accurately thus resulting in altered wake profile measurements and the skewed measurement distributions because the LFA processor rejected measurements from the oversize particles. Data acquisition was cancelled on the high humidity days.

3.4 LFA Data Reduction

The LFA data is standard day corrected using the plenum as the inlet conditions. The velocities are corrected as:

$$V_{corr} = V\sqrt{\frac{T_{ref}}{T_{plenum}}} \qquad \text{(EQ 1)}$$

In the remainder of this report all velocities are assumed corrected and the subscript *corr* is dropped.

The LFA data is acquired for all 36 rotor passages at a resolution of 184 windows per passage which yields 6624 windows per revolution. Typically 30,000 to 60,000 velocity realizations are acquired at each measurement location. Prior to LFA data analysis the data acquired at each measurement location is processed into an average blade passage form as follows.

The data are first processed to obtain an average velocity for each window:

$$\overline{V}_j = \frac{1}{nm_j}\sum_{i=1}^{nm_j} V_{i,j} \qquad \text{(EQ 2)}$$

where j=1, 6624. $V_{i,j}$ is the *i*th velocity measurement in window *j* and nm_j is the number of measurements in window *j*. $\overline{V}_j$ is ensemble averaged across one blade pitch to yield an average passage:

$$\overline{V}_k = \frac{1}{(np - nz)}\sum_{n=1}^{np} \overline{V_{(k+(n-1)\times 184)}} \qquad \text{(EQ 3)}$$

where k=1, 184. *np* is the number of passages (36) and *nz* is the number of passages with zero measurements in window *k*. This average is calculated for both the axial and tangential velocity. The average passage velocity is stored with the number of realizations and the standard deviation of the velocity realizations for each window (k=1, 184). The analysis in this report is done based on this average passage formulation.

The radial velocity component is not measured by the LFA system. The error introduced by ignoring the radial velocity component will be estimated using the stage numerical simulations and presented in a later chapter.

3.5 Data Acquisition

As mentioned previously, data acquisition in the isolated rotor configuration only requires positioning the probe volume at one axial/radial location and acquiring data as the rotor sweeps past. There is no variation of properties in the circumferential direction.

In the stage environment the probe volume must also be traversed in the circumferential direction to map the stationary flow field associated with the stator and the superimposed unsteady rotor flow field. The flow field can then be viewed in several ways as illustrated in Figure 10 using data from the PE case at the stator leading edge.

An LFA data point at an axial/radial/circumferential position shows the velocity as a function of rotor position for a rotor blade passing cycle at that position relative to the stator. Velocity profiles for a rotor passing cycle acquired at 50% and 96% pitch are shown in Figure 10. The wake has been shifted to the center of the rotor period for easier comparison. Note the different rotor wake behavior depending on position relative to the stator blade.

By surveying a series of axial and circumferential positions a grid of measurement points is acquired so that the velocity as a function of rotor position is known for each point. For this data the rotor passing is divided into 184 time steps. The stator flow field can be viewed for any fixed rotor/stator position as shown in the lower left of Figure 10 for rotor position 80 of 184. This illustration was created by plotting the 80th velocity measurement from each of the measurements at the stator leading edge plane. By stepping through rotor positions (time) a movie is generated of the velocity field behavior versus rotor position. Contour plots of wake behavior are shown this way in Appendix B.

Averaging over a rotor blade passing period yields a time average view of the flow field which shows the stator potential field. The time average axial velocity at the stator leading edge plane is shown in the lower right of Figure 10.

The data could also be transformed into the rotor reference frame where the rotor would appear stationary and the stators would sweep by. The rotor wakes would appear to bend due to the presence of the stator. The data is not presented in that reference frame in this report.

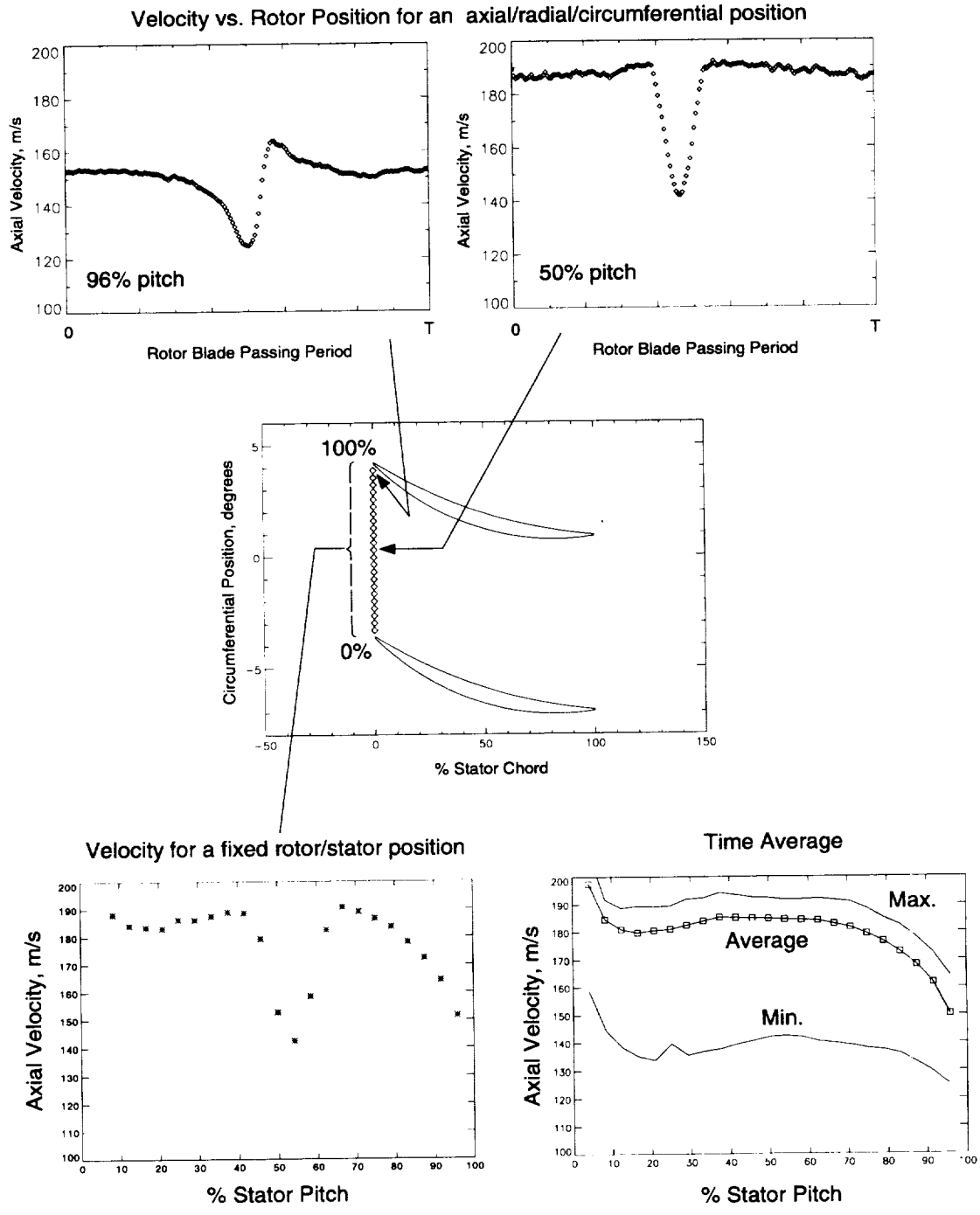

Figure 10. Viewpoints from which to interpret LFA data acquired in a stage environment.

4. NUMERICAL SIMULATIONS

Both steady and unsteady simulations of the stage were done to help interpret the experimental data. This chapter describes the codes and grids used and shows representative comparisons done to assess the accuracy of the simulation results.

4.1 Steady Simulations

The steady simulations were performed using the average passage code, APNASA, developed by Adamczyk (1985). The code solves the average passage formulation of the Reynolds Averaged Navier Stokes equations and the version of the code used has a Baldwin Lomax turbulence model. The blade clearance gaps are modeled by periodic boundary conditions using a height equal to one half of the physical clearance. This is analogous to assuming an orifice with a discharge coefficient of 0.5.

The stage geometry input begins with the design coordinates from Reid and Moore (1978b). A NASTRAN finite element analysis of the rotor was done at 80% design speed with estimated temperature and pressure loads. This determines the blade hot shape which is the shape of the blade during operating conditions with deflections due to centrifugal and pressure loads. In high-speed machines the rotor blade deformation can be significant and the hot geometry must be used to obtain an accurate numerical simulation.

Although APNASA can simulate machines with arbitrary blade counts, the full unsteady code can not. Therefore, the 36/46 blade count for the stage was changed to 36/48, which is a 3/4 blade count, in preparation for a full unsteady stage simulation to be done in the future. The rotor grid size was 226 axial x 51 radial x 57 tangential grid nodes with 51 nodes along the blade chord. The stator grid size was 226 axial x 51 radial x 43 tangential grid nodes with 51 nodes along the blade chord. The style of grid used is a sheared H mesh. The rotor clearance gap is two grid cells. The code was run on both IBM SP2 parallel systems and a Cray C90 supercomputer.

The APNASA solution is started from a uniform flow field initial guess with a back pres-

sure intended to give a solution on the choke portion of the operating line. Successive solutions at higher back pressure values are started using the previous back pressure solution as an initial guess. The back pressure is adjusted until the desired mass flow is obtained. The solutions are allowed to iterate until the mass flow rate, pressure ratio, temperature ratio, and number of separated points are stable. These converged solutions become the starting point for the unsteady code.

APNASA code simulations were done of the stage at mass flows that matched, as closely as possible, the experimental conditions. Table 4 shows a comparison of the overall performance from APNASA results and experimental measurements. These APNASA solutions were interpolated onto the unsteady code grid and the simulation run until the flow is periodic with a rotor blade passing period.

Table 4: Overall performance results from experiment and APNASA simulation.

	Experiment		APNASA	
	PE	NS	PE	NS
m (kg/s)	17.2	15.1	17.2	15.2
PR	1.40	1.49	1.43	1.50
Efficiency	88.4	80.8	85.2	80.1

4.2 Unsteady Simulations

The unsteady code, MSU-TURBO, was developed by Chen et al. (1994) to solve the time-dependent 3D Reynolds Averaged Navier Stokes equations. The code uses an implicit solution scheme to advance the solution in time and is second order accurate in time and space. Baldwin Lomax is the turbulence model used.

MSU-TURBO was not used in its full unsteady stage form for generating solutions for this thesis due to time/computing constraints. The form of MSU-TURBO used simulates only the stator passage and models the rotor (wake generating blade row) as an unsteady upstream boundary condition. This scheme will simulate wake stretching and wake/blade interactions correctly but will not simulate stage interactions.

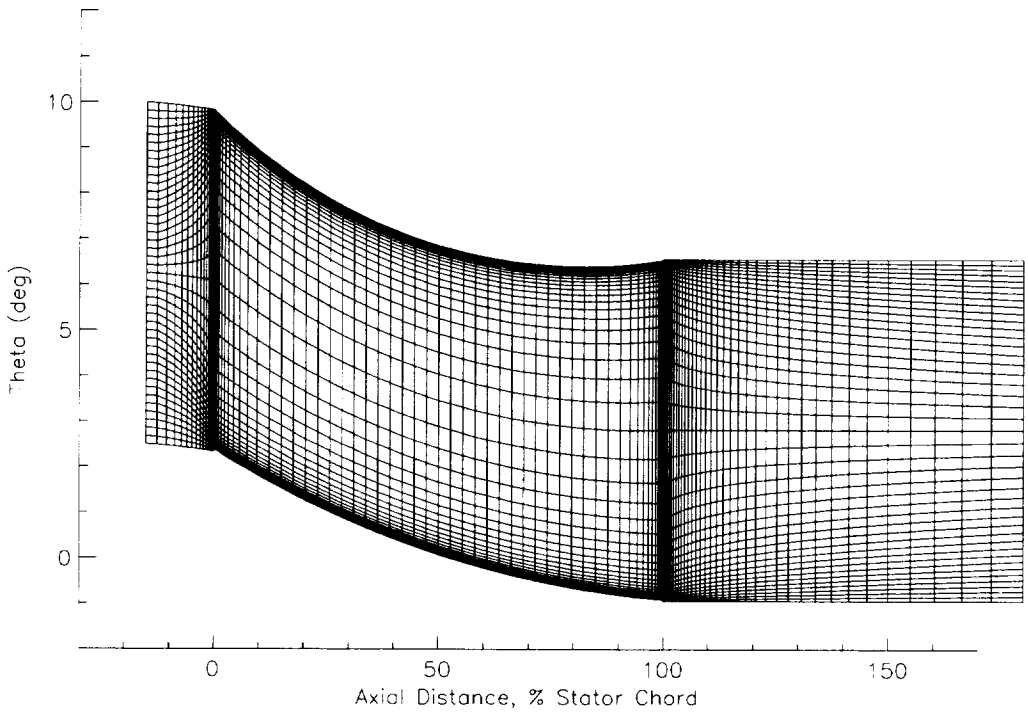

Figure 11. Blade to blade view of one stator grid block at 75% span for the unsteady code.

The setup for the unsteady code involves building new grids based on the APNASA grids, interpolating the APNASA solution onto the new grids, and setting the appropriate boundary conditions. The unsteady code grid must have equally spaced grid points in the tangential direction at the mid rotor/stator plane. The APNASA stator grid was modified to include the required rotor/stator interface. Due to memory and storage limitations, the grid was also reduced in axial size. Figure 11 shows the blade to blade view of the grid on the 75% span streamsurface. The stator grid is 101 axial x 51 radial x 43 tangential grid nodes with 51 nodes along the blade chord. The APNASA flow field solution was then interpolated onto the new grid. The unsteady upstream boundary condition was also determined from the APNASA solution.

The APNASA solution provides an excellent initial guess for the MSU-TURBO code. The APNASA solution determines the vortical flow field entering the downstream blade row and defines the unsteady upstream boundary condition. The unsteady code then calculates the response of the stator to the rotor wake (Chen 1994). This method of solution is an order of magnitude faster than starting from a uniform flow field and makes time accurate solutions

feasible. The CPU time needed to obtain a periodic solution is reduced from hundreds of CPU hours to approximately 20 CPU hours on a Cray C90 supercomputer. The unsteady code requires the memory and high speed disk resources of the C90 to execute in a reasonable time.

The time step size in terms of rotor grid spacing is an input to the code. A time step size study determined that the default time step (56 steps per rotor blade period) was not small enough to maintain rotor wake resolution. Reducing the time step to smaller than 0.25 of the default no longer resulted in significant changes in the solution flow field. Therefore, a time step of 224 steps per rotor period (1/4 of the default) was used.

During code execution a history file is output which contains the mass flow rate in and out of the stator blade row and also the value of static pressure at a point near the leading edge of the stator on both the pressure and suction surfaces at mid span. The solution is considered converged when these values become periodic with time. Figure 12 shows the solution history for the PE case where the solution becomes periodic after 6 blade passings.

All code results are post processed into Plot3D format for analysis. It is not practical to output each time step from the unsteady solution, so 14 time planes per rotor passing period were output.

MSU-TURBO solutions are used as a tool to evaluate errors associated with measurement limitations and to aid in interpreting the data. For comparison to the LFA data, Appendix C contains contour plots of the 75% span streamsurface showing the predicted rotor wake behavior in the stator passage. There is a wealth of information in these solutions which is well beyond the scope of this thesis. It is intended that these solutions will be studied further in addition to running a full unsteady stage simulation as a logical extension of the current work.

4.3 Unsteady Simulation Results

The unsteady simulation results are compared to experimental measurements in terms of time average velocities and time accurate results. Some differences between the measured and simulated results should be expected due to the 4.4% increase in solidity of the stator row in the simulations. The unsteady solutions were time averaged and compared to the average LFA results in Figure 13 for absolute velocity at 75% span. The LFA data do not have sufficient

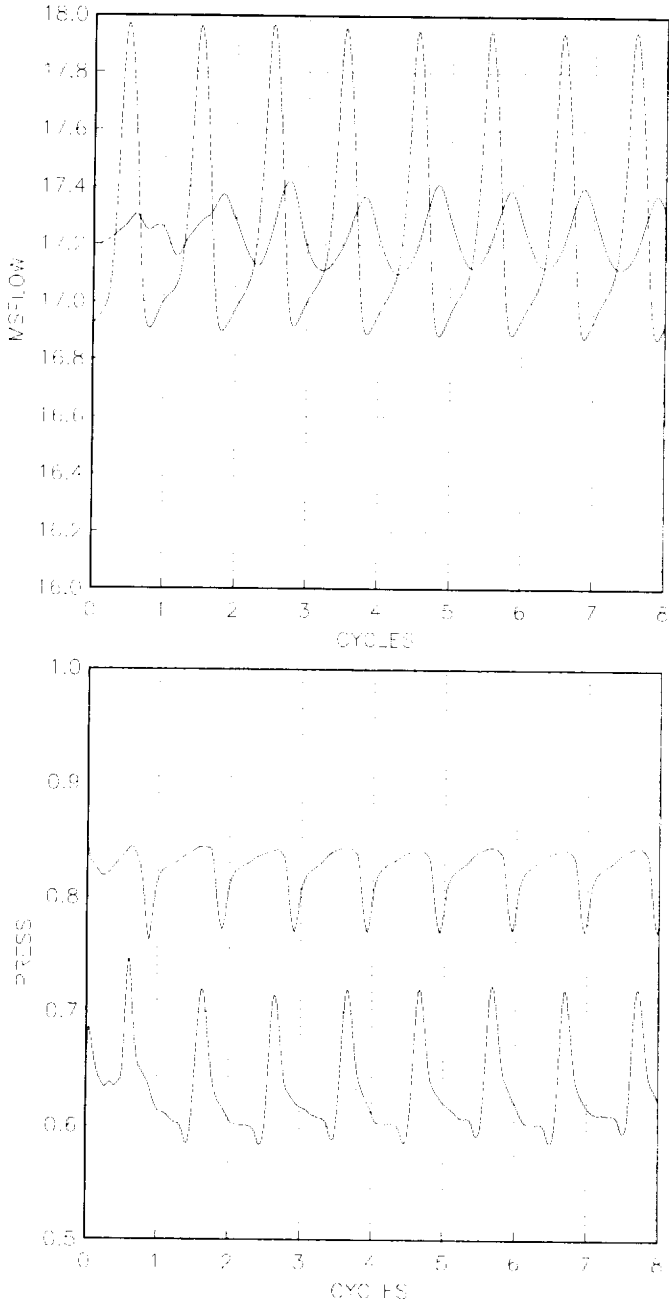

Figure 12. Massflow and pressure history for the PE unsteady simulation.

spatial detail at the stator exit to allow contour plotting. Instead Figure 14 shows the time average absolute velocity at the 120% stator chord plane for the LFA and simulation data.

The time average results at 75% span shown in Figure 13 are in excellent agreement with the time average measurements. The character of the flow fields is the same and the absolute

velocities agree to within approximately 5 m/s (better than 5%). Note also that the stator is aft loaded in the PE case and front loaded in the NS case.

The LFA data shown in Figure 13 extends from the rotor trailing edge to 20% stator chord. The 'raggedness' of the LFA data contour lines compared to the simulation results is due to both limited spatial resolution and day-to-day operating point variations. A comparison of Figures 9 and 11 shows the difference in spatial resolution. Each pitchwise LFA survey contains 15 - 20 points in the circumferential direction while the simulations utilize 43 nodes across the stator pitch. Time constraints limit the total number of experimental data points acquired. Several days of run time were needed to acquire the data for each operating condition with multiple rig shutdowns each day to replenish the seed supply and clean the optical access window. Reference measurements taken each day show that the repeatability of the operating condition as determined from the time average axial velocity is +/- 5.0 m/s for PE and +/- 2.5 m/s for NS. The PE data was acquired over more days and thus the larger uncertainty. The uncertainty is still less than 2.5% of the time average absolute velocity. See appendix B for a more detailed description of how these uncertainties were calculated.

As an interesting sidenote, there exists a dichotomy in the time/space information contained in the measurements and the simulations. The measurements have good time resolution (184 points per blade passing period) but poor spatial resolution. The simulations have good spatial resolution (43 points across the stator pitch) but poor time resolution (14 time planes). Even though the simulation calculates 224 time steps per blade passing, due to storage limitations, it is not practical to store more than a few time steps. Both types of data have their strengths and weaknesses.

Time accurate details of the flow field are examined in Figure 15 which shows a view of the stator flow field for a fixed rotor/stator position where the rotor wake is at midpitch. Overall the qualitative behavior of the rotor wakes in the unsteady stator simulations agreed well with the experimental observations. The rotor wake in the PE case is narrower in both the LFA data and simulation than the NS rotor wake. The NS simulation and LFA data both show greater wake/blade interaction on the suction surface near the stator leading edge. Although the simulations show the correct trends, the rotor wakes in the simulations are consistently wider and shallower than those measured. Figure 16 shows a comparison of measured and

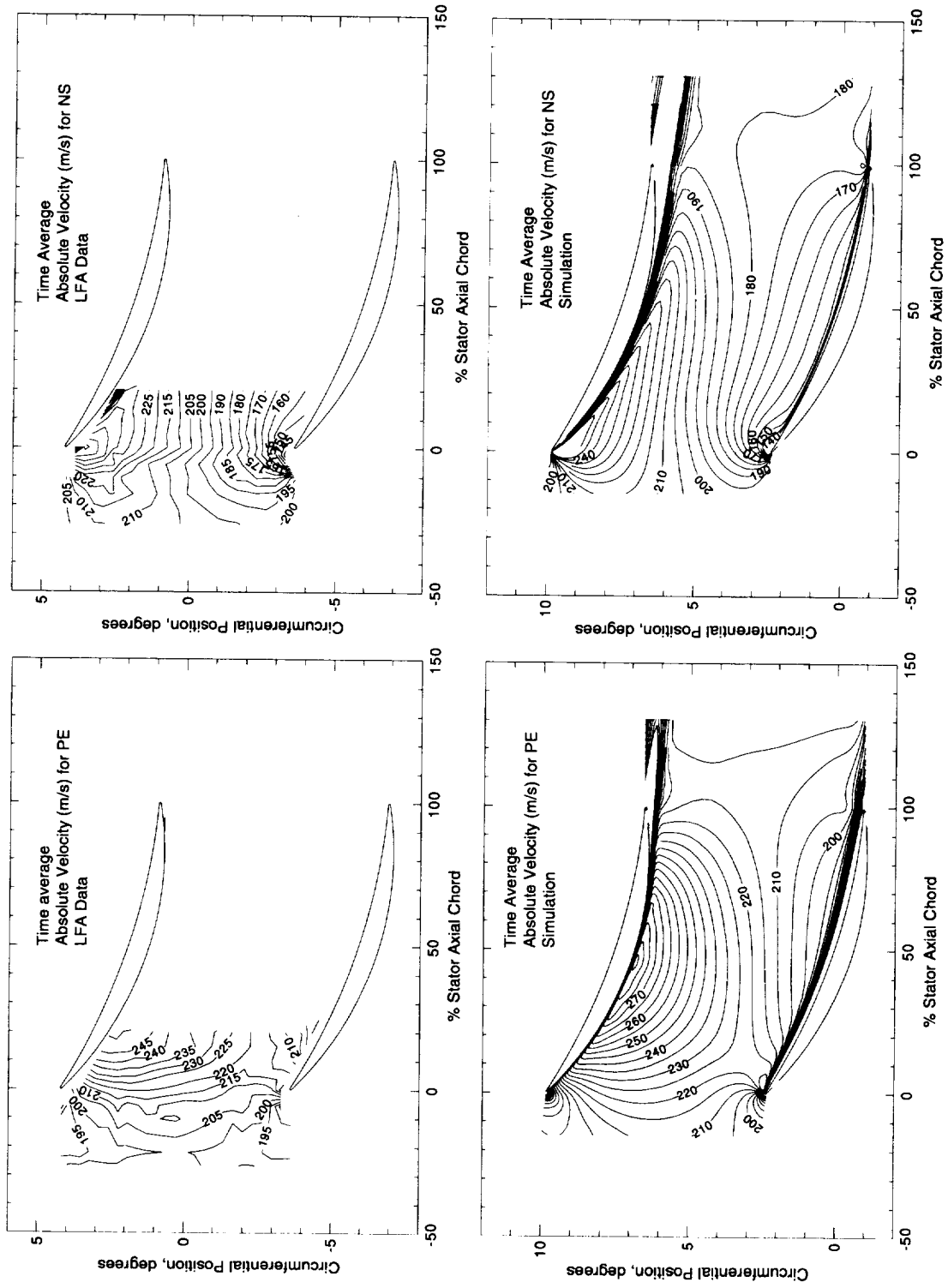

Figure 13. Time average absolute velocity flow fields for LFA data and simulations.

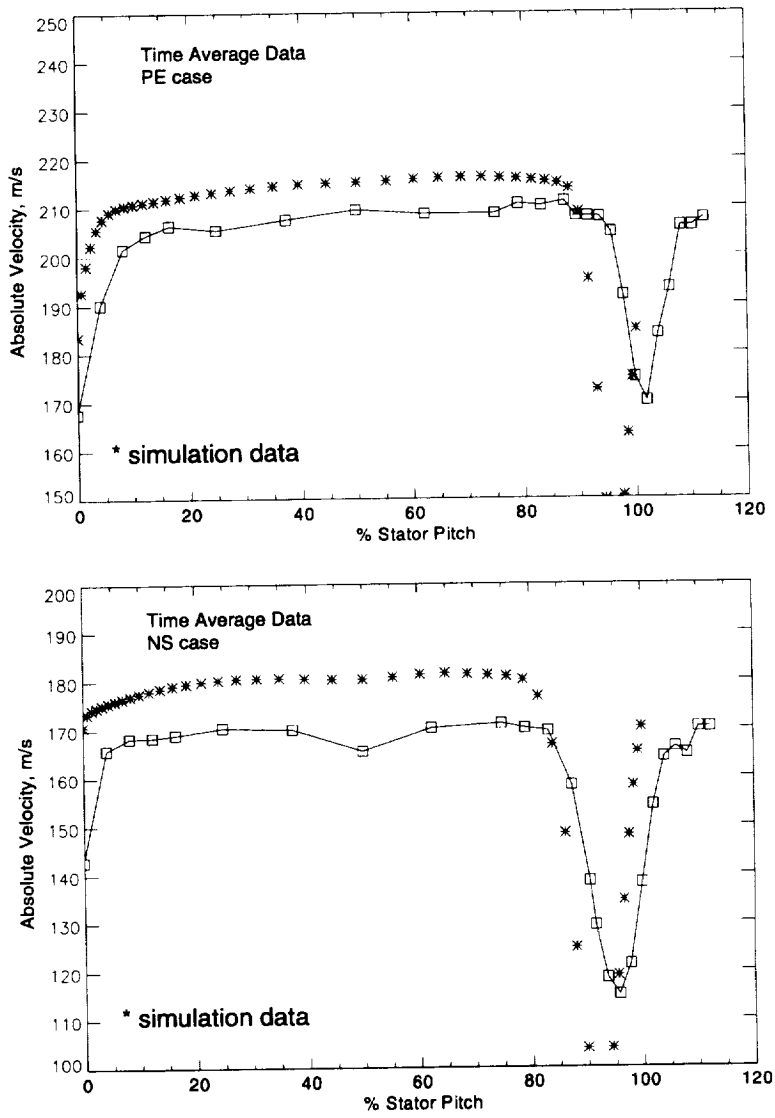

Figure 14. Pitchwise profiles of time average absolute velocity at the 120% stator axial chord plane.

simulation rotor wakes at the stator leading edge plane. The wake differences indicate more dissipation in the simulations than the experiment. It is not known if this is due to the turbulence model, grid topology, or numerics. Since the simulations are used only to help interpret the data, these differences in wake character do not affect the analysis conducted in this dissertation.

More views of the LFA measurements for additional rotor/stator positions are shown in Appendix B. Results from the simulation time steps which best match the measured rotor/sta-

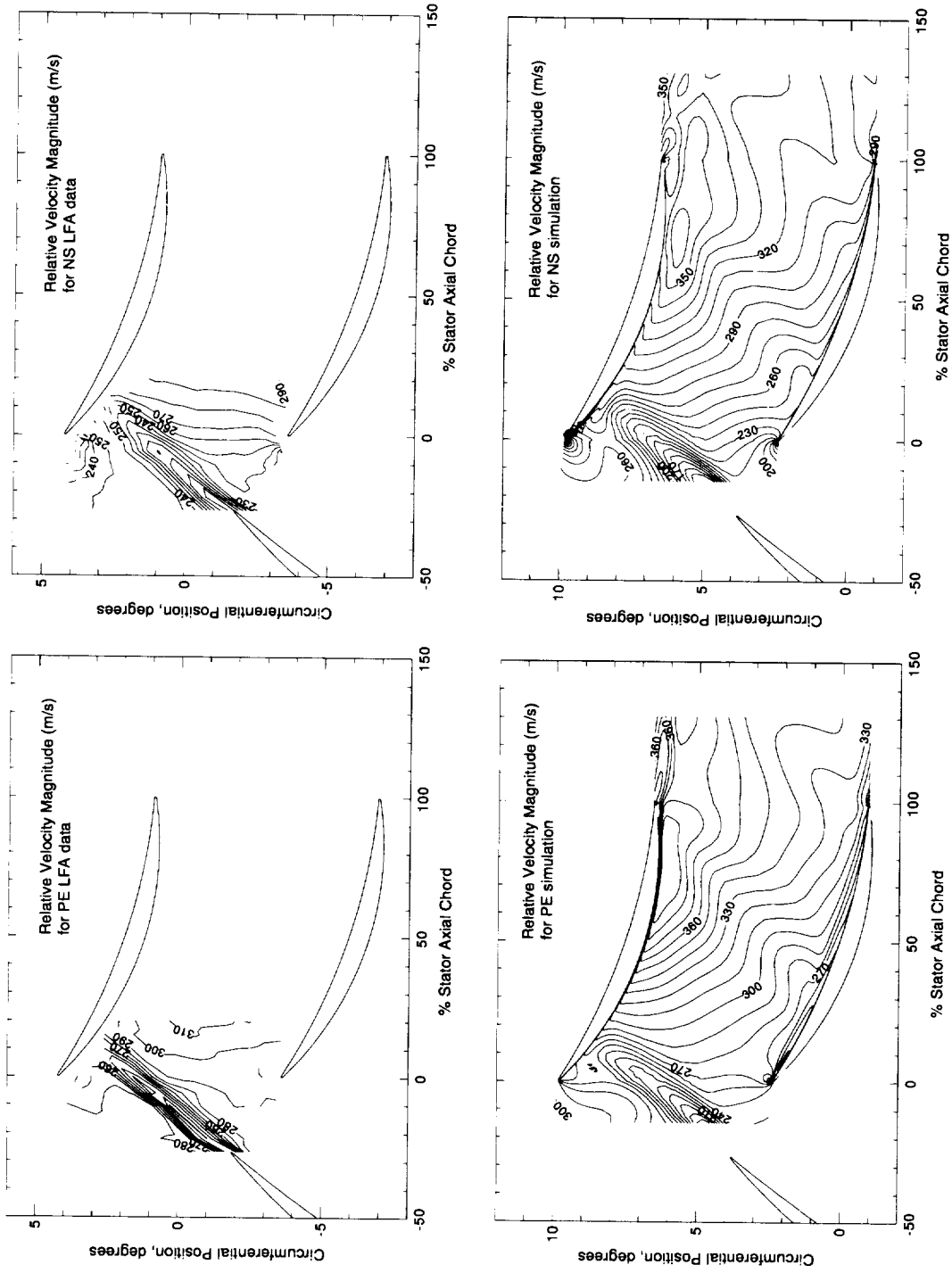

Figure 15. Examples of a rotor wake entering the stator passage from the LFA data and the simulations.

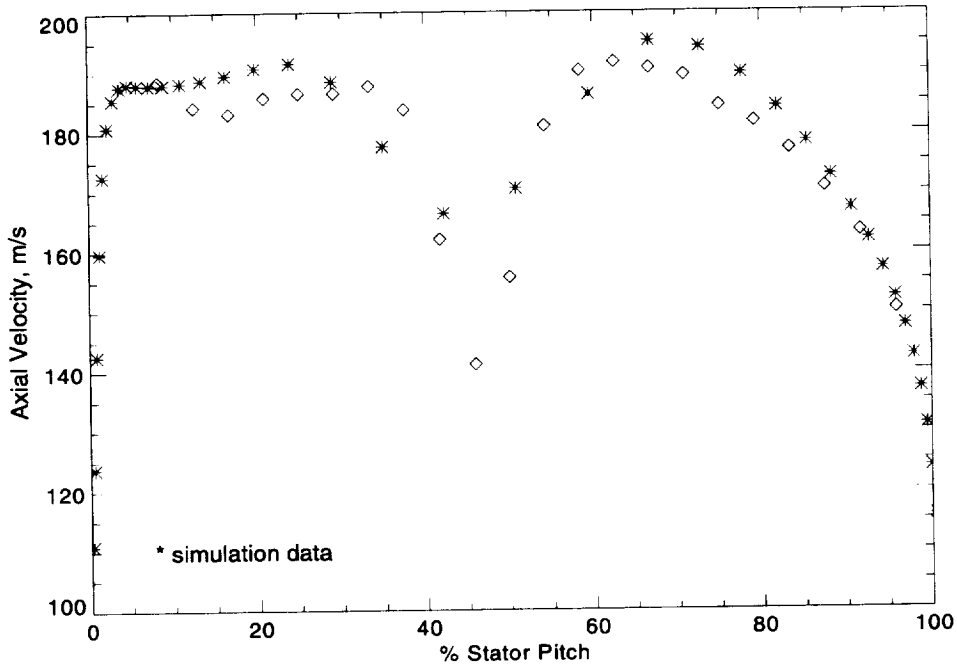

Figure 16. Comparison of measured and simulation wake at the stator leading edge plane for the PE case.

tor positions are shown in Appendix C. This qualitative information was very helpful in interpreting the experimental data since only a small portion of the flow field was measured.

These comparisons between the time average and time accurate simulation and LFA measurement flow fields show acceptable agreement. The simulations are therefore considered to be representative of the experimental observations and are used in interpreting the test data.

5. WAKE DECAY MODEL

Before the wake decay model is presented, the relation of unsteadiness in the flow field to mixing loss is developed. The relationships determined are used to consider how the production of loss due to the decay of rotor wakes is impacted by flow mechanisms occurring in the stage environment. The later sections give an overview of the kinematics of the rotor wake convection process through a stator row and present the development of a rotor wake decay model.

5.1 Relation of Unsteadiness to Mixing Loss

The relation between flow field unsteadiness and mixing loss comes from the analysis of Adamczyk (1996). Consider a 2D incompressible, inviscid flow with a time varying component of period T. The velocity and pressure fields are decomposed into time average and unsteady components. The time average component is further decomposed into a spatially periodic component over distance L and a time-average component which is constant in the y direction:

$$u_i(x, y, t) = U_i(x) + \hat{u}_i(x, y) + u_i'(x, y, t) \quad \text{(EQ 4)}$$

$$p_i(x, y, t) = P_i(x) + \hat{p}_i(x, y) + p_i'(x, y, t) \quad \text{(EQ 5)}$$

where $i = 1,2$ represent the axial and tangential directions. Velocities, pressure, and time are non-dimensional. The non-dimensional density is 1.0 and does not appear in the equations.

Two averaging operators are defined, the time average:

$$A_t f = \frac{1}{T}\int_0^T f\,dt \quad \text{(EQ 6)}$$

and the average in y:

$$A_y f = \frac{1}{L}\int_0^L f\,dy \qquad \text{(EQ 7)}$$

A mixing plane calculation can be used to estimate the total pressure loss due to viscous dissipation of 2D unsteady flow. The mixing plane is a control volume with an inlet at x_{ref} and an outlet at downstream infinity. Mass, specific impulse in the x direction, and y momentum are conserved across the control volume.

$$A_y A_t u|_{x_{ref}} = U_{mix} \qquad \text{(EQ 8)}$$

$$A_y A_t (p + u^2)\big|_{x_{ref}} = p_{mix} + U^2{}_{mix} \qquad \text{(EQ 9)}$$

$$A_y A_t (uv)|_{x_{ref}} = U_{mix} V_{mix} \qquad \text{(EQ 10)}$$

where subscript *mix* refers to the conditions at downstream infinity.

The difference in the time average mass flux of total pressure between the inlet and exit is the loss in total pressure due to viscous dissipation:

$$X = A_y A_t u P|_{x_{ref}} - U_{mix} P_{mix} \qquad \text{(EQ 11)}$$

where X is the total pressure loss. Total pressure is defined as:

$$P = p + \frac{1}{2}(u^2 + v^2) \qquad \text{(EQ 12)}$$

The velocity and pressure decompositions are substituted into the mixing plane calculation and the results are substituted into Eqn. 11. The resulting equation relates the total pressure mixing loss to the unsteady flow field:

$$\begin{aligned} X = {} & A_y A_t (p'u') + A_y (\hat{p}\hat{u}) + A_y A_t \left(\frac{1}{2} u(u'^2 + v'^2)\right) \\ & + A_y \left(\frac{1}{2}\tilde{u}(\hat{u}^2 + \hat{v}^2)\right) + A_y A_t (u'(\hat{u}u' + \hat{v}v')) \\ & - \frac{1}{2U_{mix}} A_y A_t (\hat{u}\hat{v} + u'v')^2 \end{aligned} \qquad \text{(EQ 13)}$$

where $\tilde{u}$ is the time average velocity, $\hat{u}$ is the spatially non-uniform velocity, and u' is the unsteady velocity.

The first two terms represent the pressure work at the inlet due to the unsteady and spatially nonuniform flow. The third term is the flux of disturbance kinetic energy (DKE) due to

the unsteady velocities. The fourth term is the flux of unsteadiness due to the spatial non-uniformity. The fifth and sixth terms are due to coupling of spatially nonuniform and unsteady flow.

A relevant question to ask is "Does passing a rotor wake through a blade row prior to mixing improve the compressor performance by reducing mixing loss?" Consider a case where the flow is mixed out prior to entering a blade row for instance at plane 1 shown in Figure 17. Denote this mixing loss as X_1. Next consider the case where the wakes are passed through the blade row prior to mixing at plane 2. The resulting mixing loss is X_2. The difference in mixing loss between these two cases is defined as wake recovery. The question can now be restated as:

$$\text{Is } X_1 - X_2 \text{ positive, negative, or zero?} \qquad \text{(EQ 14)}$$

In order to evaluate the wake recovery the velocity and pressure components, $f_i(x, y, t)$, $\hat{f}_i(x, y)$, and $f'_i(x, y, t)$, are expressed as perturbation series in Δ out to $O(\Delta^2)$. These perturbation series are substituted into Eqn. 13 for both the upstream plane 1 and the downstream plane 2. Furthermore, the mixing planes are considered far enough removed from the blade row such that pressure variations are of $O(\Delta^2)$ or higher. The result is:

$$X_1 - X_2 = K_1 R = K_1\left(1 - \frac{K_2}{K_1}\right) + O(\Delta^3) \qquad \text{(EQ 15)}$$

$$K_1 = \frac{1}{2} u_o A_y A_t (u^2 + v^2)\Big|_{plane1_1} \qquad \text{(EQ 16)}$$

$$K_2 = \frac{1}{2} u_o A_y A_t (u^2 + v^2)\Big|_{plane2} \qquad \text{(EQ 17)}$$

where K_1 and K_2 are the flux of the first order unsteady velocity components entering and leaving at planes 1 and 2 respectively. R is the recovery parameter and is analogous to that used by Smith (1993). If $R=1$ the unsteady flow has mixed out completely by reversible means. If $R<0$ the disturbance kinetic energy has increased. For $0<R<1.0$ energy has been transferred from the unsteady flow to the time average flow. Eqn. 15 states that recovery is related to the flux of disturbance kinetic energy entering and leaving a blade row for incompressible inviscid flow.

Smith (1966) proposed a simple model for recovery of total pressure mixing loss which is based only on wake lengths:

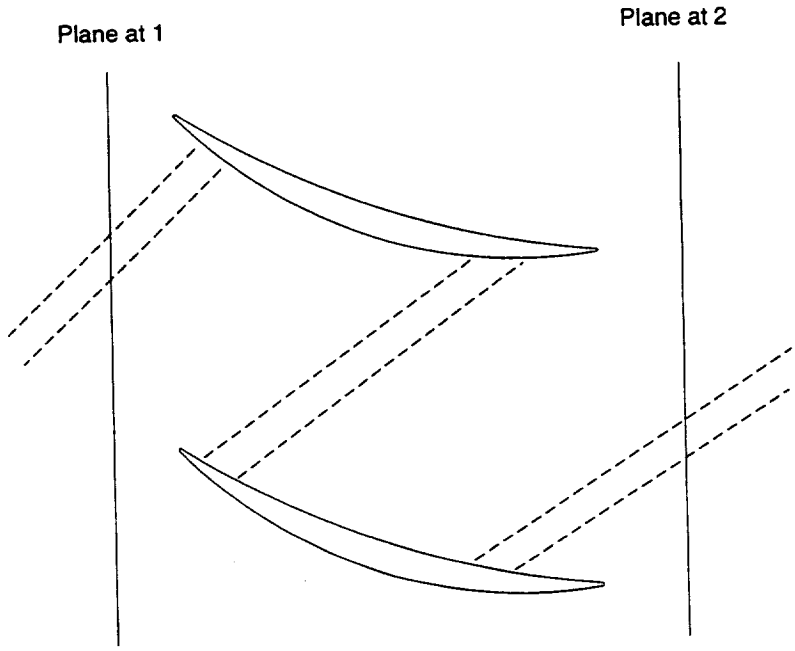

Figure 17. Mixing plane locations.

$$R = 1 - \left(\frac{L_{in}}{L_{exit}}\right)^2 \qquad \text{(EQ 18)}$$

This relationship can be derived by considering 2D, incompressible, inviscid flow and tracking a segment of rotor wake. The circulation is determined for the contour C shown in Figure 2 for a segment of rotor wake at the entrance to the stator passage. The upper and lower segments of the contour do not contribute to the circulation because periodicity is assumed for these surfaces. The circulation for contour C is $\Gamma = \int_{b1}^{c1} \vec{V}_{1w} \bullet ds + \int_{d1}^{a1} \vec{V}_1 \bullet ds$, where the subscript *1* represents the free stream velocity and *1w* represents the wake deficit velocity. The contour is rotated and stretched as it is convected with the wake through the stator to a final orientation and length at the stator exit. The circulation around the contour remains constant because the flow is assumed inviscid and incompressible. The circulation at the stator exit is $\Gamma = \int_{b2}^{c2} \vec{V}_{2w} \bullet ds + \int_{d2}^{a2} \vec{V}_2 \bullet ds$. Assuming that the free stream velocity remains relatively unchanged, for the circulation to remain constant the wake velocity deficit must decrease as the contour length increases, therefore $\vec{V}_{2w} > \vec{V}_{1w}$. The change in the wake deficit is thus proportional to the change in wake segment length.

Adamczyk (1996) showed that mixing loss is proportional to square of the wake deficit,

see Eqn. 13. Thus the reduction in the mixing loss due to wake stretching is proportional to the wake deficit squared which is proportional to the wake length ratio squared and therefore, Eqn. 18 deduced by Smith (1966) from these kinematic arguments is a good approximation to the total pressure recovery. This relation can be recovered from Adamczyk's analysis in the limit of thin airfoils and high reduced frequency.

Because the numerical simulations are used to help interpret the experimental data, it is useful to compare the change in the first order unsteady kinetic energy determined from the simulations to that calculated from the experimental data. Figure 18 shows a comparison of the flux of DKE for the stator flow field for both the data and simulations. The decay in the rotor/stator gap is more rapid in the simulations than the data. The decay of DKE inside of the stator passage is similar for both the simulations and experiments. This gives confidence that the simulations are representative of the measurements. The uncertainty in the DKE calculation is +/- 0.01 for PE and +/- 0.005 for NS in units of % of U^3_{tip} as determined from the daily reference measurements.

5.2 Overview of Rotor Wake Convection

A rotor wake passing through a stator row is chopped, rotated, and stretched all of which potentially contribute to the wake decay process. Figure 19 illustrates this for a rotor wake segment of mass as it enters the stator passage and as it exits the stator passage after being rotated and stretched. Two mechanisms are responsible for rotating and stretching the wake segment, the diffuser effect and the circulation effect (Deregel and Tan, 1996).

If the stator passage is thought of as a diffuser with no turning, the leading end of the wake segment will enter an area of diffusing flow first and thus slows. The trailing end of the wake segment is still in the higher speed flow upstream of the stator. The effect is that the segment rotates counterclockwise.

The second mechanism is the circulation effect. Due to the blade loading (turning of the mean flow), the velocities along the suction surface are higher than the velocities along the pressure surface of the stator blade. This will cause a clockwise rotation of the wake segment. The experimental data shows that the circulation effect is the dominant mechanism and the wake segments are rotated clockwise as shown in Figure 19.

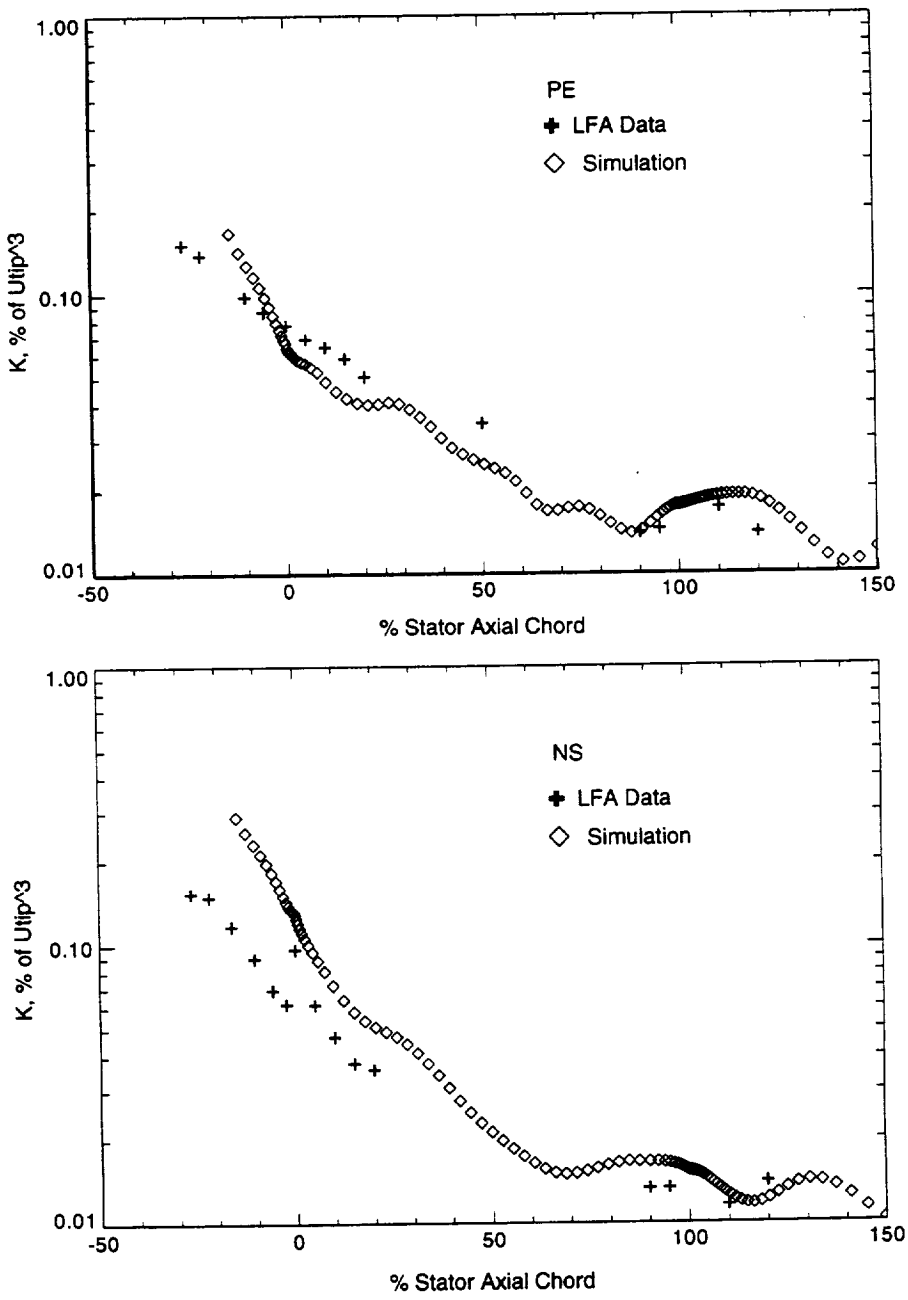

Figure 18. Comparison of the stage LFA and simulation decay of the flux of DKE for the PE and NS operating conditions.

As a result of the rotation of the wake segment, its length is increased at the exit of the stator passage relative to its length at the stator inlet. The wake stretching causes a reversible reduction in the wake velocity deficit as postulated by Smith (1966). This attenuation of the wake velocity deficit by stretching is a reversible mechanism and thus does not lead to a loss

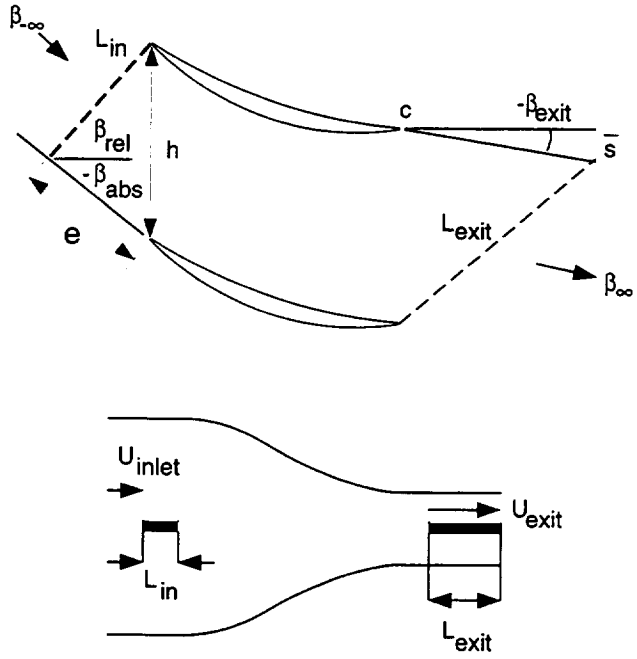

Figure 19. Rotor wake chopping and transport and the 2D converging channel/wake stretching analogy.

in total pressure or a rise in entropy.

This idealized situation ignores effects which may predominate in a compressor. In reality, the rotor wake undergoes viscous decay as it convects from the rotor trailing edge to the stator leading edge. Once inside the stator passage, both stretching and viscosity act concurrently on the wake. Any model for rotor wake decay in a stage environment must include both effects.

5.3 Development of Wake Decay Model

A method for estimating the viscous contribution to wake decay comes from the work of Hill, et al. (1963) on the decay of turbulent wakes in pressure gradients. Hill, et al. developed a model for the wake decay which includes pressure gradient and viscous effects. The model predictions compared well to measurements of wake decay in adverse pressure gradients. Hill stated that the model was equally applicable to favorable pressure gradients. This applicability to favorable pressure gradients allows the model to be used for rotor wake decay calculations in the stator environment as follows.

In the stator passage the rotor wakes are convected with the mean stator flow field (to a

good first order approximation). The time mean flow as determined from measurements (or a compressible viscous simulation) will account for the effects of compressibility and also changes to the mean flow due to boundary layer growth on the blades. Imagine a trail of rotor wake fluid particles "embedded" in this mean flow. As the flow convects through the stator the trail of particles is rotated and lengthened by the mean flow. To an observer riding on a wake fluid particle the wake simply appears to be stretched.

Rotor wake stretching in the stator passage is analogous to the lengthening of a wake segment of mass as it convects through a converging channel (acceleration) as shown in Figure 19. To an observer riding on a wake fluid particle, this situation looks identical to the wake stretching that occurs in the stator passage. For 2D incompressible flow the wake length ratio across the channel is given by:

$$\frac{L_{exit}}{L_{inlet}} = \frac{U_{exit}}{U_{inlet}} \qquad \text{(EQ 19)}$$

By choosing the correct velocity ratio for a 2D channel, the lengthening of a wake segment as it convects through that channel can simulate rotor wake lengthening in a stator passage.

The wake decay model consists of two parts: 1) a model which is used to predict the wake stretching given inlet and outlet velocity triangle information for the stator passage and, 2) a model which predicts the decay of the wake velocity profile with the effects of viscosity and stretching acting concurrently. The development of each part of the wake model is now presented.

The wake stretching model comes from the work of Adamczyk (1996) which is based on the work of Smith (1955). An outline of the derivation follows.

All lengths and angles used in the derivation are shown in Figure 19. The law of sines is used to define the following lengths:

$$\frac{h}{\sin(\beta_{rel}-\beta_{abs})} = \frac{e}{\sin(90-\beta_{rel})} = \frac{e}{\cos(\beta_{rel})} \qquad \text{(EQ 20)}$$

$$\frac{L_{in}}{\sin(90+\beta_{abs})} = \frac{h}{\sin(\beta_{rel}-\beta_{abs})} = \frac{L_{in}}{\cos(\beta_{abs})} \qquad \text{(EQ 21)}$$

The ends of the wake segment are tracked so that the convection time for a particle along

the pressure surface, denoted by subscript p, is the same as the convection time along the suction surface, denoted by subscript s. q is the velocity magnitude.

$$\int \frac{1}{q_s} ds = \int \frac{1}{q_p} ds \qquad \text{(EQ 22)}$$

This can be expressed approximately as:

$$\int_0^c \frac{1}{q_s} ds + \frac{(\bar{s} - c)}{q_\infty} = \int_0^c \frac{1}{q_p} ds + \frac{e}{q_{-\infty}} \qquad \text{(EQ 23)}$$

so

$$\frac{(\bar{s} - c)}{q_\infty} = \int_0^c \left(\frac{(q_s - q_p)}{q_s q_p} \right) ds + \frac{e}{q_{-\infty}} \qquad \text{(EQ 24)}$$

Now let

$$\frac{1}{q_s q_p} = \frac{1}{\bar{q}^2} \qquad \text{(EQ 25)}$$

where

$$\bar{q} = 0.5(q_{-\infty} + q_\infty) \qquad \text{(EQ 26)}$$

Also the blade circulation Γ is

$$\Gamma = \int_0^c (q_s - q_p) ds = h(V_{exit} - V_{inlet}) \qquad \text{(EQ 27)}$$

where V is the tangential velocity. This relation for circulation comes from the fact that circulation for a given path is constant with time in an incompressible inviscid flow. At t=-∞ the circulation around a contour far upstream of a blade as shown in Figure 20 is zero. At some time later, t=T, the contour is shown enclosing the blade. The circulation of the blade is $\int_0^c (q_s - q_p) ds$. The upper and lower paths of the contour do not contribute to circulation because periodicity is assumed. Therefore, the circulation of the left and right paths must equal the blade circulation and thus Eqn. 27.

Now,

$$\frac{(\bar{s} - c)}{q_\infty} = \frac{e}{q_{-\infty}} + \frac{\Gamma}{\bar{q}^2} \qquad \text{(EQ 28)}$$

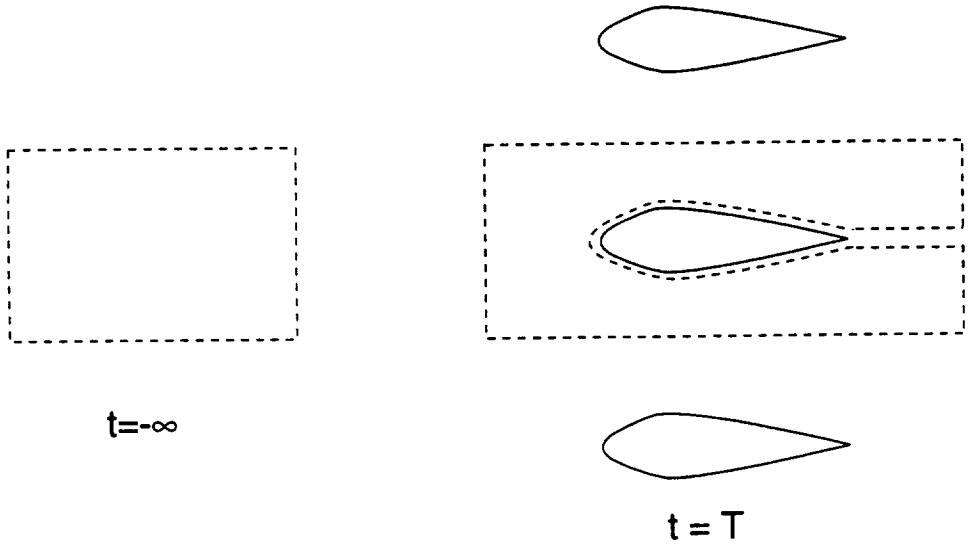

Figure 20. Contour path for blade circulation calculation.

Now apply the law of cosines at the exit:

$$L^2_{exit} = h^2 + (\bar{s}-c)^2 + 2h(\bar{s}-c)\cos(90+\beta_{exit}) = h^2 + (\bar{s}-c)^2 + 2h(\bar{s}-c)\sin(\beta_{exit}) \quad \text{(EQ 29)}$$

The wake segment lengths now become:

$$L_{exit} = h\left(1 + 2\frac{(\bar{s}-c)}{h}\sin(\beta_{exit}) + \frac{(\bar{s}-c)^2}{h^2}\right)^{\frac{1}{2}} \quad \text{(EQ 30)}$$

$$L_{in} = h\frac{\cos(\beta_{abs})}{\sin(\beta_{rel}-\beta_{abs})} \quad \text{(EQ 31)}$$

which yields the following expression for a wake length ratio:

$$\frac{L_{exit}}{L_{in}} = \frac{\sin(\beta_{rel}-\beta_{abs})}{\cos(\beta_{abs})}\left(1 + 2\frac{(\bar{s}-c)}{h}\sin(\beta_{exit}) + \frac{(\bar{s}-c)^2}{h^2}\right)^{\frac{1}{2}} \quad \text{(EQ 32)}$$

Now an estimate for the $(\bar{s}-c)/h$ term is needed.

$$\frac{(\bar{s}-c)}{h} = \frac{e}{h}\frac{q_\infty}{q_{-\infty}} + \frac{\Gamma q_\infty}{h\bar{q}^2} \quad \text{(EQ 33)}$$

Substitute for e from Eqn. 20:

$$\frac{(\bar{s}-c)}{h} = \frac{\cos(\beta_{rel})}{\sin(\beta_{rel}-\beta_{abs})}\frac{q_\infty}{q_{-\infty}} + \frac{\Gamma}{h}\frac{q_\infty}{\bar{q}^2} \qquad \text{(EQ 34)}$$

now let

$$q_\infty = \frac{U}{\cos(\beta_\infty)} \qquad \text{(EQ 35)}$$

$$q_{-\infty} = \frac{U}{\cos(\beta_{-\infty})} \qquad \text{(EQ 36)}$$

so now

$$\frac{(\bar{s}-c)}{h} = \frac{\cos(\beta_{rel})}{\sin(\beta_{rel}-\beta_{abs})}\frac{\cos(\beta_{-\infty})}{\cos(\beta_\infty)} + \frac{\Gamma}{h}\frac{U}{\cos(\beta_\infty)}\frac{1}{\bar{q}^2} \qquad \text{(EQ 37)}$$

From the circulation relationship

$$\Gamma = -h(V_{in}-V_{exit}) = -hU(\tan(\beta_{-\infty})-\tan(\beta_\infty)) \qquad \text{(EQ 38)}$$

and

$$\bar{q}^2 = \frac{U^2(\cos(\beta_{-\infty})+\cos(\beta_\infty))^2}{4(\cos(\beta_\infty)\cos(\beta_{-\infty}))^2} \qquad \text{(EQ 39)}$$

Substitute to finally obtain:

$$\frac{(\bar{s}-c)}{h} = \frac{\cos(\beta_{rel})}{\sin(\beta_{rel}-\beta_{abs})}\frac{\cos(\beta_{-\infty})}{\cos(\beta_\infty)} - \frac{4[\tan(\beta_{-\infty})-\tan(\beta_\infty)]}{(\cos(\beta_{-\infty})+\cos(\beta_\infty))^2}\cos(\beta_{-\infty}^2)\cos(\beta_\infty) \qquad \text{(EQ 40)}$$

From knowing only the inlet and exit velocity triangle information for the stator, the length ratio, L_{exit}/L_{in}, can be determined by using Eqns. 32 and 40. This is the wake stretching portion of the wake decay model.

The relationships describing the decay of the wake velocity profile come from the work of Hill et al. (1963). A summary of their derivation is given below.

The Reynolds average form of the momentum equations for 2D turbulent wake flow with second order terms omitted are:

$$u\frac{du}{dx} + v\frac{du}{dy} = -\frac{1}{\rho}\frac{dP}{dx} - \frac{\partial}{\partial y}(\overline{u'v'}) \qquad \text{(EQ 41)}$$

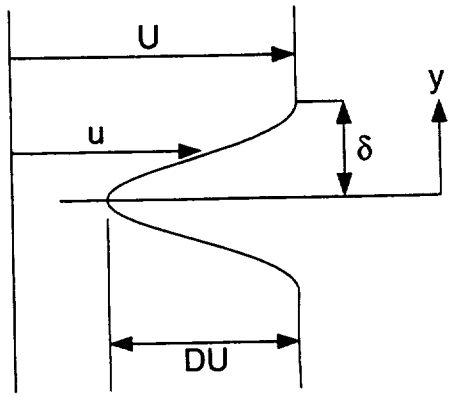

Figure 21. Coordinate system for wake decay model.

$$0 = -\frac{1}{\rho}\frac{\partial P}{\partial y} \qquad \text{(EQ 42)}$$

Viscous effects are included through an eddy viscosity defined as:

$$\varepsilon\frac{\partial u}{\partial y} = -\overline{u'v'} \qquad \text{(EQ 43)}$$

Eqn. 41, after using the Bernoulli equation for the $\frac{dP}{dx}$ term, becomes:

$$u\frac{du}{dx} + v\frac{du}{dy} = U\frac{dU}{dx} + \varepsilon\frac{\partial^2 u}{\partial y^2} \qquad \text{(EQ 44)}$$

It is useful to use similarity profiles for the wake shape. Hill et al. (1963) showed that this is a reasonable approximation. The form used is:

$$\frac{U-u}{U} = D\frac{1}{2}\left[1 + \cos\left(\frac{\pi y}{\delta}\right)\right] \qquad \text{(EQ 45)}$$

where δ is the distance from the wake centerline to the wake edge. See Figure 21. D is the relative wake depth defined as $(U\text{-}u_{minimum})/U$.

To predict the wake shape, a relationship for δ and D as a function of x is needed. Such a relationship can be derived from the Karman integral form of Eqn. 44:

$$\frac{d\theta}{dx} + \left(2 + \frac{\delta^*}{\theta}\right)\frac{\theta}{U}\frac{dU}{dx} = 0 \qquad \text{(EQ 46)}$$

where

$$\theta = \int_{-\infty}^{\infty} \frac{u}{U}\left(1 - \frac{u}{U}\right)dy \qquad \text{(EQ 47)}$$

$$\delta^* = \int_{-\infty}^{\infty} \left(1 - \frac{u}{U}\right)dy \qquad \text{(EQ 48)}$$

Evaluation proceeds by multiplying Eqn. 44 by *ydy*, using continuity, and integrating by parts. The wake profile relation, Eqn. 45, is substituted into the remaining integrals to obtain (for $D<<1$):

$$\frac{1}{D}\frac{dD}{dx}\left(-\frac{1}{4} + \frac{1}{\pi^2}\right) + \frac{1}{\delta}\frac{d\delta}{dx}\left(-\frac{1}{2} + \frac{2}{\pi^2}\right) + \frac{1}{U}\frac{dU}{dx}\left(-1 + \frac{4}{\pi^2}\right) = -\frac{\varepsilon}{U\delta^2} \qquad \text{(EQ 49)}$$

Substitution of the wake shape relation, Eqn. 45, into the momentum thickness and displacement thickness equations yields:

$$\theta = \delta\left(D - \frac{3D^2}{4}\right) \qquad \text{(EQ 50)}$$

$$\delta^* = \delta D \qquad \text{(EQ 51)}$$

The Karman integral equation becomes:

$$\frac{1}{D}\frac{dD}{dx}\left(\frac{4-6D}{4-3D}\right) + \frac{1}{\delta}\frac{d\delta}{dx} + \frac{1}{U}\frac{dU}{dx}\left(\frac{12-6D}{4-3D}\right) = 0 \qquad \text{(EQ 52)}$$

Combining Eqns. 49 and 52 yields:

$$\frac{1}{D^2}\frac{dD}{dx} + \frac{2}{D^2}\frac{1}{U}\frac{dU}{dx} = -\left(\frac{4\pi^2}{\pi^2 - 4}\right)\frac{\varepsilon}{U\theta^2} \qquad \text{(EQ 53)}$$

Although D<<1 is implied by this part of the derivation, Hill et al. (1963) found that the equations are applicable for $0.0<D<0.5$ from comparisons to experimental data.

Multiply both sides of Eqn. 53 by $-2D^2_o(U/U_o)^{-4}$ and integrate to yield:

$$\frac{D}{D_o} = \left(\frac{U_o}{U}\right)^2\left[1 + \frac{8\pi^2}{\pi^2 - 4}\int_{x_o}\frac{\varepsilon D_o^{\,2}}{U\theta^2}\left(\frac{U}{U_o}\right)^{-4}dx\right]^{-\frac{1}{2}} \qquad \text{(EQ 54)}$$

For small wakes:

$$\frac{\theta}{\theta_o} = \left(\frac{U_o}{U}\right)^3 \qquad \text{(EQ 55)}$$

Eqn. 54 becomes:

$$\frac{D}{D_o} = \left(\frac{U_o}{U}\right)^2 \left[1 + \frac{8\pi^2}{\pi^2 - 4}\left(\frac{\varepsilon}{U\theta}\right)\int_{x_o} \frac{U_o}{U} d\left(\frac{D_o^2 x}{\theta_o}\right)\right]^{-\frac{1}{2}} \qquad \text{(EQ 56)}$$

As per Schlichting (1987), a constant value of $\varepsilon/(U\theta) = 0.044$ was used for all wake shapes and pressure gradients. U_o/U represents the pressure gradient effect on wake decay. By the analogy to a nozzle flow, this term is related to the amount of wake stretching in the stator passage by Eqn. 20.

The wake width can be computed using:

$$\frac{\delta}{\delta_o} = \left(\frac{U_o}{U}\right)^3 \frac{\left(\frac{1}{D_o} - \frac{3}{4}\right)}{\left(\frac{1}{D_o} - \frac{3D}{4D_o}\right)\frac{D}{D_o}} \qquad \text{(EQ 57)}$$

Eqn. 56 estimates the change in relative wake depth as a function of axial distance and velocity ratio which represents the free stream pressure gradient. Knowing the relative wake depth, the wake width can be computed from Eqn. 57. The wake velocity profile is computed from Eqn. 45.

Eqns. 32, 40, 45, 56 and 57 represent the complete wake decay model which includes the effects of both stretching and viscosity.

5.4 Summary

The work of Adamczyk (1996) which was summarized relates the unsteadiness present in the flow field to mixing loss. This provides a framework from which to evaluate how the mechanisms which act on a rotor wake as it is convected through a stator passage impact the production of mixing loss in the stator passage.

The rotor wake in the stator passage is decayed by two mechanisms: wake stretching and viscous dissipation. A wake decay model drawn from the work of Hill et al. (1963) was presented which includes the effects of both decay mechanisms. The model uses an analogy between lengthening of a segment of mass passing through a convergence and the wake stretching that occurs in a stator passage. Viscous dissipation effects are included by an eddy viscosity assumption in the model.

The first step in using the decay model is to estimate the rotor wake stretching that occurs in the stator passage. The derivation of a wake length relationship from the work of Smith (1955) and Adamczyk (1996) was shown. This relationship depends only on the stator inlet and exit velocity triangles. Having established the wake length ratio, the velocity ratio across the convergence is established also. The second part of the wake decay model is the decay of the velocity field due to viscous dissipation and pressure gradients. An outline of the derivation from Hill et al. (1963) was presented. The wake length ratio calculated in the first step is used to set the velocity ratio, representing the pressure gradient, in the wake decay model. The decay model is then evaluated by marching with axial distance to determine the wake shape. The results from the wake decay model will be compared to experimental data using the idea of the disturbance kinetic energy and further used to determine the relative contributions of wake stretching and viscous dissipation to rotor wake decay in the stator passage.

6. DATA ANALYSIS

The application of the wake decay model to the estimation of wake stretching and viscous dissipation contributions to the decay of a rotor wake in the stator passage is presented in this chapter. The results are consistent with the experimental data and show that wake stretching is the dominant rotor wake decay mechanism in the stator passage with viscous dissipation playing only a minor role.

Before results of the model are presented, some background must be established relative to the validity of applying the wake decay model to the flow field of this compressor stage. Because of the assumptions used to derive the model, the stage flow field is evaluated using the simulations and experimental data to determine the errors associated with those assumptions. Following that, determination of the wake stretching from measurements and results from the wake stretching model are compared. Next the measured rotor wake profiles are shown to familiarize the reader with the experimental data. The decay model is then used to predict the decay of a rotor wake at the midpitch location in the stator passage and the results are compared to the experimental data. A more complete survey of the LFA data including other interesting regions of the flow field is found in Appendix B.

6.1 Non-modeled effects

The wake decay model does not include the effect of wake drift, radial velocities, compressibility, or the wake/blade interaction which occurs at the ends of the chopped wake segments. Before applying the decay model it will be shown that these effects are of secondary importance for the compressor stage under consideration.

Rotor wake drift in the stator row as described by Kerrebrock and Mikolajczak (1970) is a result of the lower velocity of the rotor wake fluid compared to the free stream fluid in the relative reference frame. Rotor wake fluid thus has a larger tangential velocity component in the absolute reference frame than the free stream fluid and 'drifts' toward the stator pressure surface. An estimate of the drift velocity indicated that the maximum drift of a wake fluid particle

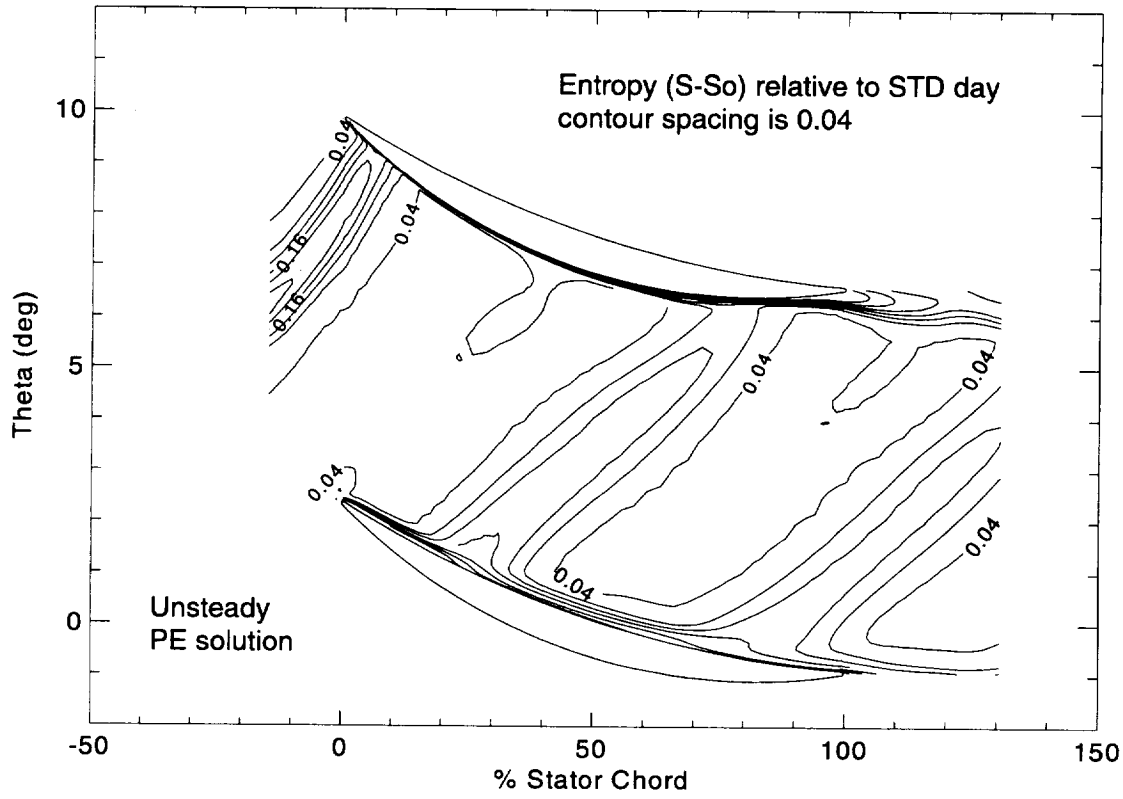

Figure 22. Contours of entropy for a fixed rotor/stator position from the PE simulation.

as the wake convects through the stator passage would be less than 1/3 of the stator pitch toward the pressure surface. The entropy contours from the numerical simulations, shown in Figure 22 for the PE case, suggest that the high entropy rotor wake fluid particles extend across the stator pitch, even at the stator exit. Therefore, wake decay in the stator is not primarily due to the wake fluid drifting to the pressure surface of the stator.

Radial velocity magnitude in the rotor wakes predicted by the CFD simulations is significant at the rotor trailing edge, 12% and 27% of absolute velocity for PE and NS cases respectively. However, at the stator leading edge the radial velocity magnitude is only 6% and 13% of the absolute velocity for PE and NS cases. The radial migration of wake fluid within the stator passage is 5.5% and 10.5% span for PE and NS. These spanwise drift distances were determined by tagging the wake fluid at the stator leading edge and following the convection of the tagged particles through the stator. The flow field was considered sufficiently two dimensional in the core spans of the compressor stator such that calculating wake decay on a geometric 75% span stream surface was considered a reasonable approximation to following a

wake fluid particle.

Compressibility affects both the wake recovery and the calculation of mixing losses. Wake recovery is affected in two ways. First, compressibility affects the mean flow velocities which determine the wake stretching. Both the LFA data and the simulation include this compressibility effect. The simple wake stretching model, which is based on an incompressible assumption, does well in predicting the wake stretching (as will be shown) and thus indicates that compressibility is a small effect. The minor importance of density on wake stretching and mixing is also corroborated by Denton (1993). Secondly, wake recovery is affected because of the assumption that the circulation is constant for inviscid incompressible flow. For compressible viscous flow the circulation around a material segment of mass changes as (Sherman, 1990):

$$\frac{d\Gamma}{dt} = \oint\left(-\frac{\nabla P}{\rho} + \frac{\nabla \bullet \tau}{\rho}\right)d\vec{r} \qquad \text{(EQ 58)}$$

This is a line integral that encloses the segment of mass. The first term on the right hand side is zero if the density is only a function of the pressure. For a stator row where static temperature changes are small, this term should be small. The contribution of this term can be estimated by comparing the relative magnitudes of the change in density across the stator row due to static pressure increase and due to static temperature increase. From the APNASA simulation of the stator row for the PE condition at midpitch, the total increase in the non-dimensional density was 0.019 due to both static pressure and static temperature. The isothermal change in density was 0.0264 and the isobaric change in density was -0.0049 so that 0.0264 + (-0.0049) yields, within the error of this approximation, the total change in density. This indicates that the temperature effects are five times smaller than the pressure effects and the assertion that the pressure term has a small impact on the circulation change is probably justified.

The second term on the right hand side is the divergence of the stress tensor and represents the viscous impact on circulation. Because the rotor wake has decayed significantly before entering the stator row, this term is expected to be small, with the possible exception of near the blade surfaces. Viscous decay of the wake will change the circulation of a material segment. This does not invalidate the wake attenuation due to stretching but reduces the potential benefit. Further treatment of the impact of density and viscosity on circulation is beyond the

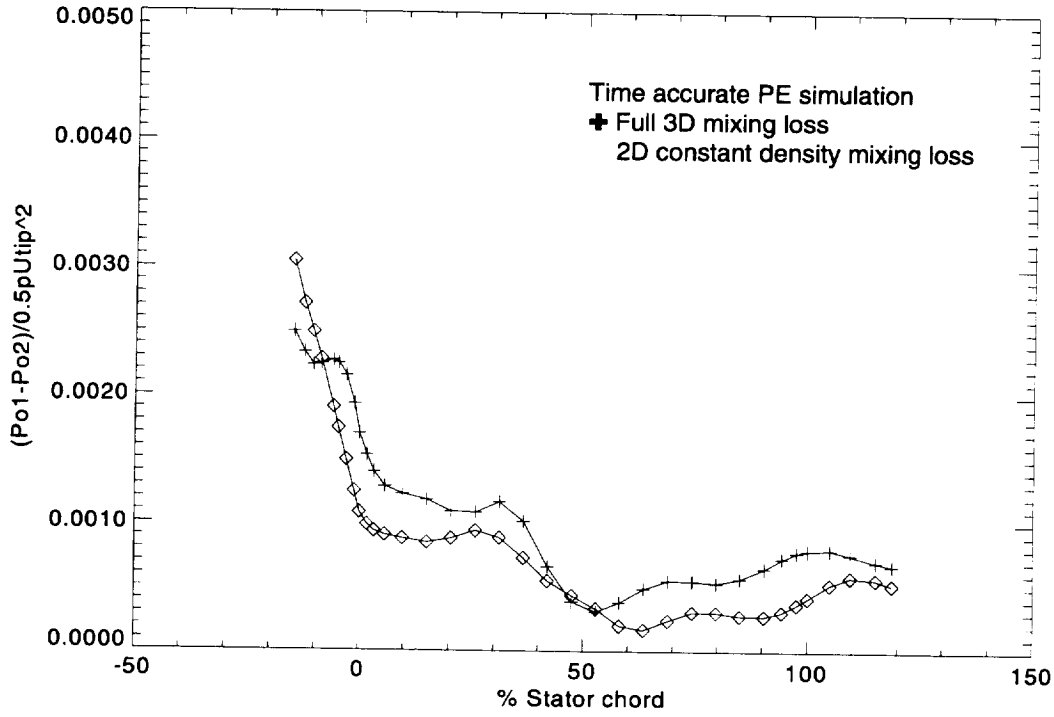

Figure 23. Comparison of 2D incompressible mixing loss results to full 3D compressible mixing loss calculations using the numerical simulations.

scope and intent of this dissertation.

Because the LFA system only measures two velocity components and not density or pressure, mixing loss calculations with the LFA data must be done by assuming 2D incompressible flow. The unsteady simulations are used to estimate the error associated with these assumptions. Figure 23 shows a comparison of the 3D compressible and 2D incompressible mixing loss for a rotor wake at stator midpitch. When evaluated for a rotor wake at midpitch at the stator leading edge, the 2D incompressible mixing loss is in error by -38% for PE and -23% for NS compared to the 3D compressible mixing loss of the rotor wake. At the stator trailing edge, the error is -27% for PE and -18% for NS. The total mixing loss is small compared to the incoming kinetic energy, so the error incurred by the assumptions is a small in absolute magnitude. The simple 2D incompressible mixing loss calculations consistently underpredict the rotor wake mixing loss but will show the correct loss trends. Mixing loss when referred to in the remainder of this thesis is understood to be calculated using 2D incompressible assumptions.

End effects refers to mechanisms such as wake/boundary layer interaction and the stator/

wake gust response. Wake/boundary layer interaction may produce other structures which interact with the wake (Valkov and Tan, 1995). The gust response is a reversible mechanism and is treated in some detail in Chen et al. (1994). Further mechanisms, for instance the stator back-pressuring the rotor, as proposed by Smith (1996) may also impact rotor wake decay and recovery. These additional mechanisms are currently under study and are outside the scope of the project described in this dissertation.

In summary, radial velocities and wake drift are considered secondary effects. Compressibility has minimal impact on wake recovery but does have a known impact on mixing loss calculations. Other effects are present also, but at midpitch where comparisons are made these impacts are minimized. Within the context of the above caveats, application of the wake decay model to this stage is considered reasonable. A more complete survey of the LFA data is contained in Appendix B where rotor wake profiles in other regions of the flow are shown.

6.2 Wake Stretching Measurements and Calculations

The first step in using the wake decay model involves determining the amount of wake stretching. To determine the inlet and exit wake lengths from the data, it must be determined when the wakes are incident with the stator leading edge and incident with the stator trailing edge. The wake velocity field is altered by end effects and is also decayed rapidly in the stator passage. Since this makes it difficult to accurately determine wake lengths from velocity measurements, the following procedure was developed. From the experimental data it was noted that, over a rotor blade passing period, the number of measurements per window was not uniform and that more measurements per window were acquired in the pressure side of the rotor wake region than in the 'core flow' region between wakes. This effect is illustrated in Figure 24 which shows an axial velocity distribution with the measurement distribution superimposed for a stator leading edge midpitch location at the PE operating condition. The relation between measurement distribution and wake location can thus be used to help locate the wake position.

Figure 25 illustrates the wake length determination for the PE case using a contour plot of the number of LFA measurements. Figure 25 is drawn for the rotor cirumferential position for which the wake intersects the leading edge of the upper stator blade. The wake length was

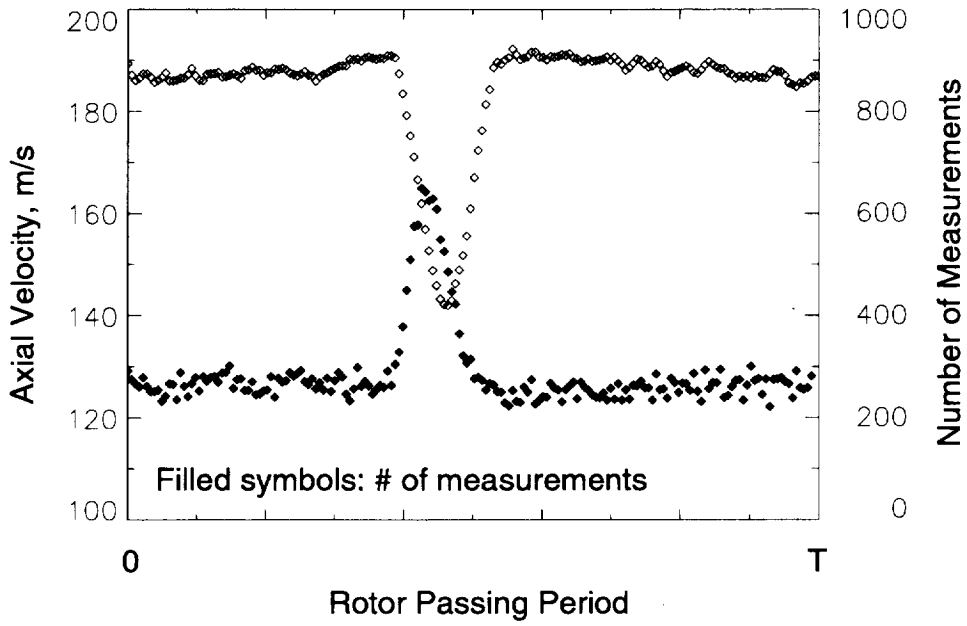

Figure 24. Axial velocity profile and number of measurements profile for PE midpitch at the stator leading edge plane.

measured from the stator leading edge to the intersection of the wake centerline with the stator leading edge stagnation streamline. A similar procedure is followed at the stator exit using a contour plot constructed from data acquired at the rotor blade position for which the rotor wake intersects the trailing edge of the lower blade. There are fewer survey planes downstream of the stator so the wake location is more difficult to determine accurately. There is an addition survey plane at an axial location of 4.2 inches not shown in Figure 25 which was also used to help locate the wake downstream. In the simulations, the wakes are easily identified as high entropy regions (see Figure 22) so their trajectory is simple to track.

Table 5 shows a comparison of wake length ratios determined from the LFA data, the simulations, and Equation 32.In most instances detailed data is not available and the wake stretching would be determined from Eqn. 32. However, in the present work the wake lengths can be determined directly from the experimental data and simulations. A comparison of measured wake lengths to those determined from the simulations shows that the simulations are accurately predicting the wake kinematics. This gives confidence that the simulations are correctly calculating the effects of wake recovery due to wake stretching. When the measured wake

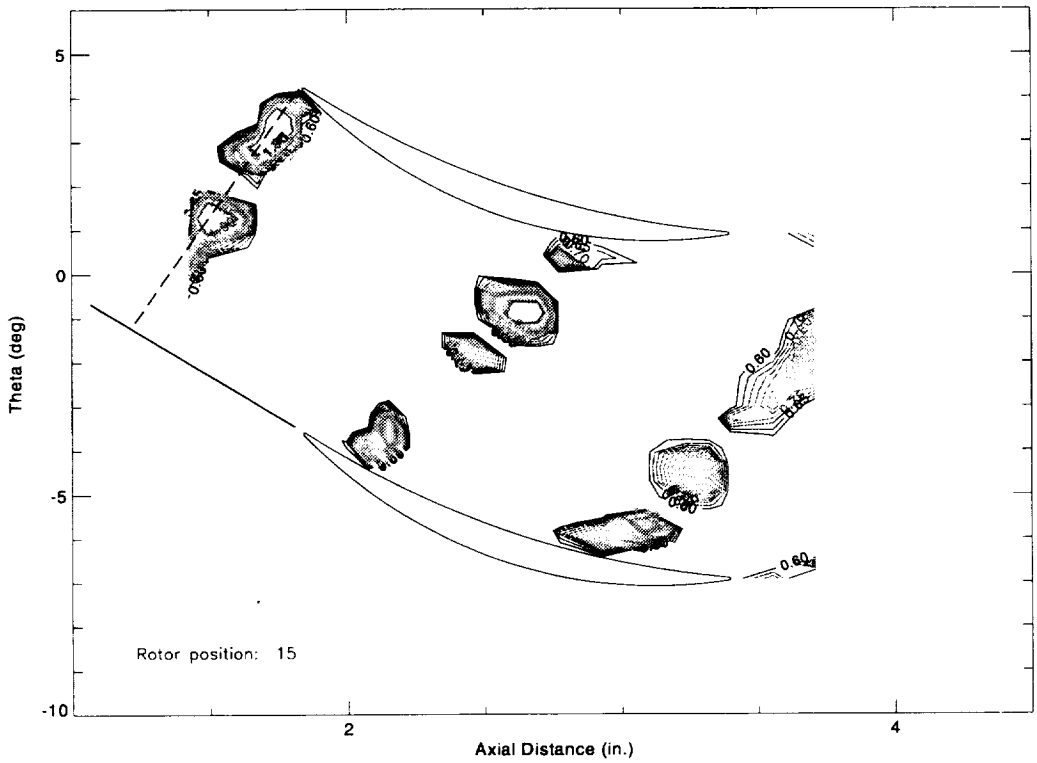

Figure 25. Determination of wake length from experimental data.

Table 5: Wake length ratios as measured from the LFA data and numerical simulations and calculated using Eqn. 32.

	Experiment		Simulation	
	measured	Eqn. 32	predicted	Eqn. 32
PE	1.67	1.52	1.62	1.53
NS	2.14	1.74	2.05	1.81

lengths are compared to those calculated using Eqn. 32 the results show that the equation is a reasonable and simple method for estimating wake stretching.

Now that the amount of wake stretching has been determined, a relevant question to ask is "How much of the rotor wake decay in the stator passage is due to recovery?" The recovery can be determined from Smith's model, Eqn. 18, which is based on wake lengths. The reduction in unsteady kinetic energy is then determined from the recovery using Eqn. 15. The

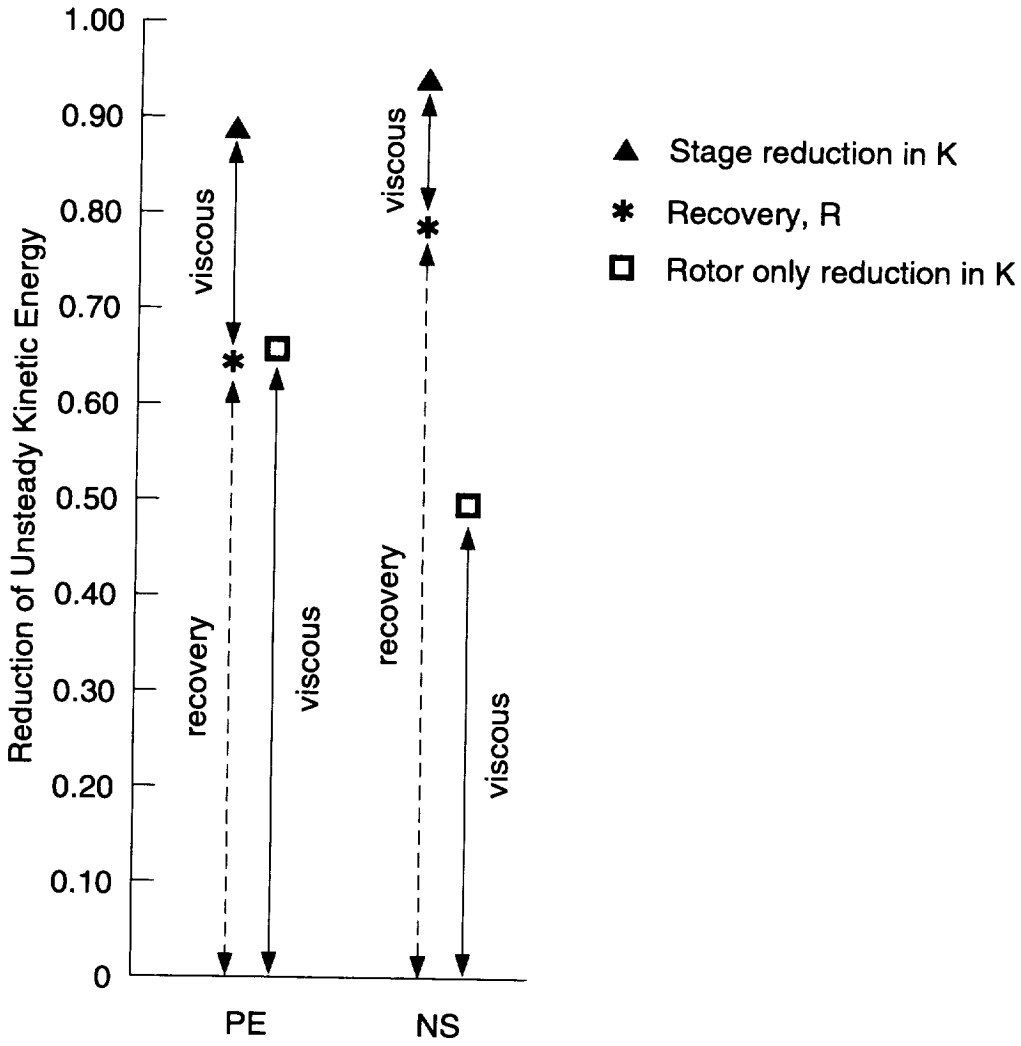

Figure 26. Rotor wake decay in the stator passage in terms of the reduction in the flux of disturbance kinetic energy and predicted recovery determined from midpitch LFA data.

reduction in unsteadiness due to recovery is compared to the total reduction of unsteadiness in the stator passage which is determined by calculating K at the stator leading edge and the stator exit from the LFA data using Eqn. 16. The total reduction of unsteadiness will include both the effects of wake stretching and viscous dissipation. A value of $K=0$ means that no wake remains and the reduction of unsteady kinetic energy is 1.0. Results from these calculations are shown in Figure 26. The figure also shows the reduction in unsteadiness based on the same axial locations and equivalent operating conditions for the rotor only environment, because the rotor only case represents the maximum possible viscous contribution to decay. Several observations can be made from this figure.

First, the amount of rotor wake decay in the stage environment is greater than for the rotor in isolation (compare the triangles to the squares). This also indicates that viscosity alone is not the cause for all of the rotor wake decay in the stage environment, What is most striking is that wake stretching (the asterisks) accounts for a large portion of the rotor wake decay in the stator passage.

The two mechanisms of viscous dissipation and wake stretching act concurrently in the stage environment and Figure 26 shows that the viscous dissipation is reduced in the stage environment. The recovery process is a kinematic process and is dependent on the mean flow velocity field which is relatively independent of compressibility and viscosity. Furthermore, the LFA data shows that the rotor wake decay is most rapid immediately downstream of the rotor trailing edge due to both viscous effects and static pressure gradients in the wake. When the wake reaches the stator leading edge plane, the rate of wake decay has decreased significantly. This is shown more quantitatively later in this chapter. Once the rotor wake enters the stator passage the viscous decay rate is decreased even further because the velocity gradients which drive the viscous dissipation are being decreased by the wake stretching.

These arguments all suggest that the viscous dissipation of the rotor wake in the stator passage is reduced relative to the rotor only environment. However, there is no direct method of measuring rotor wake decay due to viscosity or due to wake stretching from the LFA measurements. A model which includes the effects of both wake stretching and viscous decay is necessary to determine the relative contributions.

6.3 Midpitch LFA Data

Before showing the wake decay model results this section presents some detailed views of the rotor wakes at stator midpitch. Relative wake depth and unsteady kinetic energy are calculated using these profiles and these measured results are compared to predictions from the wake decay model. Presented first is detailed information in the rotor/stator gap and then wake profiles from the stator passage. All velocity profiles are presented as relative velocity magnitude. See Appendix B for detailed velocity component information. Figure 27 shows the measurement locations for the wake profiles shown.

The rotor wake decay rate is highest in the rotor/stator gap. Figures 28 and 29 show the

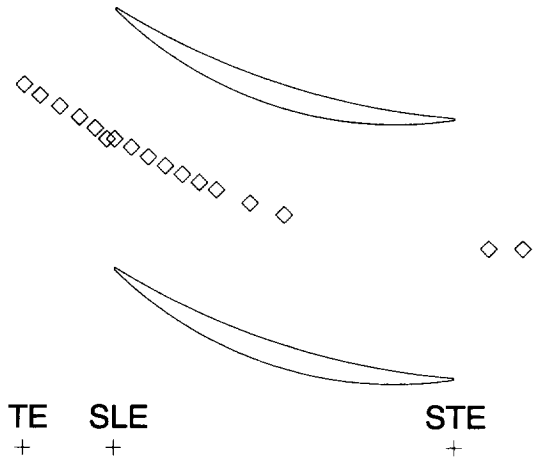

Figure 27. Measurement locations for the midpitch rotor wake data points.

rotor wake profiles approximately along the mean flow direction from the rotor TE to 90% gap. The wake minimum velocity increases rapidly and the wake width increases quickly also. Figures 30 and 31 show selected wakes, also in relative velocity magnitude, through the stator passage. The wake decay model calculations are compared to these profiles.

6.4 Wake decay model results

The rotor wake profile at the stator leading edge plane at midpitch is used to determine the initial relative wake depth and width needed in the decay model. The wake profiles are shown in Figure 32. Note that the rotor relative velocity magnitude, as shown in the figure, was used for the calculations. The stator midpitch location was chosen to minimize the wake gust/stator response interaction which is not included in the model.

The flow turning through the stator row indicated that a linear pressure gradient is a reasonable approximation to the rotor wake stretching that occurs in the stator passage. The absolute flow angle data versus axial position is shown in Figure 33. Eqns. 32 and 37 relate the flow turning to wake stretching. Substituting this flow angle information into these equations yields a wake stretching relation that is linear with axial distance.

The Uo/U term in Eqn. 56 represents the pressure gradient by a change in free stream velocity. For example, a constant value of Uo/U= 1.0 for all axial locations is a zero pressure gradient while a value of Uo/U< 1.0 represents a favorable pressure gradient. A linear varia-

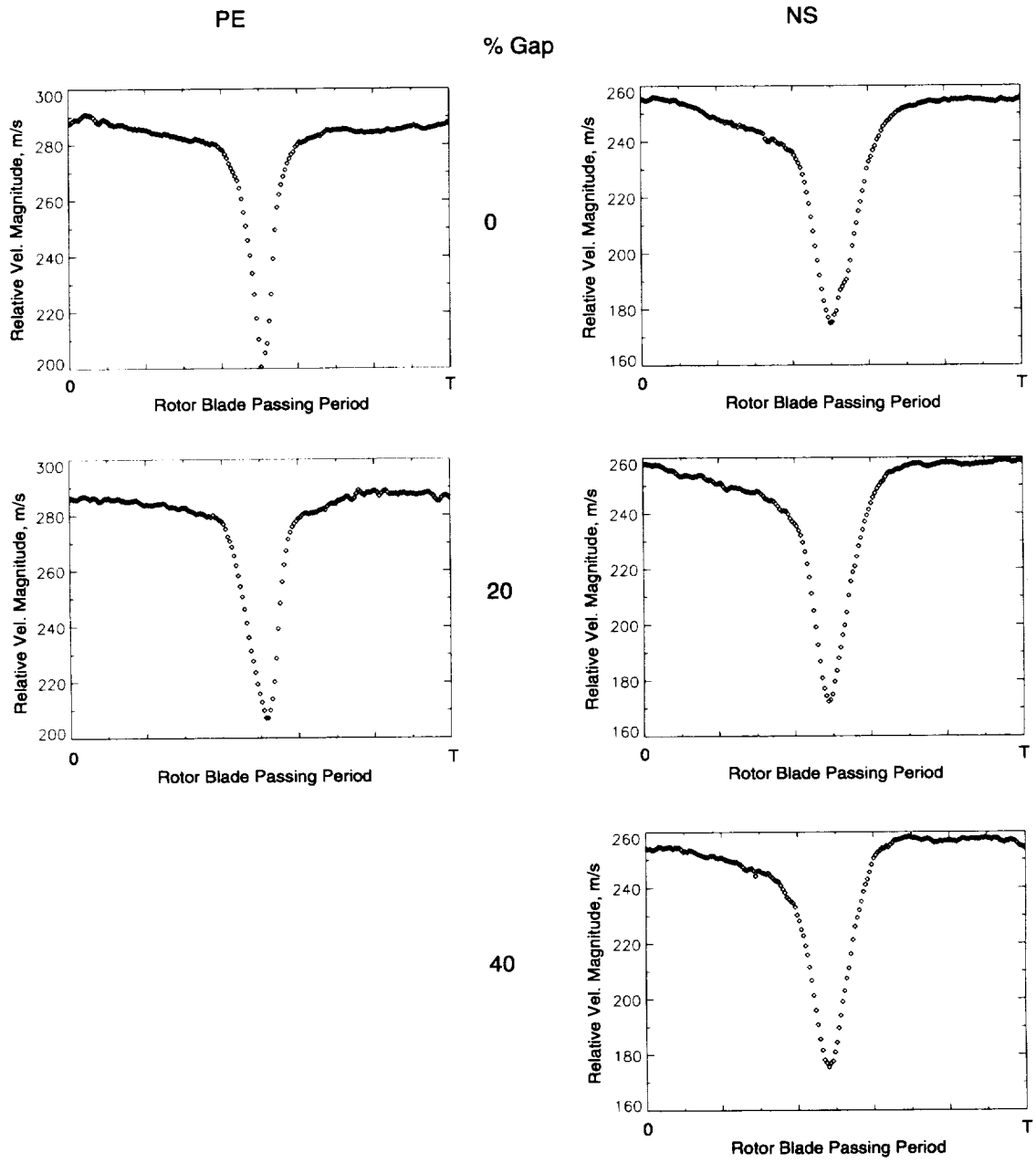

Figure 28. LFA rotor wake profiles in the rotor stator gap along an extension of the stator midpitch line.

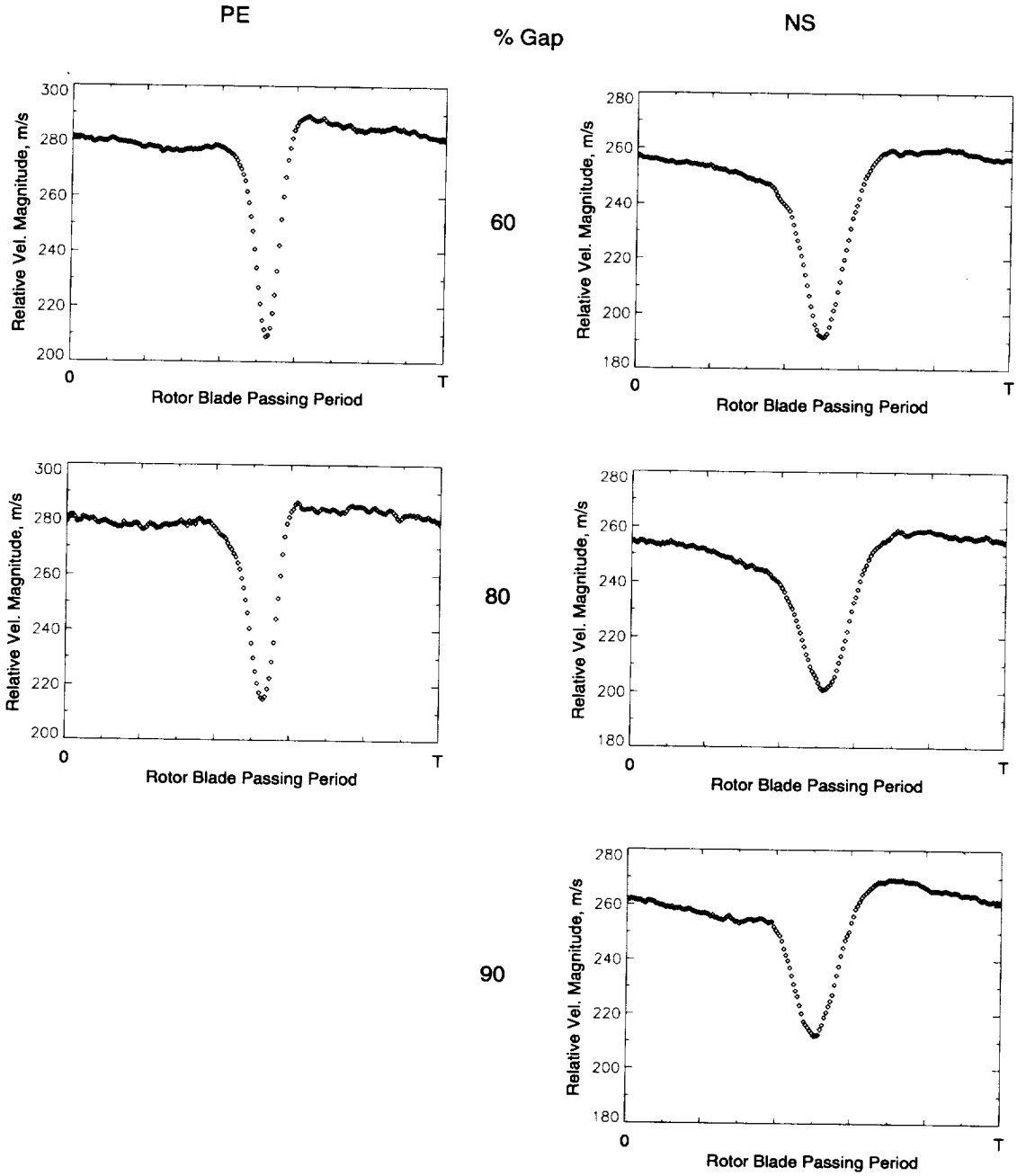

Figure 29. LFA rotor wake profiles in the rotor stator gap along an extension of the stator midpitch line.

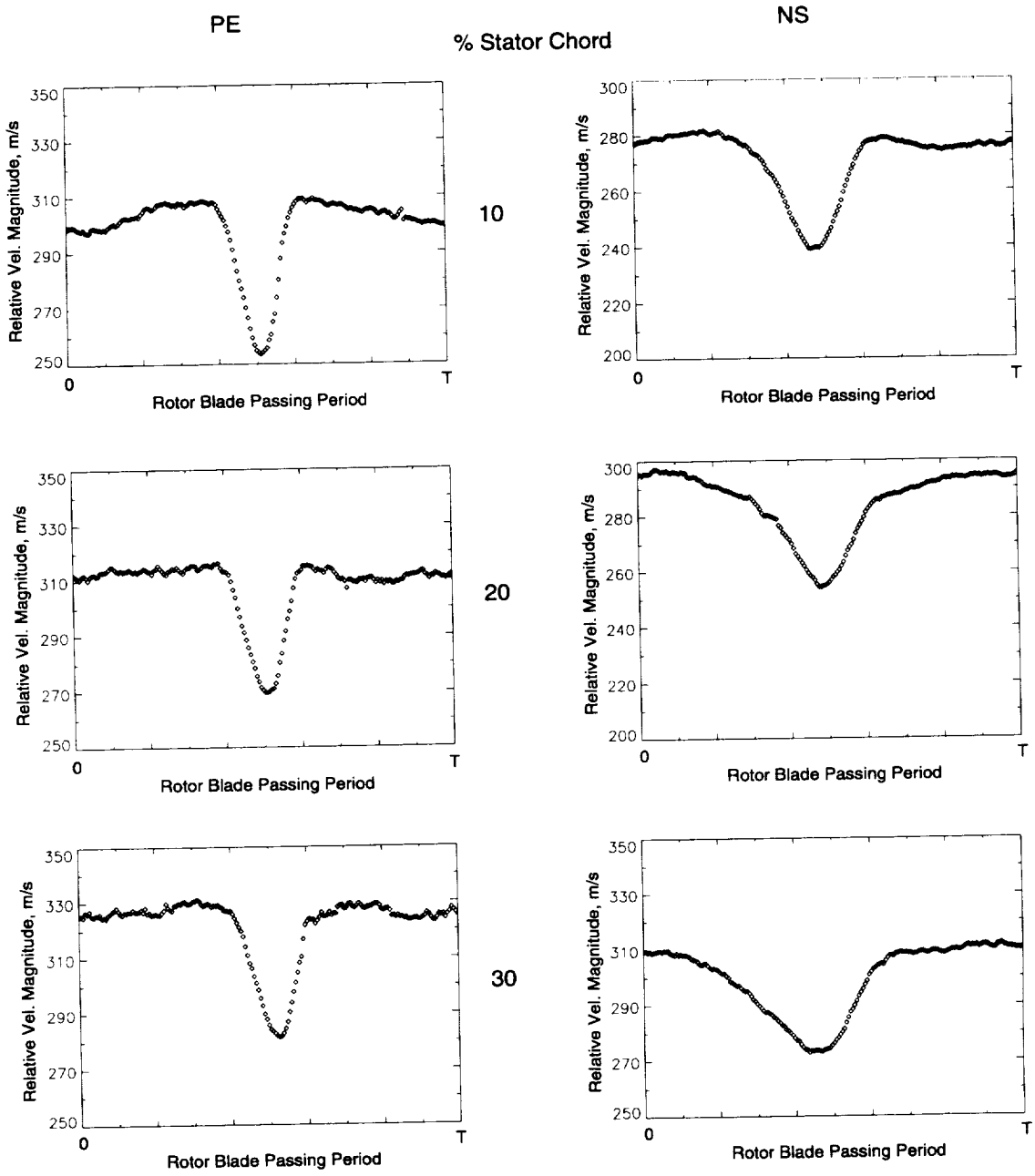

Figure 30. LFA rotor wake profiles in the stator passage at midpitch.

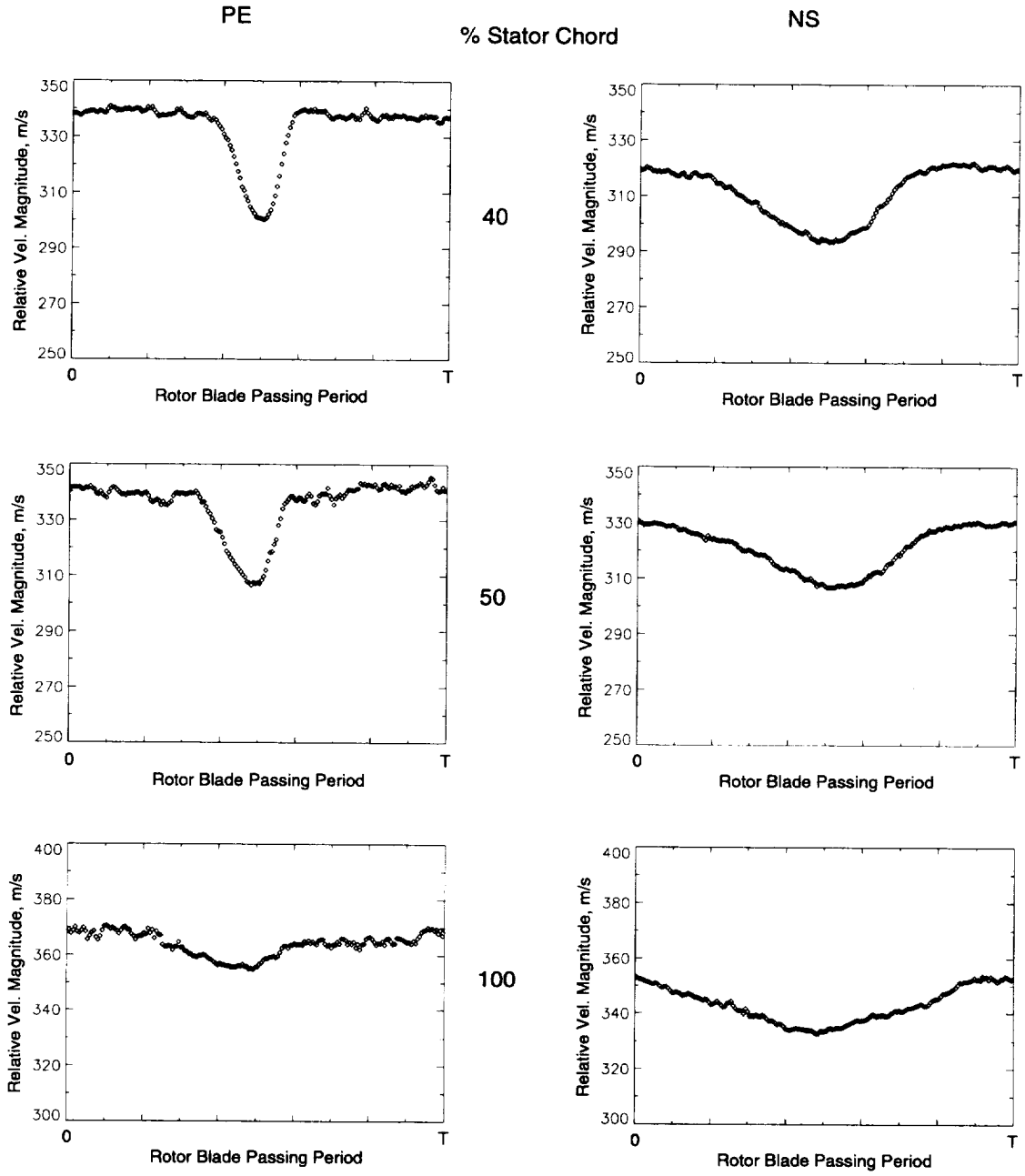

Figure 31. LFA rotor wake profiles in the stator passage at midpitch.

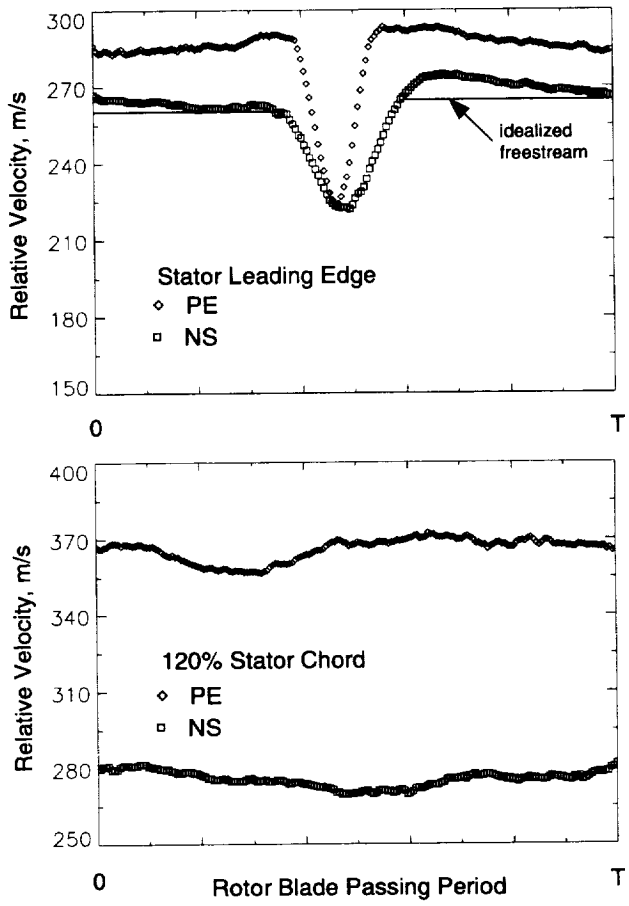

Figure 32. Midpitch wake profiles for PE and NS at the stator leading edge and stator exit planes in the stage environment.

tion of Uo/U in Eqn. 56, was therefore used in the model to represent a favorable pressure gradient such that the velocity ratio at the stator exit was equal to the wake length ratio (see Eqn. 19) as determined from the experimental data. Thus U/Uo= 1.0 at the stator leading edge and varied linearly to U/Uo= 1.67 for the PE case and U/Uo= 2.14 for the NS case at the 100% stator chord axial location.

To determine a relative wake depth from the LFA data the wake edge velocities must be determined. The LFA rotor wake velocity profiles contain some influences of both the rotor wake and the wake/blade interaction even at the midpitch location. The wake depth was assumed to be relatively unaffected by the wake/blade interaction, but the edges of the actual rotor wake were difficult to identify. The measurement distribution was used to assist in locating the edges of the rotor wake in the velocity profiles using plots similar to Figure 24. The

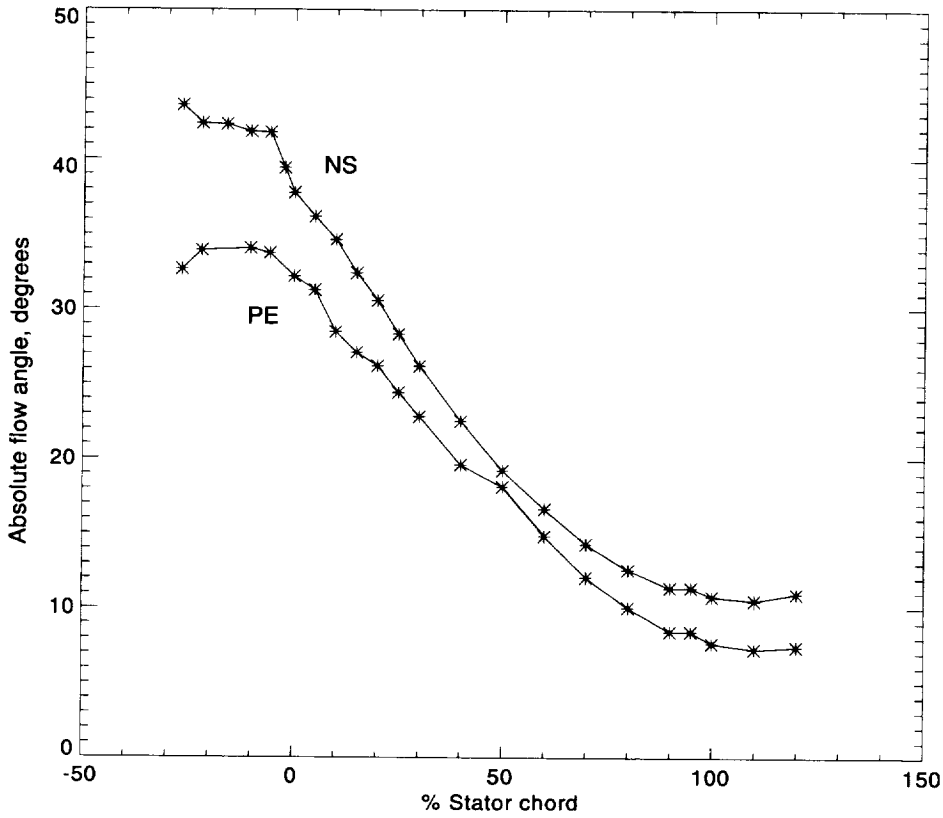

Figure 33. Flow turning at stator midpitch from the LFA data.

peak in the measurement distribution helped to identify the pressure side of the wake and the region of increased measurements helped to identify the wake fluid. The velocity in the regions outside of the rotor wake was considered constant and was set equal to the corresponding wake edge velocity. This results in a 'idealized' LFA rotor wake profile, see Figure 32, for which the wake/blade interaction effects are minimized. The relative wake depth for the LFA data was then calculated from the average of the wake edge velocities and the minimum wake velocity.

To begin the calculation an initial relative wake depth and momentum thickness must be determined at x_o which is the stator leading edge plane. Figure 34 shows the relative wake depth and momentum thickness as a function of stator chord for the PE LFA data at midpitch. There is some scatter in the data so the initial values were chosen as a 'best fit' to the trend of the data at 0% stator chord as shown in the figure. The initial values chosen are given in Table 6.

With the initial conditions set, Eqn. 56 is numerically integrated with x from x_o to the

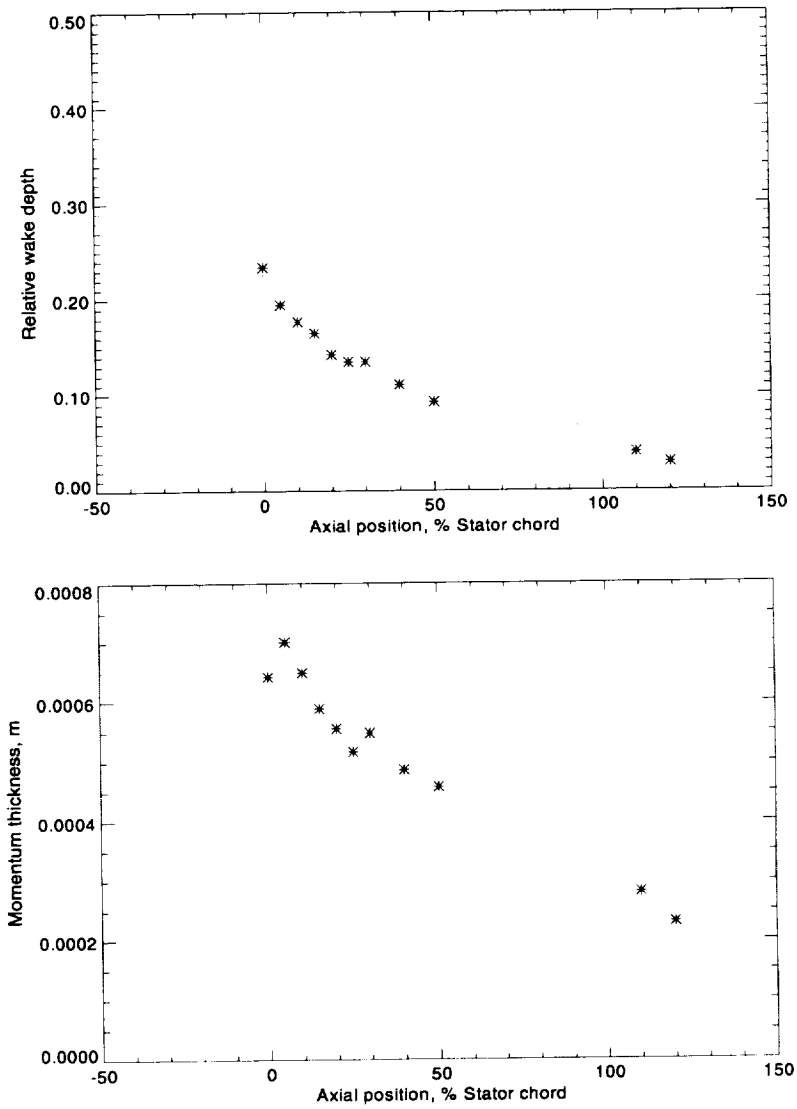

Figure 34. Relative wake depth and momentum thickness for the midpitch PE LFA data.

desired end point. The other wake parameters are then calculated.

The relative wake depth calculated from Eqn. 56 is used to determine a wake width using Eqn. 57 and then a wake velocity profile is calculated using Eqn. 45. To simulate the pressure gradient the model accelerates the free stream flow. Thus the wake profile velocity magnitude is adjusted such that:

$$\int_0^T V dy|_x = \int_0^T V dy|_{SLE} \qquad \text{(EQ 59)}$$

Table 6: Initial values for wake decay calculation.

	D_o	θ_o
PE	0.225	0.00070
NS	0.180	0.00104

where V is the relative velocity magnitude. Eqn. 59 ensures mass conservation as the wake profile shape changes and adjusts the free steam velocity back to the correct level before the DKE calculation. The relative disturbance kinetic energy is calculated from these profiles as:

$$DKE_{REL} = 0.5 V_o A_t (V - V_o)^2 \qquad \text{(EQ 60)}$$

where V_o is the time average relative velocity magnitude. Change in DKE_{REL} will be approximately proportional to the change in mixing loss. The DKE_{REL} for LFA data is calculated in a similar manner using the modified velocity profiles described previously.

A comparison between the model calculation and experimental (LFA) data at midpitch is shown in Figure 35 in terms of a) the relative wake depth and b) the relative disturbance kinetic energy. For the relative wake depth results: the curve labelled *viscous+stretching* is calculated from Eqn. 56, the curve labelled *stretching only* is calculated from Eqn. 56 with the eddy viscosity set to zero, the curve labelled *viscous only* is calculated from Eqn. 56 with the velocity ratio set to 1.0.

The relative wake depth calculations show good agreement with the data in predicting decay due to both stretching and viscosity. The stretching only curve indicates the amount of depth change due only to the lengthening of the wake segment. The viscous only curve indicates how a rotor wake will decay in a zero pressure gradient due to viscous dissipation alone. This is analogous to a rotor only environment and represents the maximum decay possible due to viscosity. These results indicate that wake stretching is the primary decay mechanism and that the viscous decay contribution is of secondary importance. Also, the viscous contribution is decreased in the NS case due to an initially lower viscous decay rate but also due to increased wake stretching.

Part b) of Figure 35 shows the model calculation results in terms of relative disturbance kinetic energy for stretching+viscous, stretching only, and viscous only decay. The agreement with the data is not as good as that for the wake depth. The disturbance kinetic energy depends

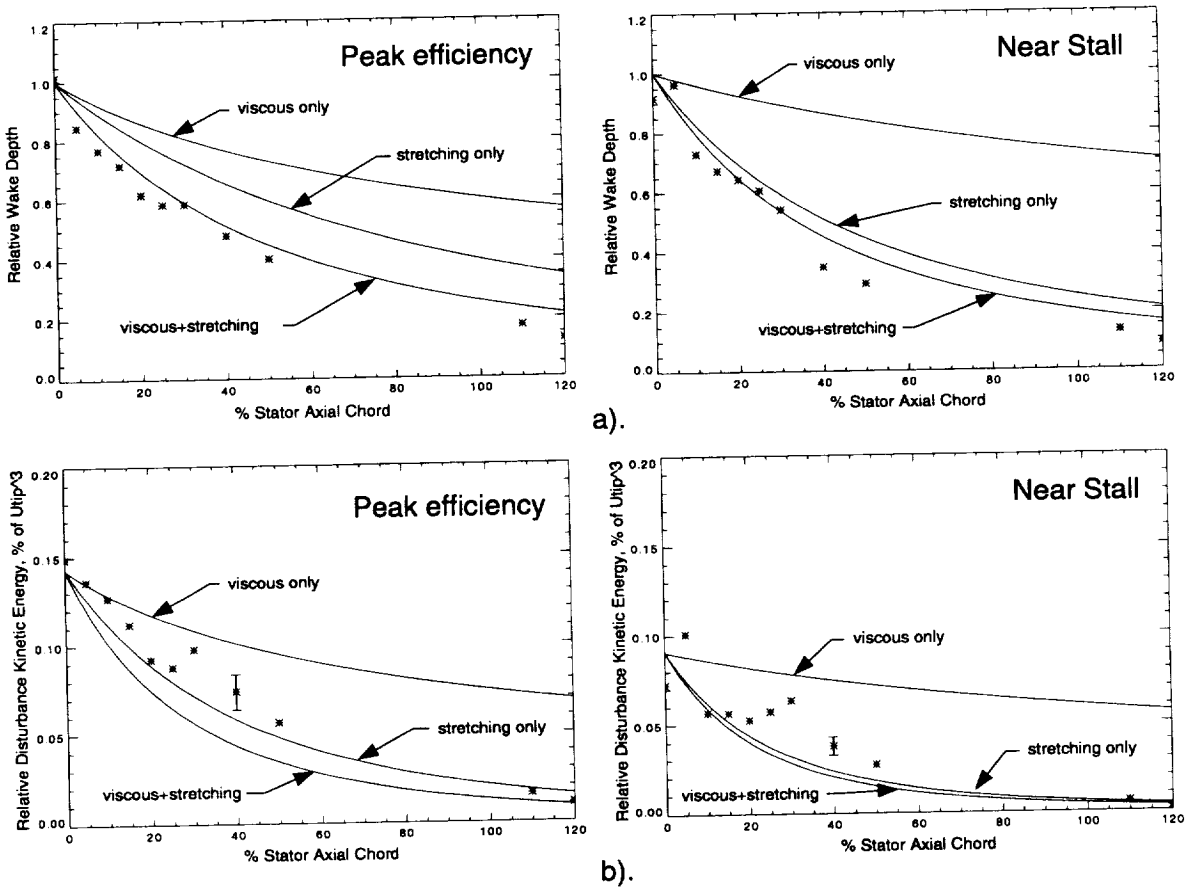

Figure 35. Comparison of LFA data to wake decay model predictions for the PE and NS cases.

upon the wake decay model calculating both the wake width and depth changes correctly. Additionally, the LFA data calculations also contain some of the non-modeled effects. The comparison of disturbance kinetic energy is a more rigorous test of the wake decay model. Interestingly, the stator exit DKE is well predicted by the model even though the path to the exit condition shows disagreement. This implies that on an overall basis, the wake decay model is doing a good job of modeling the relevant mechanisms.

A subtlety of the data analysis should be mentioned. The distance used in the wake decay comparisons is % stator axial chord. This unit of measure is the most practical and easy to understand. However, the viscous decay is a function of the path length that a particle of fluid travels. The particle path length for a given axial distance increases as the rotor loading increases. Thus the wake particles have slightly different paths for the same axial distance

through the compressor stage for different operating conditions and the rotor only versus stage configuration. The extra length travelled is small but estimates of the viscous loss in the rotor/ stator gap will include some additional loss due to path length increase for the NS case.

Decay in the stator passage is also based on axial distance instead of path length. The decay model could be improved by using actual path length but this would require much more detailed information about the stator flow field. The model as it is now applied is sufficient to make the assertions of this dissertation, especially since the viscous decay contribution in the stator is small.

6.5 Summary

Numerical simulations were used to evaluate mechanisms which are not included in the decay model and showed that they are of secondary importance for this case.

The wake decay model was applied to a rotor wake at stator midpitch for both the PE and NS operating conditions. Results from the model compared favorably in terms of relative wake depth and less favorably, but still adequately, for the disturbance kinetic energy. The results indicate that wake stretching is the primary wake attenuation mechanism in the stator passage. The wake decay model, although not perfect or all inclusive, can be used to draw some conclusions about the wake recovery process in relation to viscous dissipation.

7. IMPLICATIONS FOR STAGE DESIGN

The combination of Eqn. 32 for wake stretching and Eqn. 56 for wake decay, provides a simple method for predicting the benefit of wake recovery in reducing rotor wake mixing losses. This chapter analyzes the results from the rotor wake decay model in terms of mixing loss. Some observations on the implications of these results for stage design are explained.

7.1 Mixing Loss Audit

Assuming 2D incompressible flow, the wake decay model was used to perform an audit of rotor wake decay mixing losses for rotor wake profiles at the rotor trailing edge, stator leading edge, and stator exit axial positions. Wake profiles from these axial locations for the isolated rotor case were used to determine the mixing losses that represent the maximum possible viscous mixing without the effects of wake stretching. In the stage environment measured wake profiles at near the rotor trailing edge and stator leading edge were used in the decay audit along with the wake profiles at the stator exit determined from the decay model. It is not possible to measure the wake at exactly the rotor trailing edge, so the loss in the gap may be underpredicted slightly due to mixing that occurred prior to the measurement location. The final resolution of this issue depends on the full unsteady simulations and the loss audit will be updated at that time. For consistency, the measured profiles of relative velocity magnitude are fit using the decay model wake shape definition, Eqn. 45, before the wake profiles are passed through the mixing loss calculation.

The mixing loss results are shown in Figure 36. This analysis compares the amounts of mixing loss which occur downstream of the rotor trailing edge. In the stage environment from the rotor trailing edge to stator leading edge, 27% and 46% of the possible wake decay has occurred for PE and NS, respectively, all of it due to viscous mixing which generates loss. A portion of the larger NS viscous loss is due to the longer path length of a particle of the NS wake fluid. All of this loss occurs before wake stretching can have an impact.

The wake velocity profile at the SLE plane determines the amount of mixing yet to occur

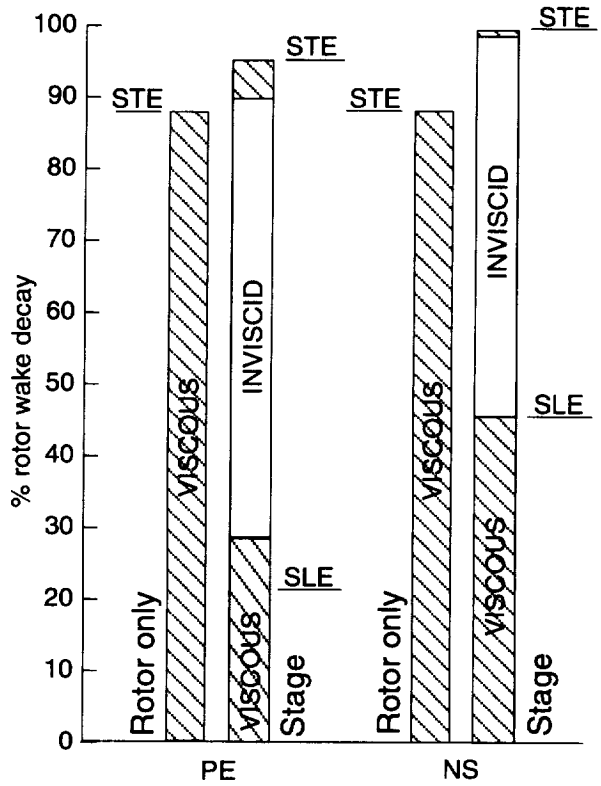

Figure 36. Rotor wake decay audit (0% represents the rotor trailing edge location).

and thus the maximum reduction of mixing loss due to recovery that could occur. Of the remaining rotor wake decay possible at the SLE, 63% for PE and 52% for NS occurred by inviscid stretching of the rotor wake in the stator passage involving no loss. Only small amounts of rotor wake mixing loss occurred in the stator passage because of viscous mixing. The rotor wake is not completely decayed at the stator trailing edge and thus the rotor wake mixing loss does not total 100% at the stator trailing edge for the rotor only results or stage results.

The rotor only loss bars represent the rotor wake mixing loss that occurred from the rotor trailing edge to the stator trailing edge in the absence of the stator row. This result shows not only that the rotor wake decay is greater in the stage environment, but also that the viscous contribution to the decay is much reduced.

On a side note, the rotor only results are not strictly at zero pressure gradient. A contraction in the flow path downstream of the rotor at the stator row location leads to a small accel-

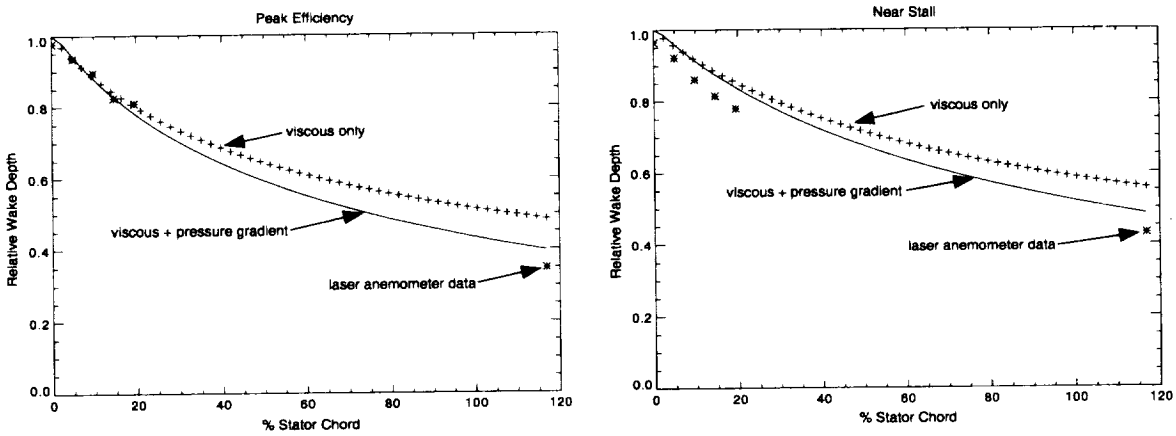

Figure 37. Rotor wake decay for the rotor in isolation experiment.

erating pressure gradient which will tend to increase the overall rotor wake decay. Figure 37 shows a calculation of the rotor wake decay from the stator leading edge downstream for the rotor in isolation experiment. The effect of this pressure gradient is less than 10% of the total rotor only decay for both PE and NS cases based on the mixing loss being proportional to the wake depth squared. The rotor only decay results presented will actually slightly overpredict the decay due to viscosity since a small portion of the observed decay is also due to the pressure gradient.

Figure 37 also indicates that the eddy viscosity assumption used in the wake decay model is reasonable since the experimental measurements and predictions of rotor wake decay are in good agreement for a situation where the wake decay is primarily due to viscosity. This result further strengthens the validity of the rotor wake decay calculations for the stage environment shown in Figure 35 from the previous chapter.

7.2 Design Implications

The reduction in mixing loss due to wake stretching implies that using loss correlations based on isolated rotor or cascade data may be misleading for multistage design. The wake mixing loss implied by cascade data will not be realized in the stage environment. Wake stretching must be accounted for in the proper assignment of losses to components. For example, rotor efficiency inferred from stage measurements would overpredict the rotor efficiency.

Since a significant amount of mixing loss occurs before the rotor wake enters the stator

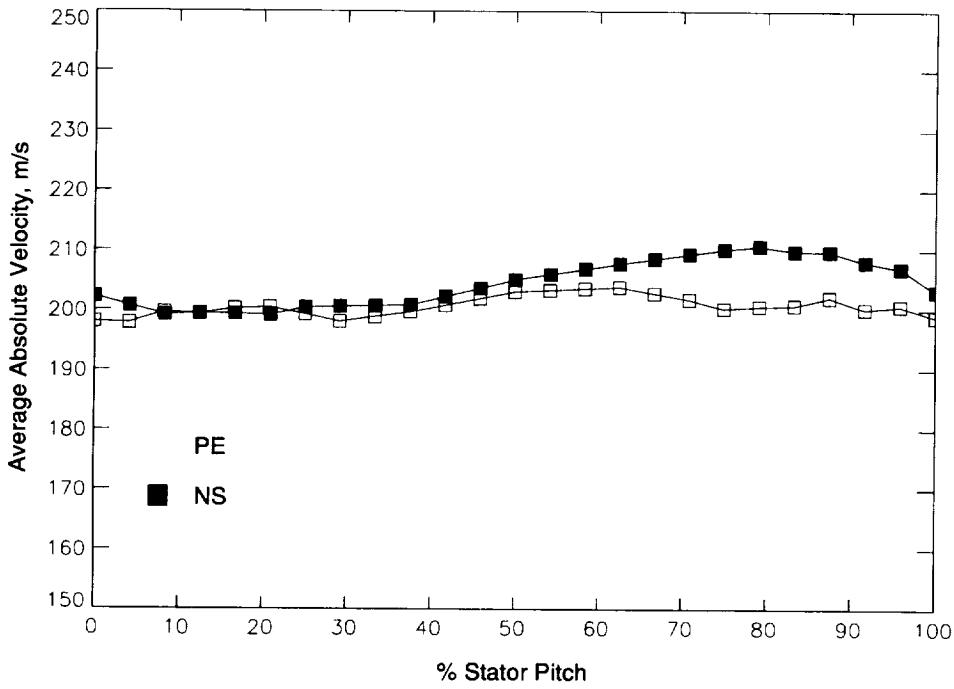

Figure 38. Time average absolute velocity at the rotor trailing edge.

passage, closer axial spacing of blade rows to capture the rotor wake earlier would be beneficial. An efficiency gain of 1.2 points due to closer axial spacing was achieved in a four-stage low speed compressor (Smith, 1970). Of this efficiency gain, 0.52 points was attributed to wake recovery and the remainder attributed to other mechanisms, for example tangential variations of total pressure caused by the downstream stator imposing non-uniform back pressure on the rotor ahead of it (Smith, 1996). Unfortunately, axial blade spacing is normally set by mechanical considerations and is not easily changed.

Predicting efficiency gains from capturing the rotor wake earlier assumes that the closer spacing would not cause increased losses in the rotor and/or stator due to potential field interactions or stronger wake/blade interactions. The stator velocity field impact on the rotor was small at 75% span in the stage used in the present work. As shown in Figure 38, the circumferential variation of the absolute velocity at the rotor trailing edge was 2.5% as measured by the LFA system at the NS operating condition where the interaction was strongest. This might imply that closer spacing is possible without greatly increasing interactions. The available data does not allow any more definitive statement. Because of the small interblade gap, no

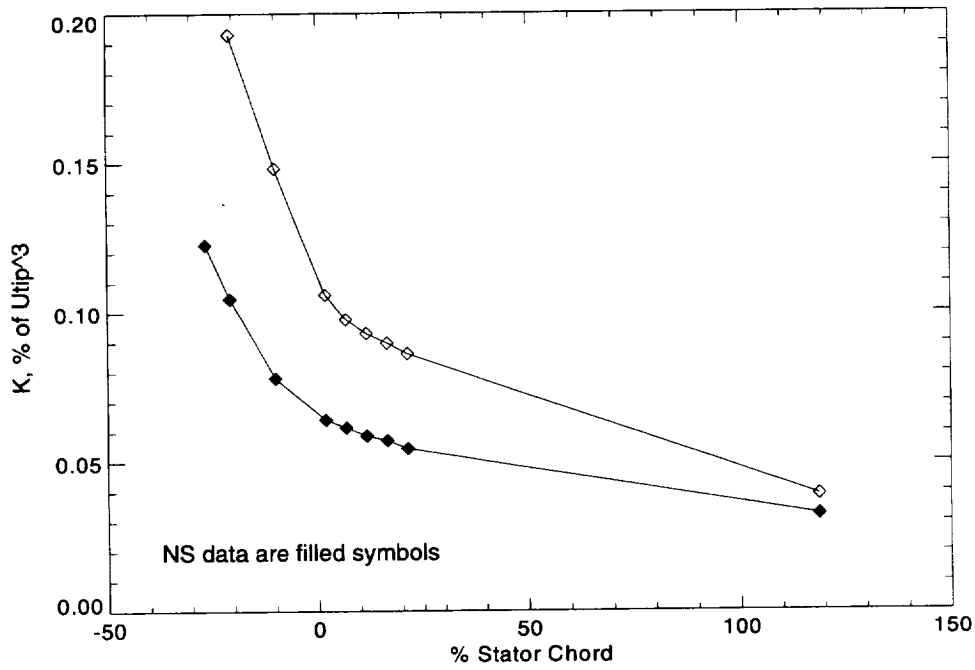

Figure 39. Rotor only wake decay in terms of disturbance kinetic energy from LFA data.

rotor performance measurements are possible in the stage configuration and nothing more definitive can be said about rotor performance either at this time. Due to the difficulty involved with changing blade spacing in a physical experiment, the sensitivity of rotor performance to blade spacing might be more effectively studied using numerical experiments.

An effect similar to closer axial spacing can be achieved by reducing the viscous decay rate of the rotor wake. The viscous decay rate immediately downstream of the TE is dependent on the shear velocity and the static pressure differences across the wake (the assumption of constant static pressure across the wake does not hold in this region). The wake decay immediately downstream of the rotor trailing edge is very rapid compared to the decay rate at the stator leading edge, see Figure 39. A small separation at the rotor TE may reduce the shear velocity and static pressure difference and thus reduce the viscous mixing rate. Denton (1993) found that a mild separation at the trailing edge only mildly increased profile loss. The effect on base pressure drag is not clear. Therefore, this suggestion is speculative and needs further investigation.

By designing stages which use the wake recovery process to its full advantage, higher stage loading may be possible. As rotor blade loading is increased, profile loss due to thicker

boundary layers and thus rotor wake mixing loss would also increase. However, in the stage environment a high percentage of the rotor wake mixing loss could be recovered in the stator row. This recovery would offset some of the higher rotor profile losses and thus might allow higher stage loading without incurring large efficiency penalties. The overall efficiency effect is dependent on the effect of larger rotor wakes on losses in the stator row. This trade-off is not currently known.

Recovery is enhanced by increased overall wake stretching and by stretching the wake sooner in the stator passage. For the NS case a higher percentage of mixing loss is recovered in the stator passage relative to the PE case. Front loaded stators (as in the NS case) turn and stretch the wake sooner in the stator passage which further reduces the viscous decay contribution. Front loading also enhances the wake/blade response attenuation of the wake as seen on the leading edge suction surface of the stator in Figure 15. This attenuation occurs because the stator generates a pressure response to the presence of a rotor wake passing over the surface. This wake/blade response is also a reversible process and is discussed by Chen et al. (1994) for the case of a stator wake being chopped by a downstream rotor.

8. CONCLUSIONS

Two-component laser anemometer measurements of rotor wakes were acquired downstream of a rotor in isolation and in a stage environment at 75% span at two operating conditions. Measurements in the stage were concentrated in the rotor/stator gap and through 20% stator chord and therefore allowed detailed analysis of the rotor wake behavior in these regions. Additional measurements were acquired at the exit of the stator passage to observe the rotor wake remnants exiting the passage. A time-accurate 3-D Navier Stokes simulation of the stator passage was also done to aid in interpreting the data.

Analysis of the measurements showed that wake stretching is the primary decay mechanism for rotor wakes in the stator passage and that wake decay due to viscous effects is greatly reduced in the stage relative to the rotor only case. A model for the rotor wake decay that includes both the effects of wake stretching and viscous dissipation was developed by drawing an analogy between the transport of a wake through a converging passage and the transport of a rotor wake through the stator passage. The model consisted of two parts, the wake stretching model and the wake decay model. The wake stretching model provides an estimate of the wake lengthening in the stator passage and is based only on stator inlet and exit velocity triangles. From the analogy to a converging passage, the amount of wake stretching determines the pressure gradient for the decay model. The decay model is then integrated with axial distance to calculate the decay of the wake profile due to both wake stretching and viscous effects. Since the wake decay model only requires knowledge of the inlet and exit velocity triangles and an assumed rotor wake profile, the model is simple enough to be used for design purposes.

The wake decay model was used to predict the decay of rotor wakes in the stator passage of the test compressor for the peak efficiency and near stall operating conditions. The results from the model were in good agreement with the measured wake decay behavior and showed that inviscid wake decay due to stretching provides a means of tailoring a compressor stage design to avoid some of the loss associated with the entirely viscous decay of a rotor wake. These results also indicate that the use of isolated rotor or cascade loss correlations for multi-

stage compressor design may be misleading because the total wake mixing loss determined for the isolated blade row will not be realized in a stage environment. Finally, the present results lead to the following comments on stage design features which can influence the balance between viscous dissipation and wake stretching:

- Axial spacing of blade rows

  In a compressor stage, a significant amount of rotor wake decay has already occurred by viscous dissipation before the wake enters the stator row. Some of this loss can be avoided by moving the stator row closer to the rotor trailing edge. This assumes that losses in the stator row are unchanged by the influence of deeper rotor wakes.

- Reduced rotor wake shear

  An effect similar to reduced axial spacing could be achieved by a reduction in the rotor wake shear which will reduce the rotor wake viscous mixing in the axial gap between rotor and stator rows. Such a reduction might be achieved by designing for a small amount of separation near the rotor trailing edge, thus broadening the wake width and reducing the shear on the sides of the wake.

- Front loading of stators

  Front loaded stator blades stretch the rotor wake inviscidly earlier in the stator passage and further reduce the already small amount of viscous dissipation involved in that row. Front loaded stators also enhance the wake/blade interaction attenuation of the wake near the stator leading edge suction surface. This mechanism also reduces the wake velocity gradients in a reversible way.

9. FUTURE RESEARCH

The logical continuation of the current project is to identify and quantify the rotor/stator interaction mechanisms other than wake stretching. Smith (1996) using the ideas of wake recovery could only account for 0.52% of the 1.2% increase in efficiency of a four-stage compressor with closer axial spacing (Smith, 1970). Smith (1996) postulated three additional mechanisms: thinning of boundary layers due to static pressure effects, non-uniform back pressuring of the rotor, and increased unsteadiness due to closer blade row spacing. There may be other as yet unidentified mechanisms at work also. Time-accurate computational codes have advanced in speed and accuracy to the point that a numerical investigation of these additional interaction mechanisms is now possible. Results from the numerical simulations would guide any future experimental efforts.

Another related problem, which is of increasing interest, is stator/transonic rotor interaction. A quick way to increase the performance of a compressor is to use a single or even multiple transonic stages. This problem adds the additional complexity of a wake/shock interaction.

Further refinements to the wake decay model are possible. Work is currently underway to develop a transport model for the wake convection through the stator passage. This model will eventually be added to the APNASA code so that wake stretching will be correctly modeled in the code.

The behavior of the rotor tip clearance flow in the stator passage is also not well understood. In a transonic machine the tip clearance 'vortex' appears as a region of low momentum fluid much like a wake. If this is the case, the ideas of recovery would also apply to this region of the flow. However, if the clearance flow behaves like a vortex, the vorticity would be aligned in such a way that wake stretching would amplify instead of attenuating the vortex. This may be the case in subsonic rotors. Detailed measurements in this region are needed to investigate these problems.

APPENDIX A: PERFORMANCE DATA

This appendix presents a detailed view of the rotor and stage aero performance data. Aero performance measurements are acquired with 18 degree wedge probes, which measure static pressure and flow angle, and combination probes which measure total pressure, total temperature, and flow angle. Both probes null to the mean flow direction using the side static pressures for the wedge probe and the side cobra pressures for the combination probe. The probes were calibrated in a jet for Mach number and pitch angle sensitivity. The measurements were then corrected for Mach number and estimated pitch angle. The estimated pitch angle came from a 3D Navier Stokes computation.

The compressor has upstream and downstream measurement locations at -1.67 inches axial location and 4.2 inches axial location respectively. A wedge and a combination probe were installed at fixed circumferential locations at the upstream measurement location. The downstream wedge probe was also mounted at a fixed circumferential location. The downstream combination probe was mounted in a circumferential pad which allowed circumferential traverses in addition to radial movement.

For the rotor only performance measurements, the steady state flow field variations in the circumferential direction were considered negligible and the combination probe was only traversed radially. For the stage performance measurements, the combination probe was traversed circumferentially through one stator pitch with the stator wake in the center of the survey. The orifice mass flow, rotational speed, total pressure, total temperature, static pressure, and static temperature are all corrected to Standard Day conditions using the upstream survey plane as a reference.

Overall performance is calculated from mass averaged total pressures and energy averaged total temperatures as follows:

$$\frac{\overline{P_2}}{\overline{P_1}} = \left[\frac{\int_{hub}^{tip} (P_2/P_1)^{(\gamma-1)/\gamma} \rho V_z r dr}{\int_{hub}^{tip} \rho V_z r dr} \right]^{\gamma/(\gamma-1)} \quad \text{(EQ 1)}$$

$$\frac{T_2}{T_1} = \frac{\int_{hub}^{tip} (T_2/T_1) \rho V_z r dr}{\int_{hub}^{tip} \rho V_z r dr} \quad \text{(EQ 2)}$$

where subscript 2 and 1 refer to the downstream and upstream measurement locations respectively. In the stage environment the total pressure and total temperature are first energy and mass averaged, respectively, across the stator pitch similar in form to the above equations, then the values are averaged in the radial direction as above. The adiabatic efficiency is:

$$\eta = \frac{(\overline{P_2/P_1})^{(\gamma-1)/\gamma} - 1}{(\overline{T_2/T_1}) - 1} \quad \text{(EQ 3)}$$

Weight flow rate is calculated as the average of the orifice flow rates at all of the radial locations.

A.1 Rotor Only Data

The overall performance information is given in Table 7 for the rotor only tests.

Table 7: Aero performance for rotor only test.

	Mass Flow, kg/s	PR	TR	Efficiency, %
PE	17.3	1.44	1.12	92.0
NS	14.8	1.54	1.15	85.5

The radial profiles of total pressure ratio, total temperature ratio, static pressure, and efficiency are shown in Figure 40 for the PE and NS case. The radial profiles of axial velocity and flow angle are shown in Figure 41 for the PE and NS cases. The rotor tip speed is 1192 ft/s.

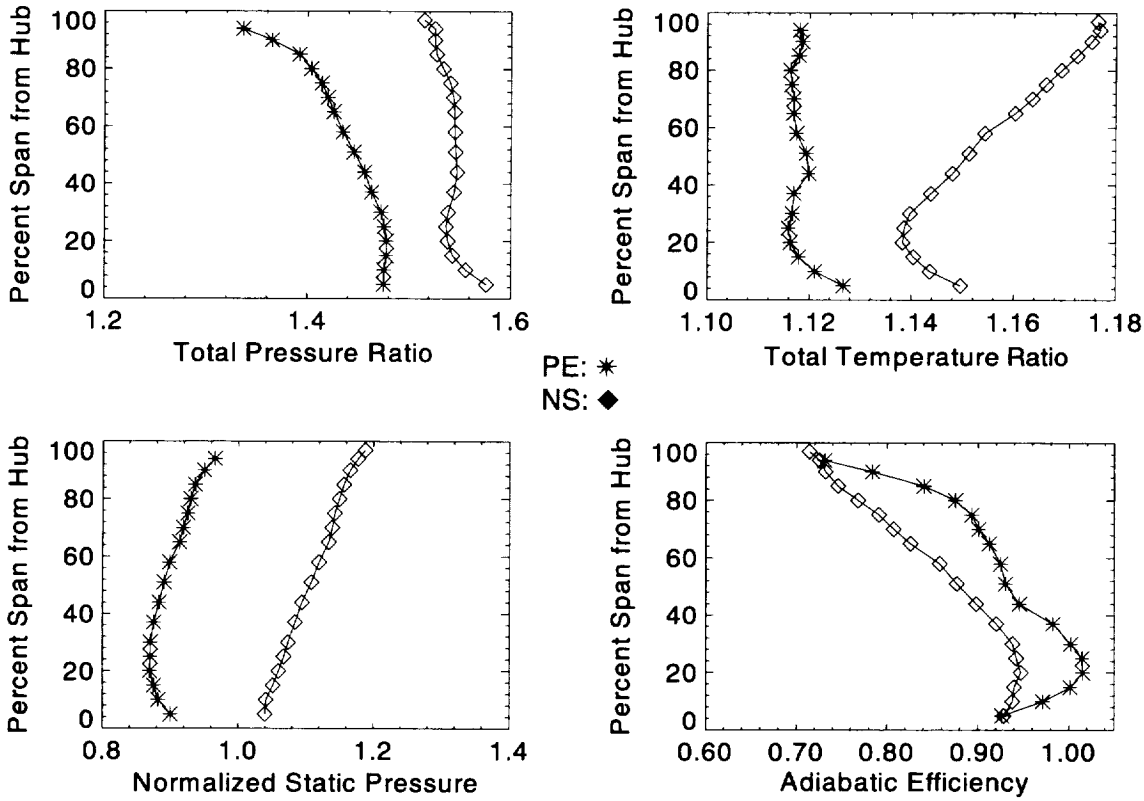

Figure 40. Radial profiles of performance parameters for the rotor only experiment.

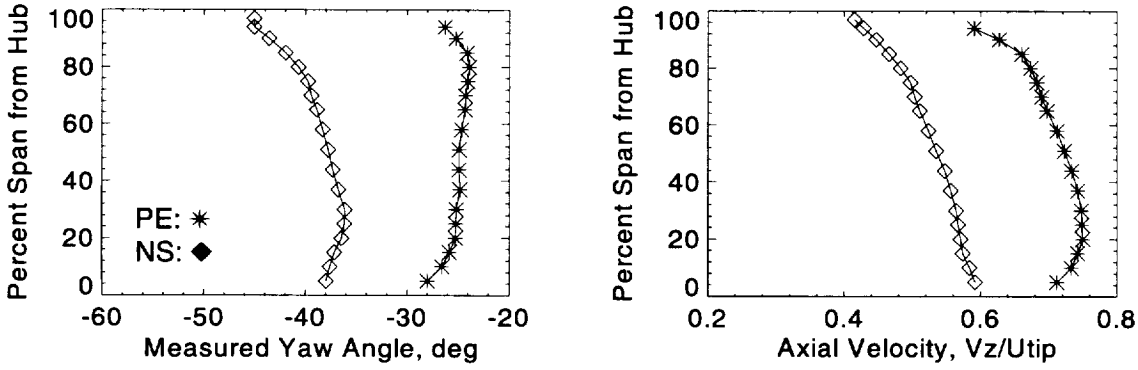

Figure 41. Radial distributions of downstream flow angle and axial velocity for the rotor only experiment.

A.2 Stage Data

The overall stage performance is given in Table 8.

Table 8: Aero performance for stage configuration.

	Mass Flow, kg/s	PR	TR	Efficiency, %
PE	17.2	1.40	1.11	88.5
NS	15.1	1.49	1.15	80.8

The radial profiles of total pressure ratio, total temperature ratio, static pressure, and efficiency are shown in Figure 42 for the PE and NS case. The radial profiles of axial velocity and flow angle are shown in Figure 43 for the PE and NS cases. These profiles are from data which is averaged in the circumferential direction.

Crosschannel plots of total pressure and total temperature are shown in Figures 44 and 45 for the PE and NS cases. The suction side of the stator wake is on the left side of the wake.

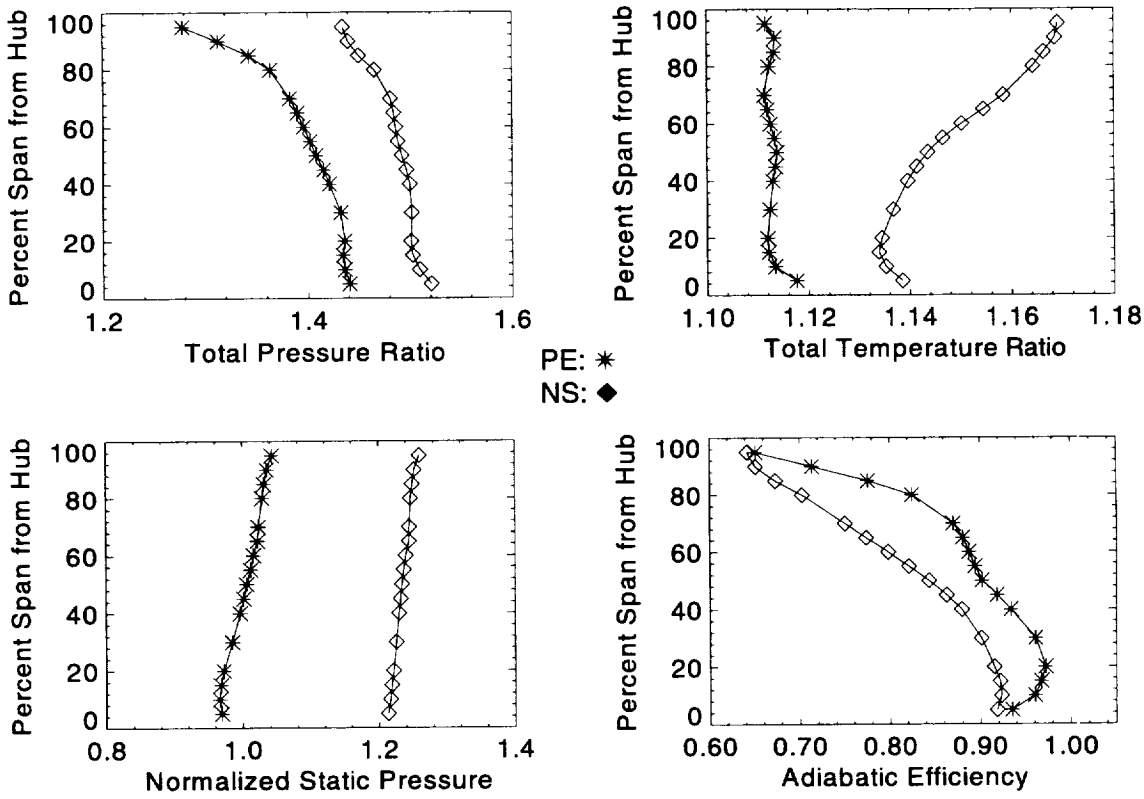

Figure 42. Radial distribution of performance parameters for the stage experiment.

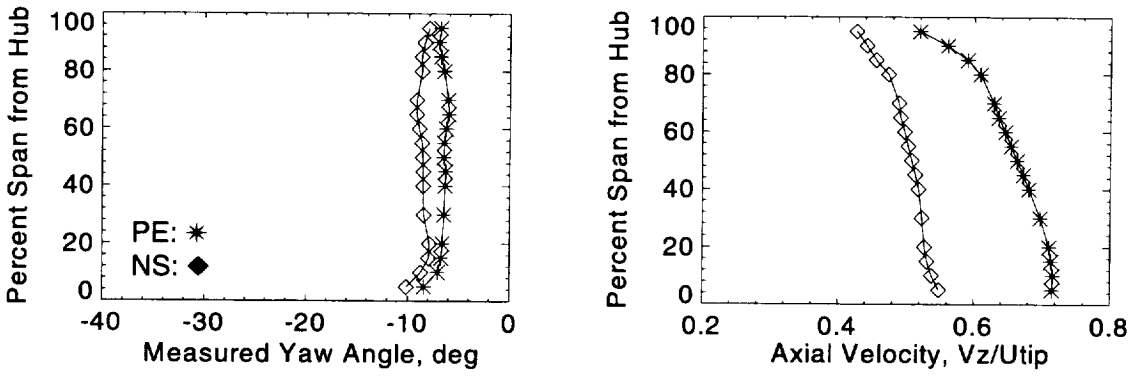

Figure 43. Radial distributions of exit flow angle and axial velocity for the stage experiment.

Notice the stator tip clearance flow in the upper suction surface/casing corner of the pressure ratio plots.

A.3 Stator Flow Field Periodicity

The conventional stators (aero stators) are mounted from the casing while the four stator blades under the optical access window (laser stators) are mounted from the hub while the aero stators have clearance at both hub and casing. The laser stators have clearance only at the casing. Additionally, the profile of the laser stators is thicker at the hub for mechanical reasons. Four guard blades with the laser stator profile which are casing-mounted were installed adjacent to the laser stators, two on either side, resulting in a group of eight stator blades having a thickened hub profile. The guard blade had both hub and casing clearance. Because of these differences, there was concern about changes in the rotor flow field due to the different back pressure caused by the non-similar leakage configurations of the two types of stator blade.

A survey of total pressure and total temperature was done for 2.5 stator pitches at midspan downstream of the laser stators. In this initial survey, the freestream total pressure did not show acceptable periodicity (greater than 5.0% variance). The hub clearance of the guard blades was therefore sealed so that they more closely resembled the leakage configuration of the laser stators. The aero survey was repeated and the results are shown in Figure 46.

The flow field periodicity is much improved from the initial configuration but still shows some variance in free stream total pressure. This could be due to stator passage geometry dif-

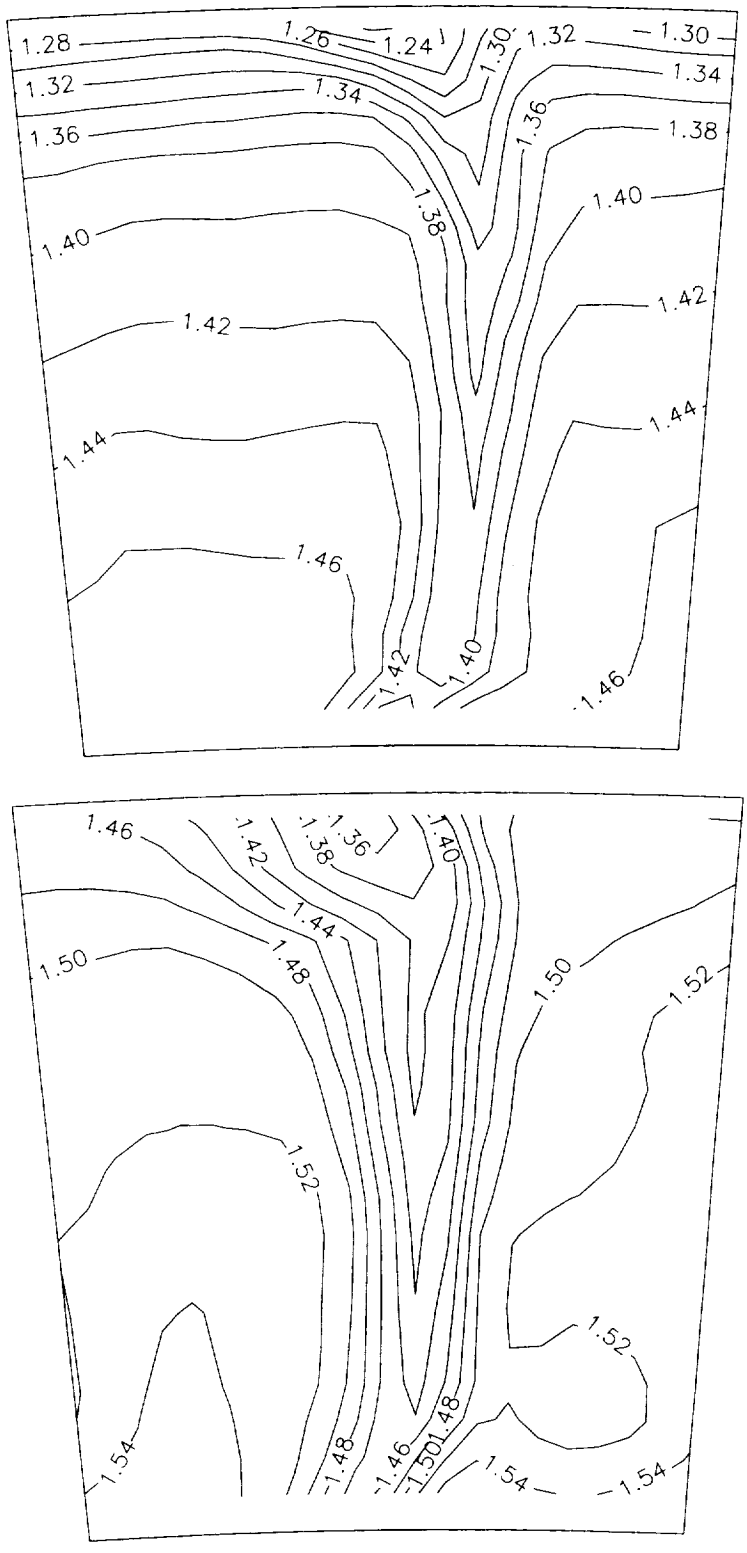

Figure 44. Crosschannel contours of pressure ratio at the downstream measurement plane for the stage experiment.

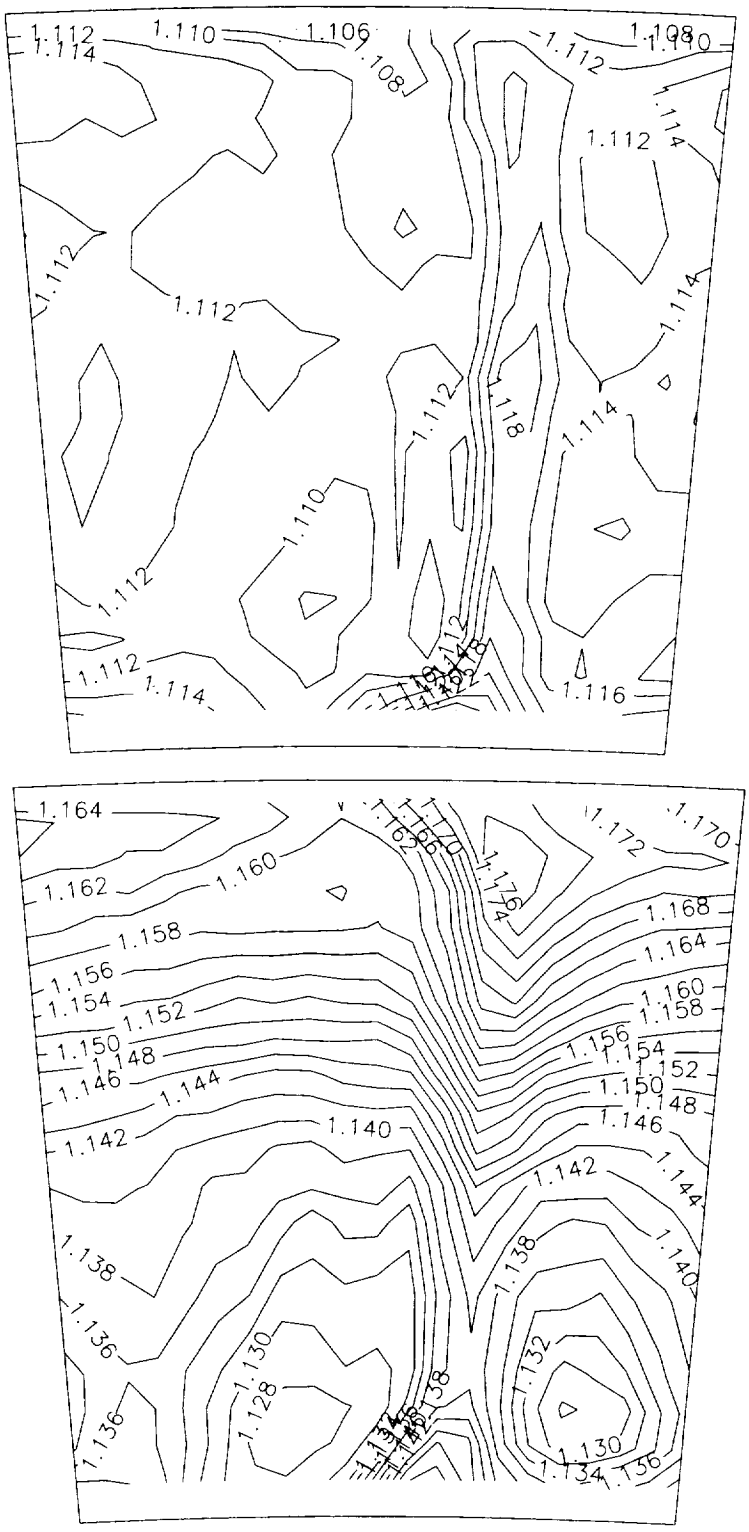

Figure 45. Crosschannel contours of total temperature ratio at the downstream measurement plane.

ferences or different rotor work output. The passage in which the LFA measurements were acquired shows good periodicity in term of total pressure. A geometrically different passage adjacent is not likely to affect the rotor wake decay in the measurement passage. However, if the total pressure difference is due to differing rotor work output, changes in the rotor wake with circumferential position observed with the laser anemometer system could be due to the rotor flow field adjusting to the new back pressure. Total temperature measurements indicate that only a portion (0.18 psia) of the total pressure change is due to rotor work output which is equivalent to a 0.15 kg/s change (7% of range) in mass flow as determined from the rotor operating characteristic. Much larger changes in operating point would be required to significantly affect the rotor wake velocity profiles for this rotor. Thus the flow field periodicity is considered adequate for this experiment.

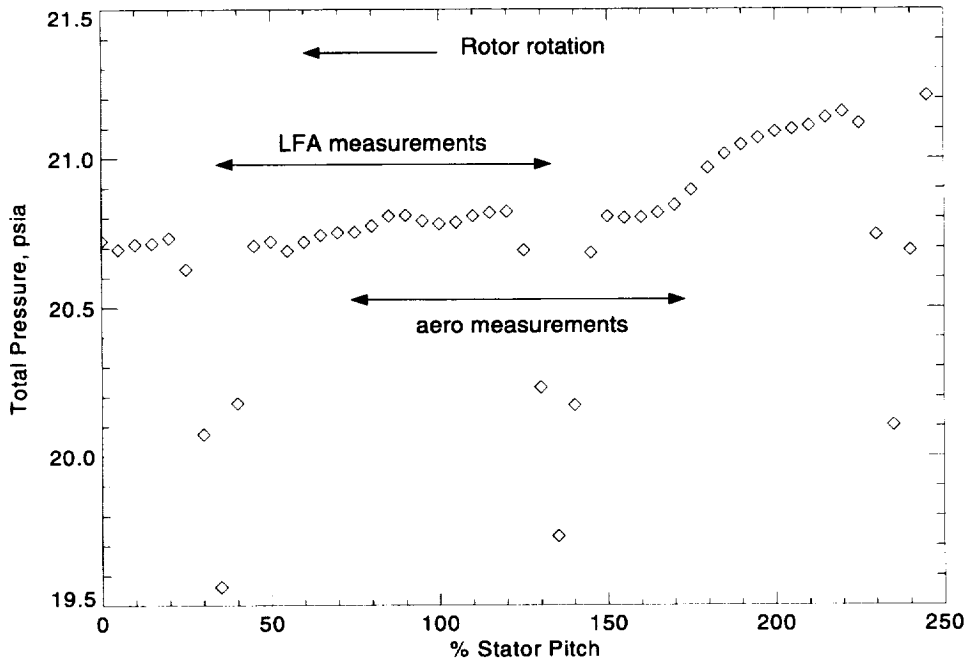

Figure 46. Stator flow field periodicity and location of LFA and aero performance measurements.

APPENDIX B: DETAILED LASER ANEMOMETER DATA

An analysis of wake profile measurement uncertainties based on the LFA reference measuremtns is presented. Next contour plots of relative velocity magnitude for the 75% span streamsurface laser anemometer data for the PE and NS cases are presented. The data is presented for fourteen time intervals of a rotor blade passing period. This is roughly the same time increment as for the simulation data shown in the following appendix.

The relative velocity magnitude is calculated as:

$$V_{relative} = \sqrt{(V_{axial}^2 + (V_{tangential} - V_{blade})^2)} \qquad \text{(EQ 1)}$$

The rotor blades shown in the figures illustrate the approximate rotor position relative to the stator. Some data in low gradient regions of the flow field were interpolated from neighboring points. The interpolation was linear and the wake profiles were shifted appropriately for the circumferential measurement position. The interpolation was done to give 25 data points across the stator pitch at all axial locations. The interpolated data was used for presentation purposes only and were not used for the wake decay calculations.

The final sections present measurements from the stator wakes and rotor wake profiles for the rotor in isolation measurements.

B.1 Wake Profile Uncertainty

As was stated in an earlier chapter the uncertainty associated with an individual LFA measurement is +/- 1.0 m/s in velocity and +/- 0.5 degrees in flow angle. Multiple LFA measurements are acquired for each window. These measurements are averaged for each window and then ensemble averaged to an average passage respresentation. A standard deviation value for each window is stored along with the average velocity profiles. Figure shows a wake profile from the stator leading edge plane and the associated standard deviation. The standard deviation shows the confidence of the velocity average for a particular window and is relatively large due to velocity variations from random unsteadiness, wake phase shifts, and passage-to-

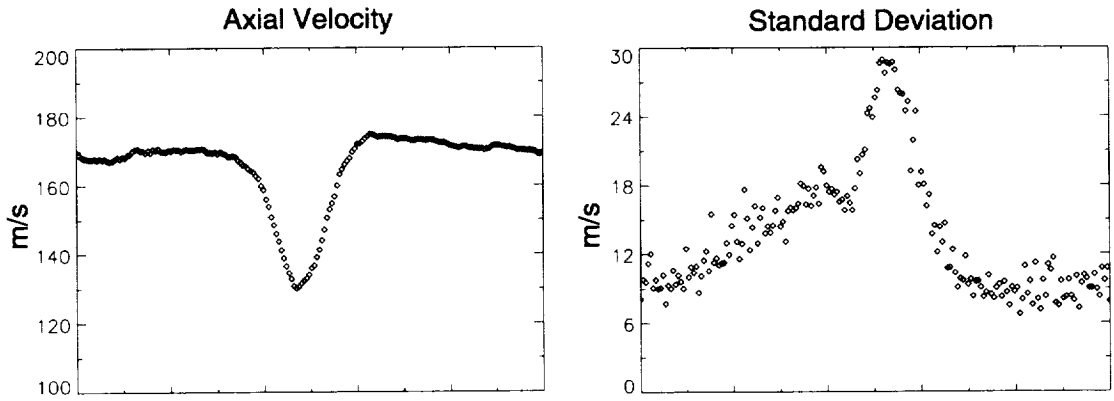

Figure 47. Axial velocity profile and standard deviation for a near stall rotor wake at the stator leading edge plane.

passage wake profile differences. The standard deviation is higher in the wake regions of the flow field due to all of the previously mentioned effects. These levels of standard deviation are typical of measurements inside of multi bladerow compressors where the freestream turbulence intensity is typically above 5% and turbulence intensity in the wake is greater than 10%.

A more relevant question to ask is "How much do the wake profiles change from day to day?" since this directly impacts the deterministic kinetic energy calculations. This question can be answered using the daily wake reference measurements which were acquired for both the PE and NS operating conditions. Only the reference measuremetns which were taken on the days for which the data was processed are shown; five for the PE data and two for the NS data. Figure part a. shows all of the reference measurements overplotted. The average and standard deviation of the wake profiles was calculated and is shown in part b. of the figure for the PE data. The mean is shown by symbols and +/- 1.0 standard deviation as solid lines. Since only two NS profiles exist, the standard deviation could not be calculated. The accuracy of the free stream velocity for the PE data is +/- 5.0 m/s which is +/- 1.0 standard deviation from the mean. The accuracy of the free stream velocity for the NS data is estimated from the scatter in part a. of the figure to be +/- 2.5 m/s. The larger uncertainty in the PE data is because the data was acquired over a longer time period than the NS data.

To determine the change in the wake profile from day to day the mean velocity was subtracted from each profile and the zero mean profiles overplotted in part c. of the figure. Part d. of the figure shows the mean and +/- 1.0 standard deviation. All of the wake profiles show

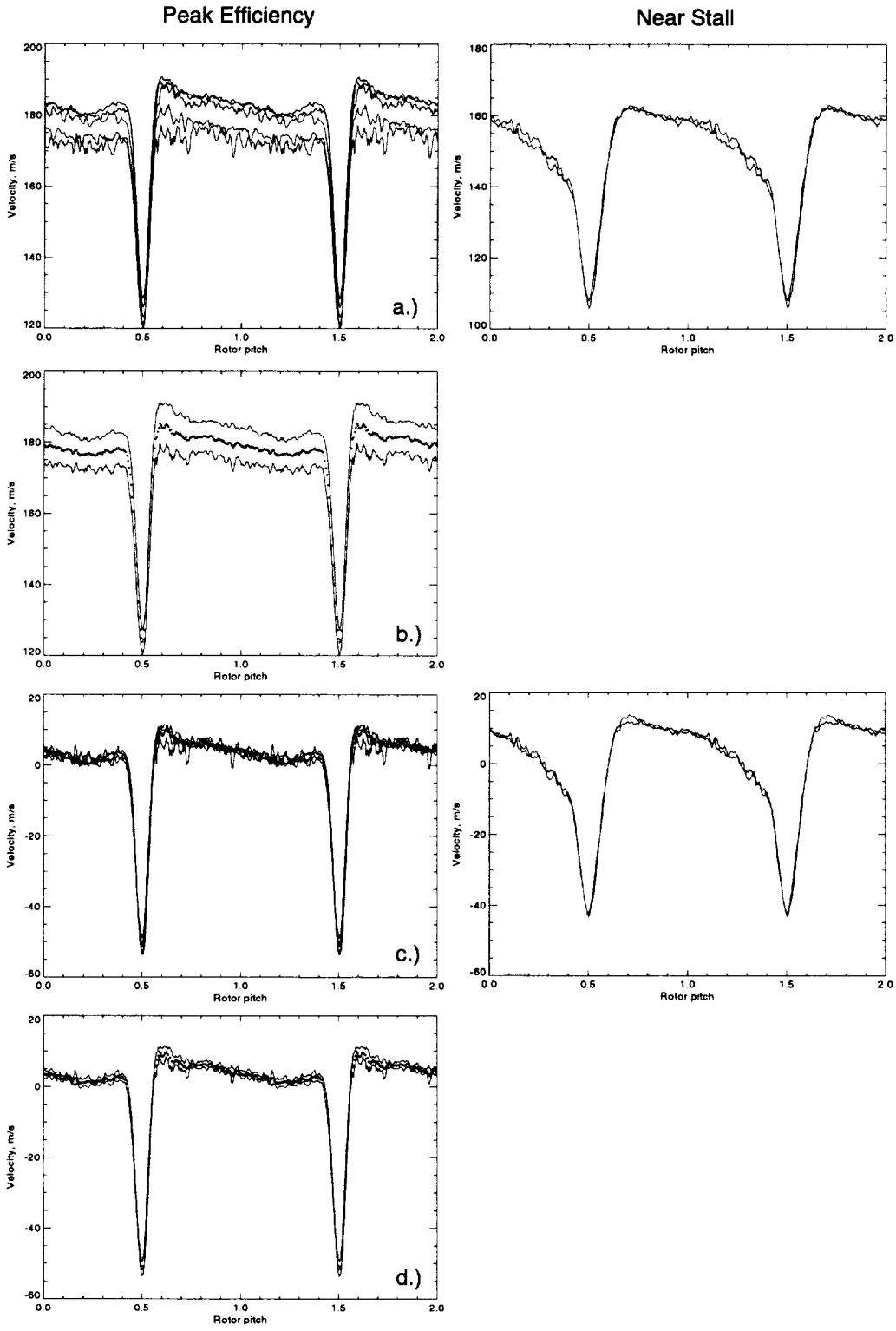

Figure 48. Daily reference measurements: a.) raw traces b.) average and standard deviation of raw traces c.) zero mean traces d.) mean and standard deviation of zero mean traces.

very good agreement from day to day in both their width and depth.

These day to day changes lead to an uncertainty in the unsteady kinetic energy calculations of +/- 0.01 for the PE data and +/- 0.005 for the NS data in units of % Utip^3.

B.2 Peak Efficiency Data

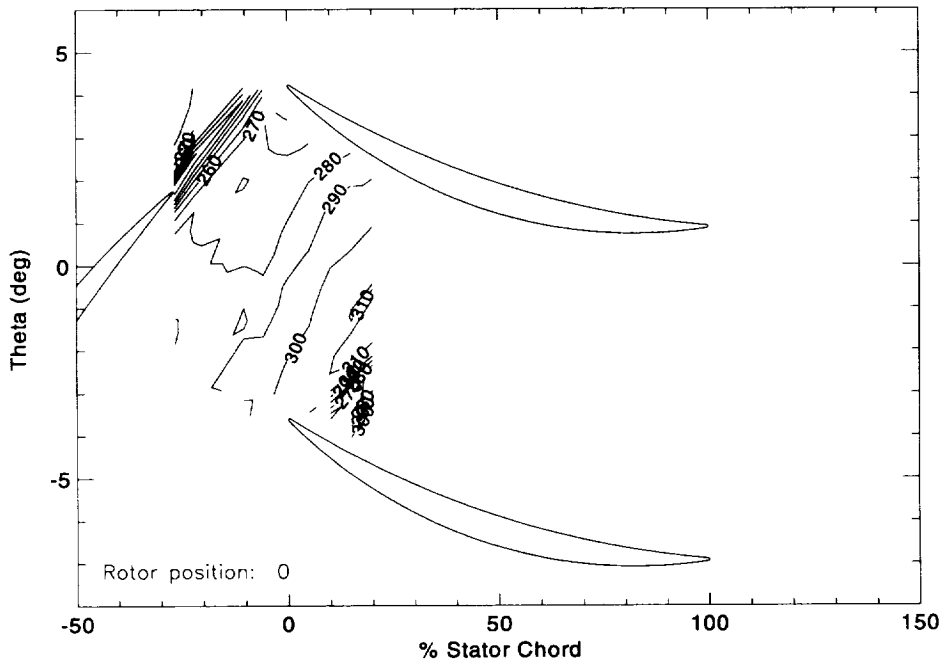

Figure 49. Relative velocity magnitude (m/s) for rotor position 1 of 15 for peak efficiency laser anemometer data.

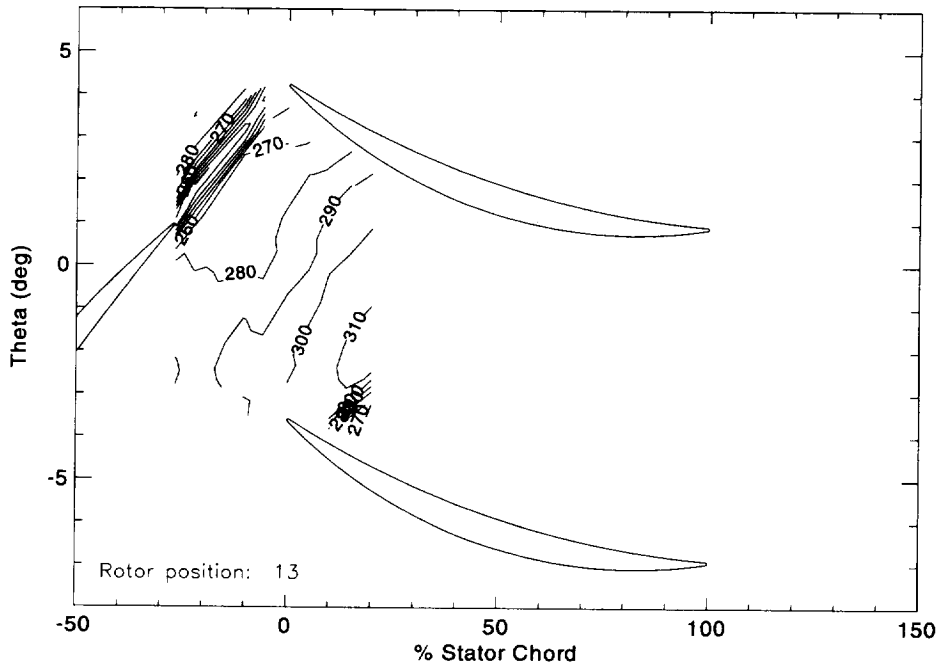

Figure 50. Relative velocity magnitude (m/s) for rotor position 2 of 15 for peak efficiency laser anemometer data.

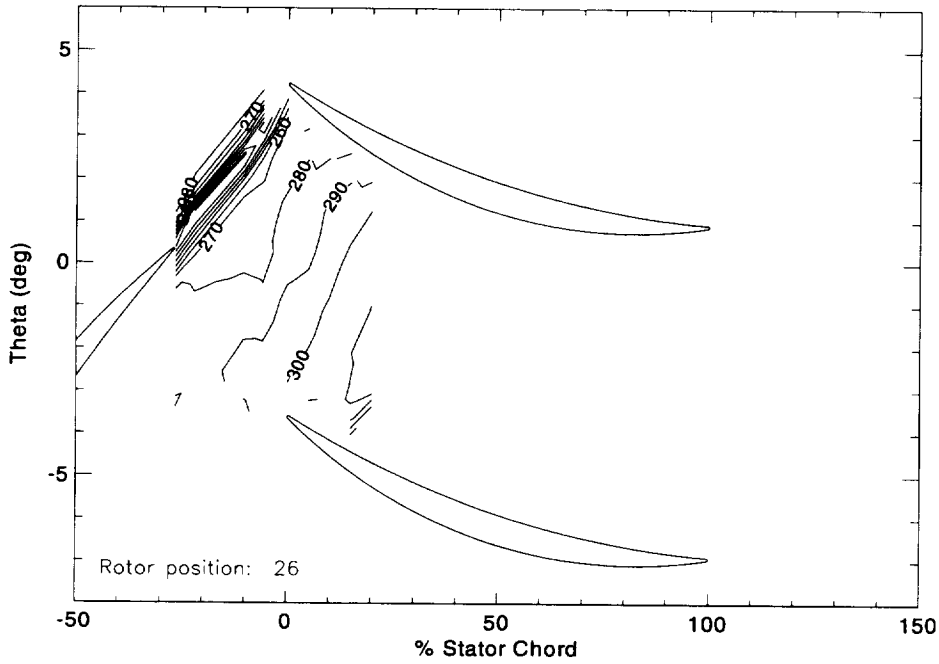

Figure 51. Relative velocity magnitude (m/s) for rotor position 3 of 15 for peak efficiency laser anemometer data.

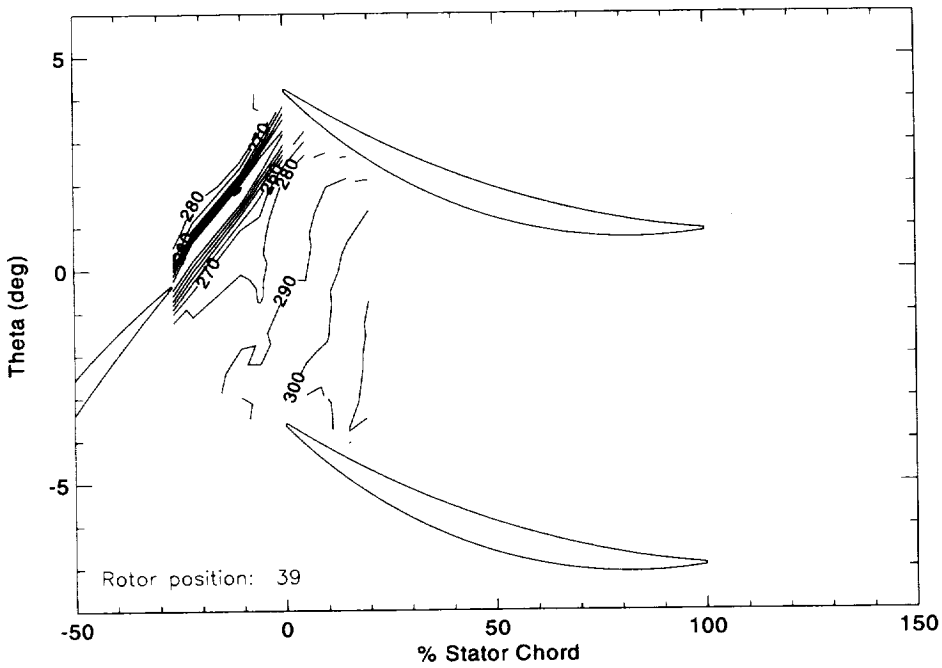

Figure 52. Relative velocity magnitude (m/s) for rotor position 4 of 15 for peak efficiency laser anemometer data

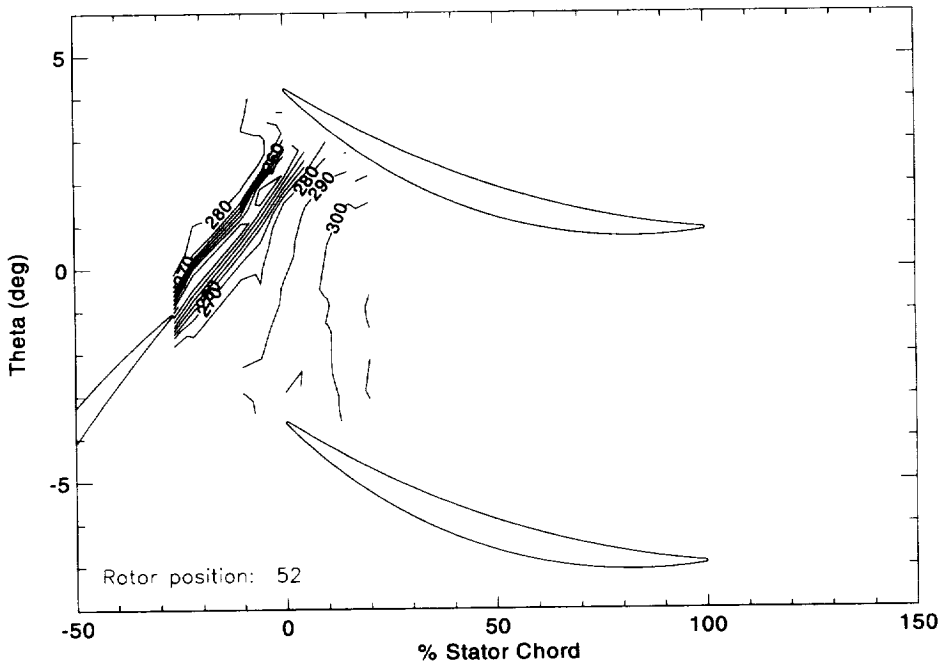

Figure 53. Relative velocity magnitude (m/s) for rotor position 5 of 15 for peak efficiency laser anemometer data.

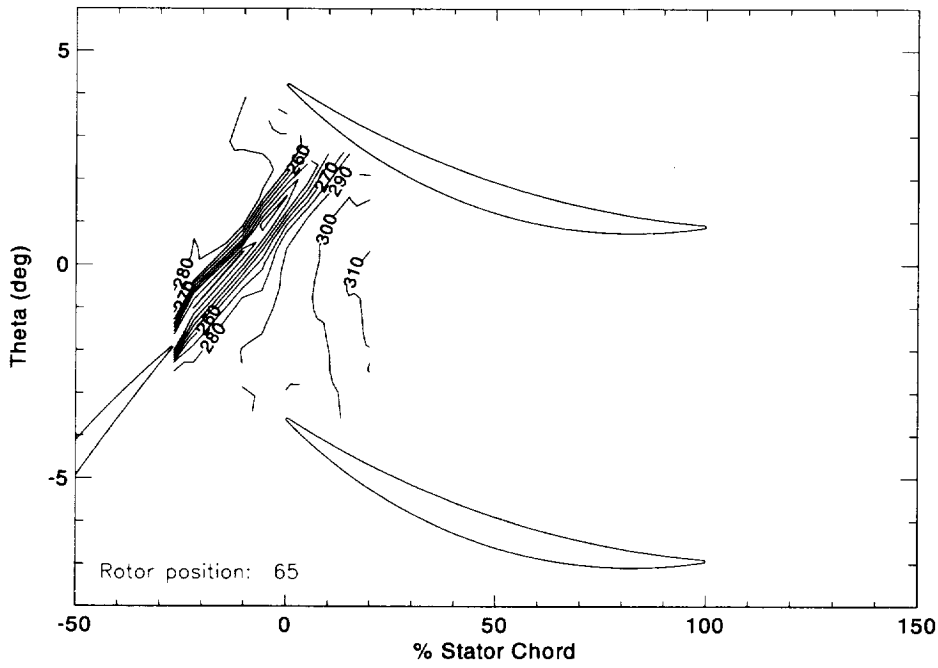

Figure 54. Relative velocity magnitude (m/s) for rotor position 6 of 15 for peak efficiency laser anemometer data.

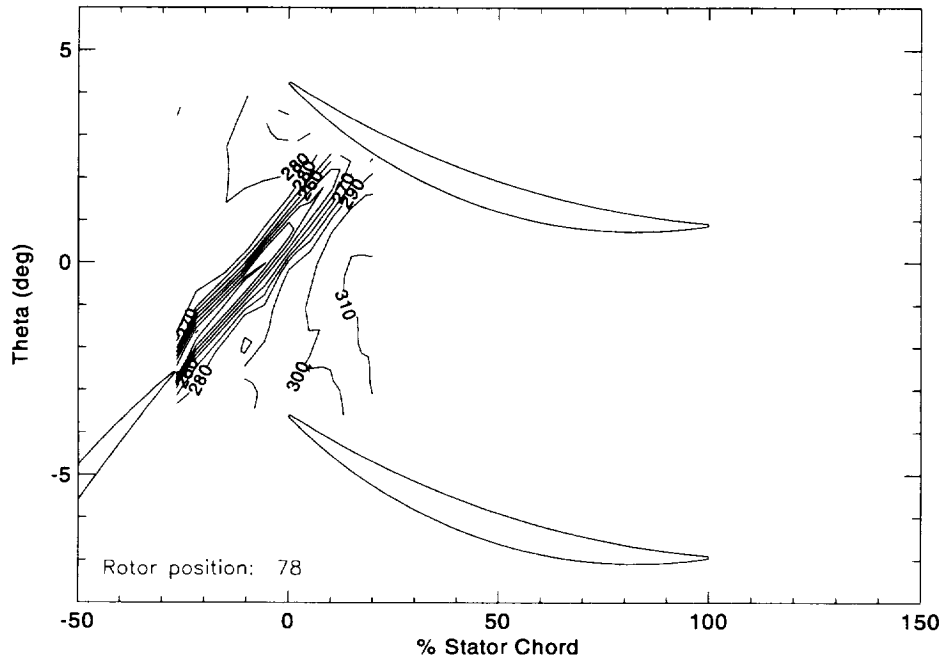

Figure 55. Relative velocity magnitude (m/s) for rotor position 7 of 15 for peak efficiency laser anemometer data.

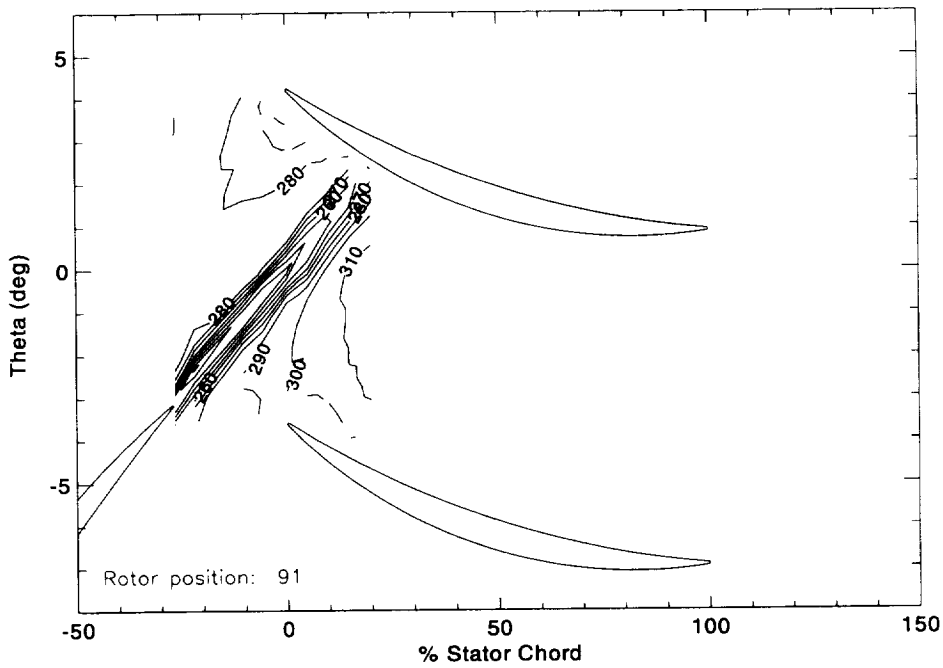

Figure 56. Relative velocity magnitude (m/s) for rotor position 8 of 15 for peak efficiency laser anemometer data.

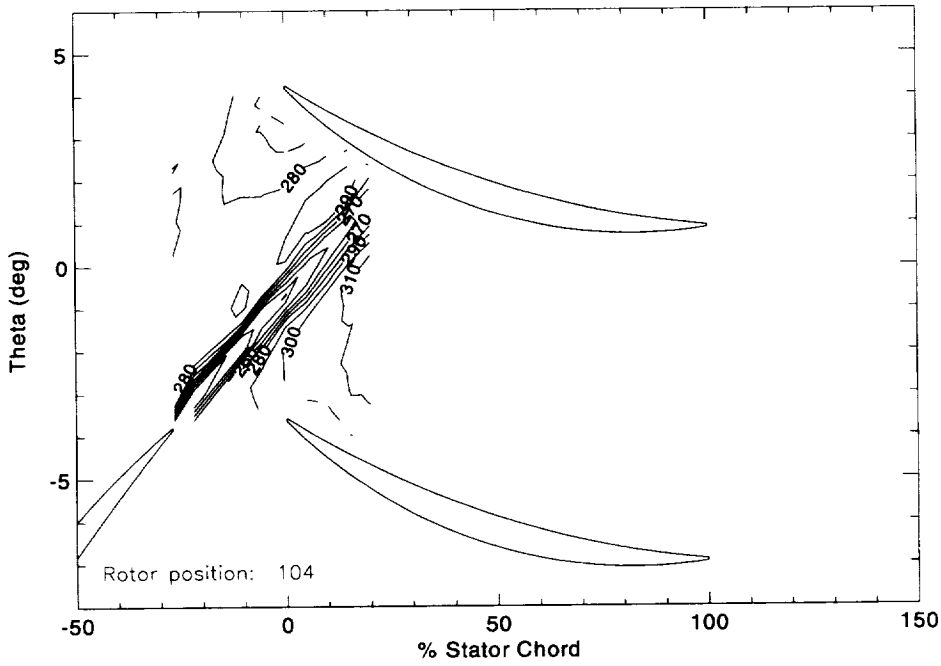

Figure 57. Relative velocity magnitude (m/s) for rotor position 9 of 15 for peak efficiency laser anemometer data.

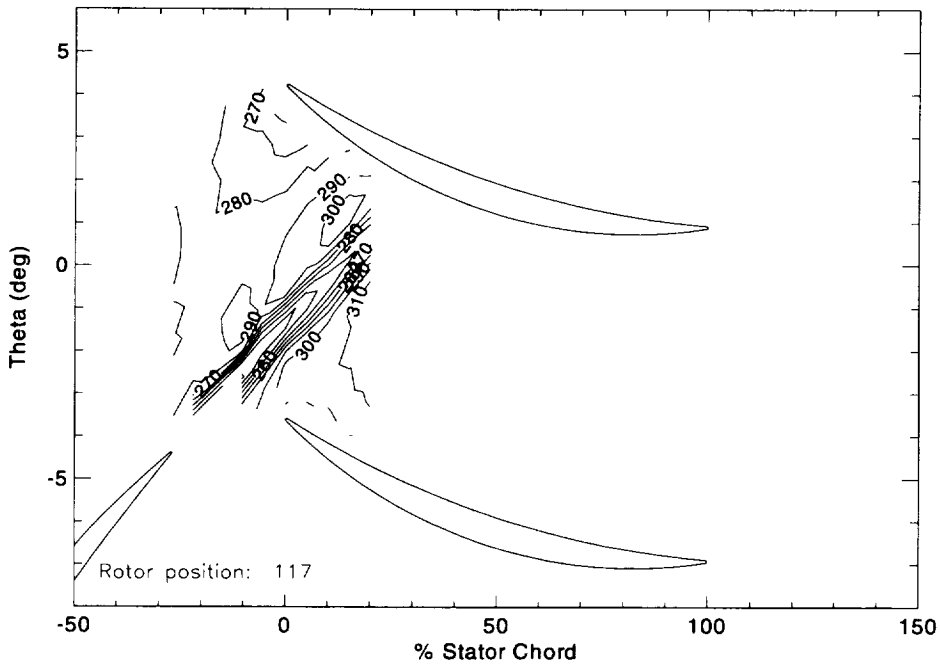

Figure 58. Relative velocity magnitude (m/s) for rotor position 10 of 15 for peak efficiency laser anemometer data.

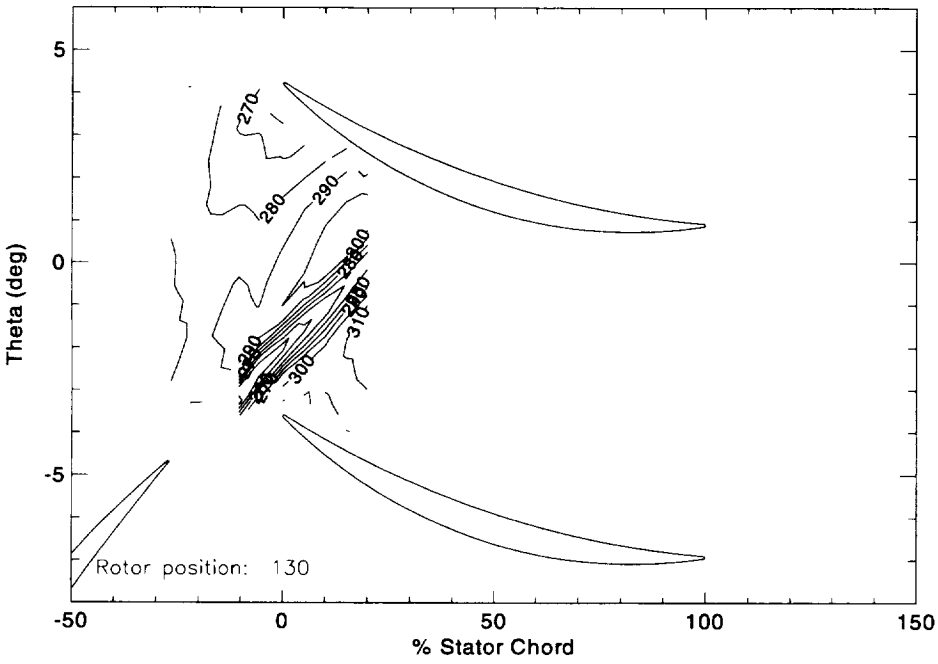

Figure 59. Relative velocity magnitude (m/s) for rotor position 11 of 15 for peak efficiency laser anemometer data.

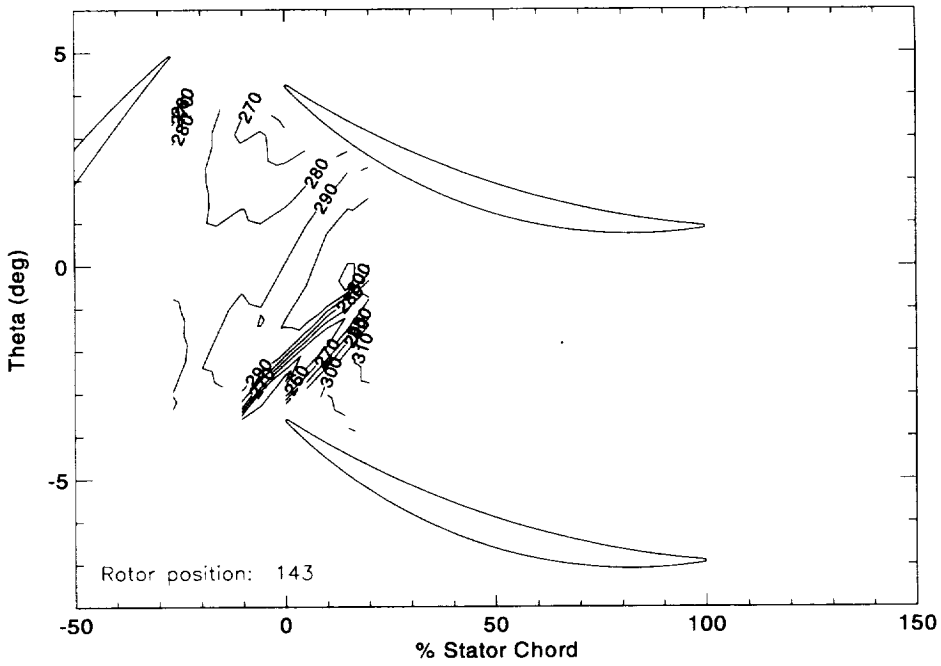

Figure 60. Relative velocity magnitude (m/s) for rotor position 12 of 15 for peak efficiency laser anemometer data.

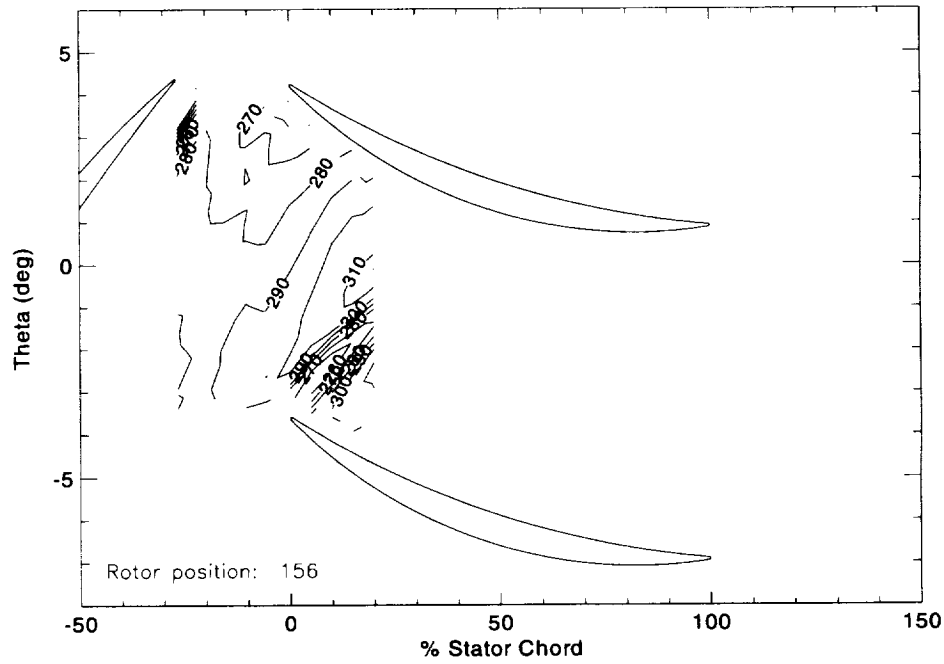

Figure 61. Relative velocity magnitude (m/s) for rotor position 13 of 15 for peak efficiency laser anemometer data.

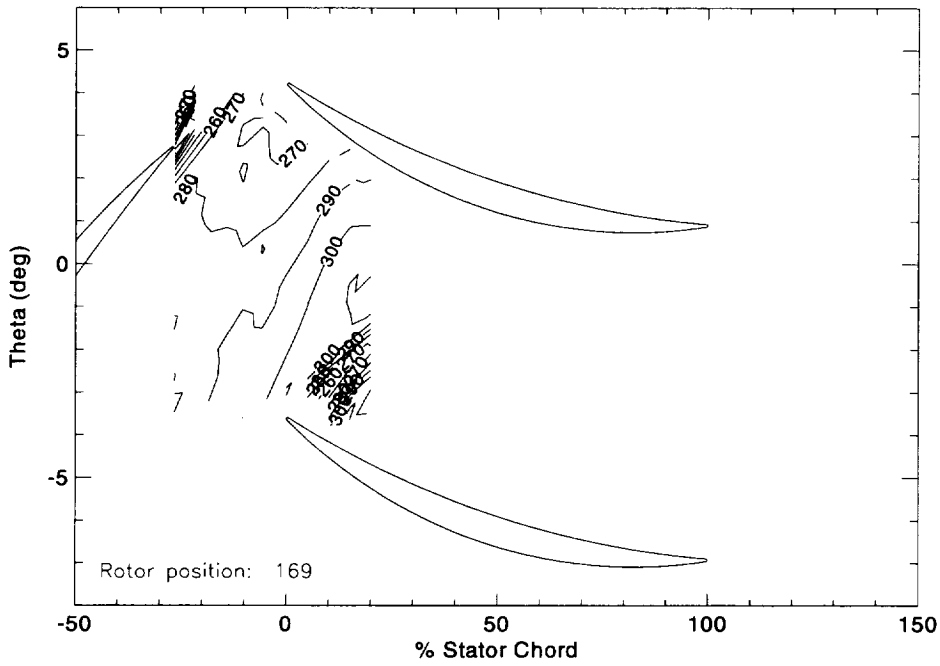

Figure 62. Relative velocity magnitude (m/s) for rotor position 14 of 15 for peak efficiency laser anemometer data.

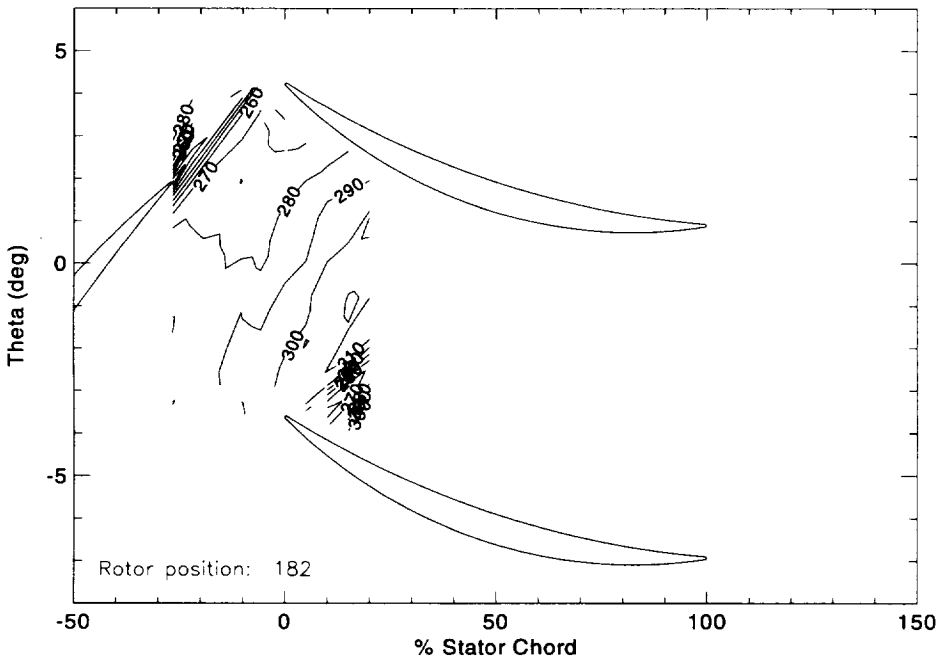

Figure 63. Relative velocity magnitude (m/s) for rotor position 15 of 15 for peak efficiency laser anemometer data.

B.3 Near Stall Data

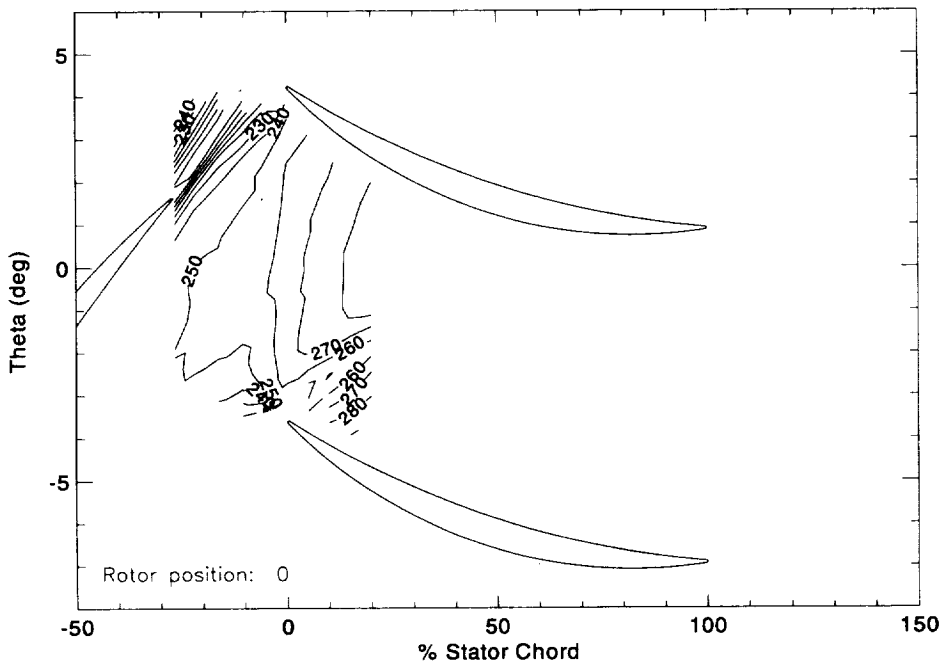

Figure 64. Relative velocity magnitude (m/s) for rotor position 1 of 15 for near stall laser anemometer data.

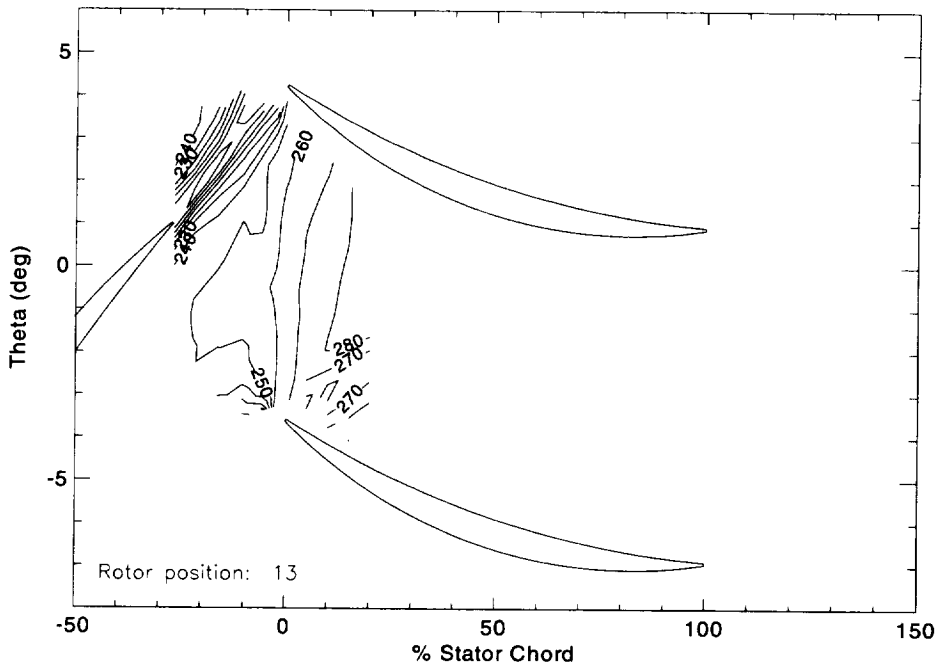

Figure 65. Relative velocity magnitude (m/s) for rotor position 2 of 15 for near stall laser anemometer data.

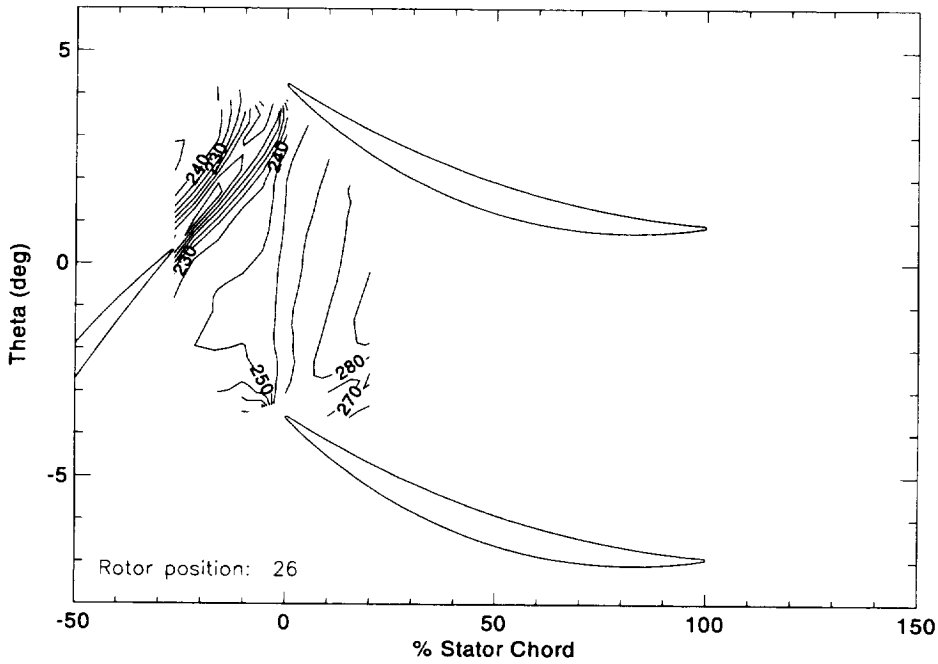

Figure 66. Relative velocity magnitude (m/s) for rotor position 3 of 15 for near stall laser anemometer data.

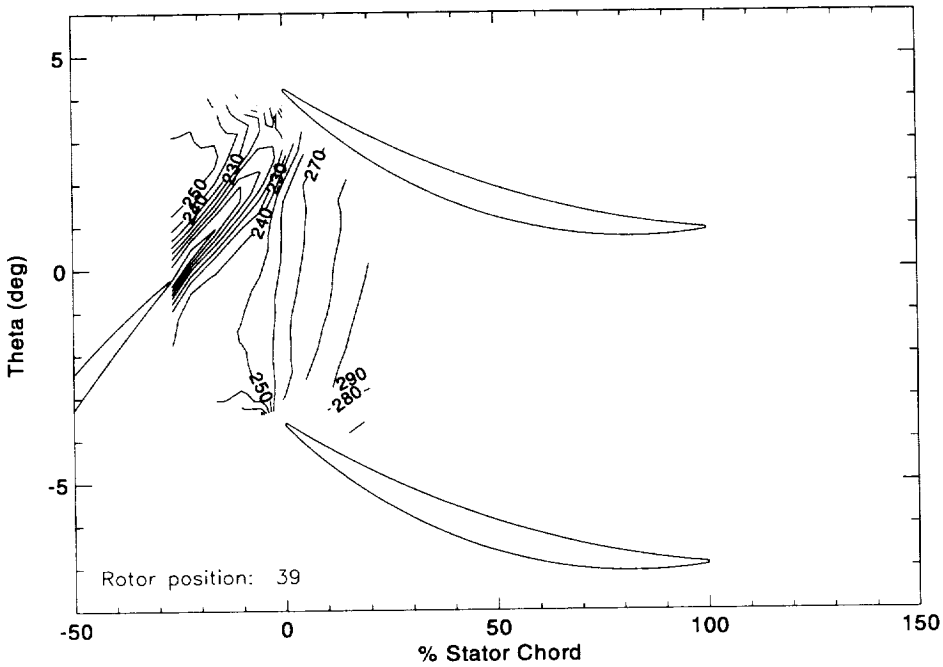

Figure 67. Relative velocity magnitude (m/s) for rotor position 4 of 15 for near stall laser anemometer data.

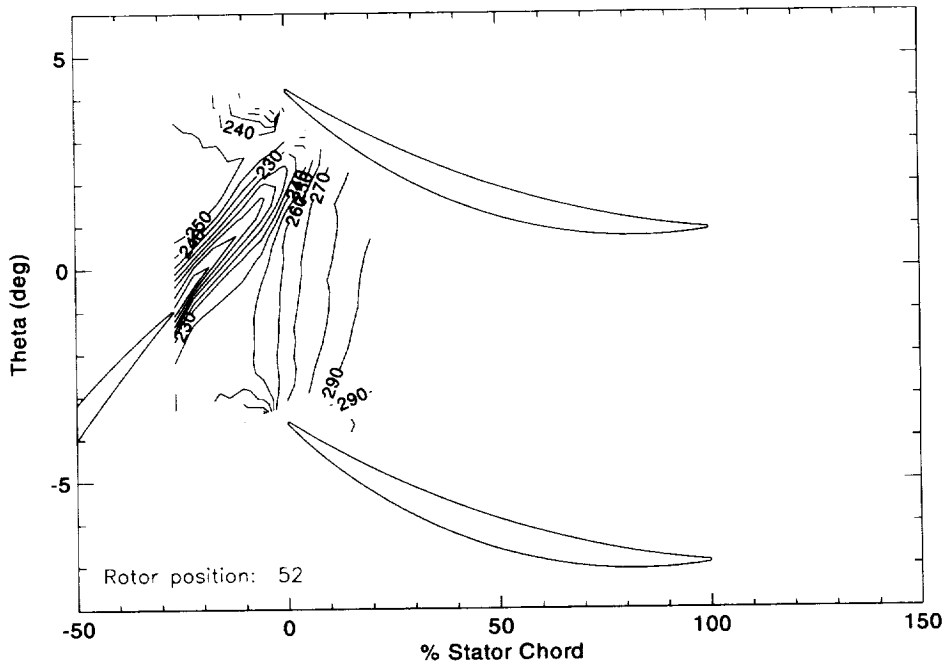

Figure 68. Relative velocity magnitude (m/s) for rotor position 5 of 15 for near stall laser anemometer data.

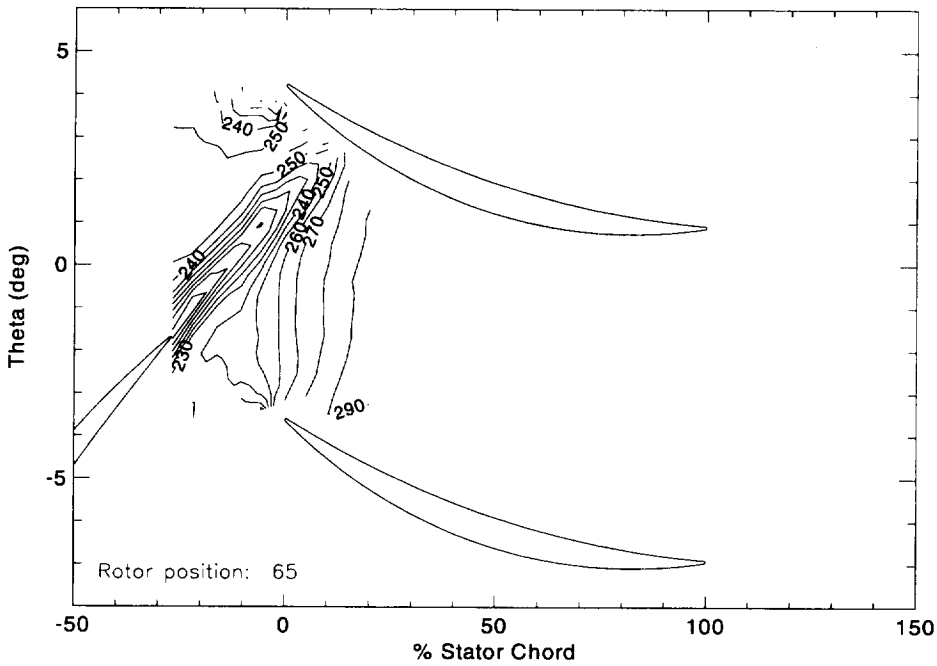

Figure 69. Relative velocity magnitude (m/s) for rotor position 6 of 15 for near stall laser anemometer data.

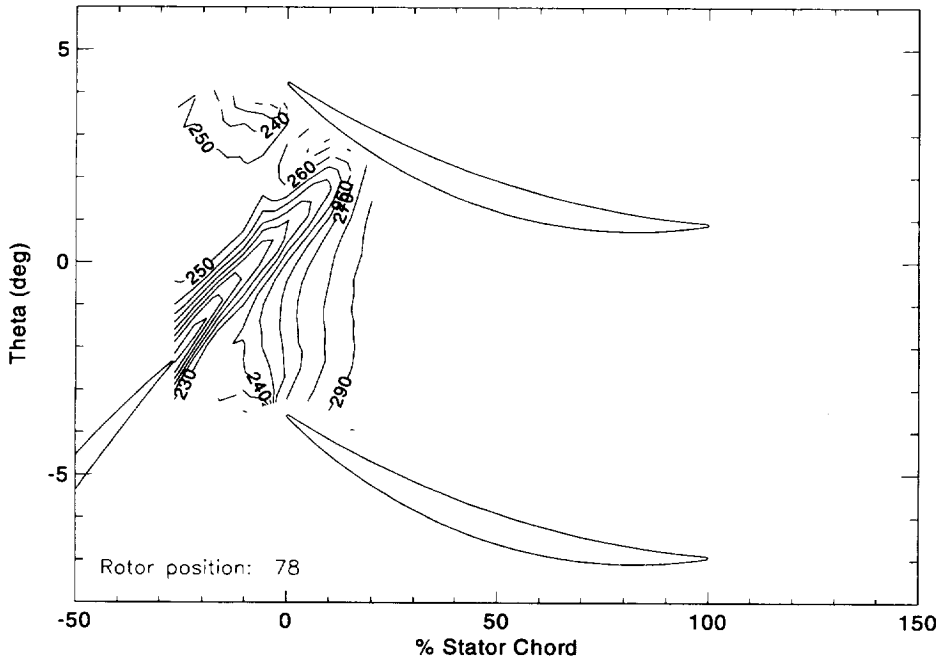

Figure 70. Relative velocity magnitude (m/s) for rotor position 7 of 15 for near stall laser anemometer data.

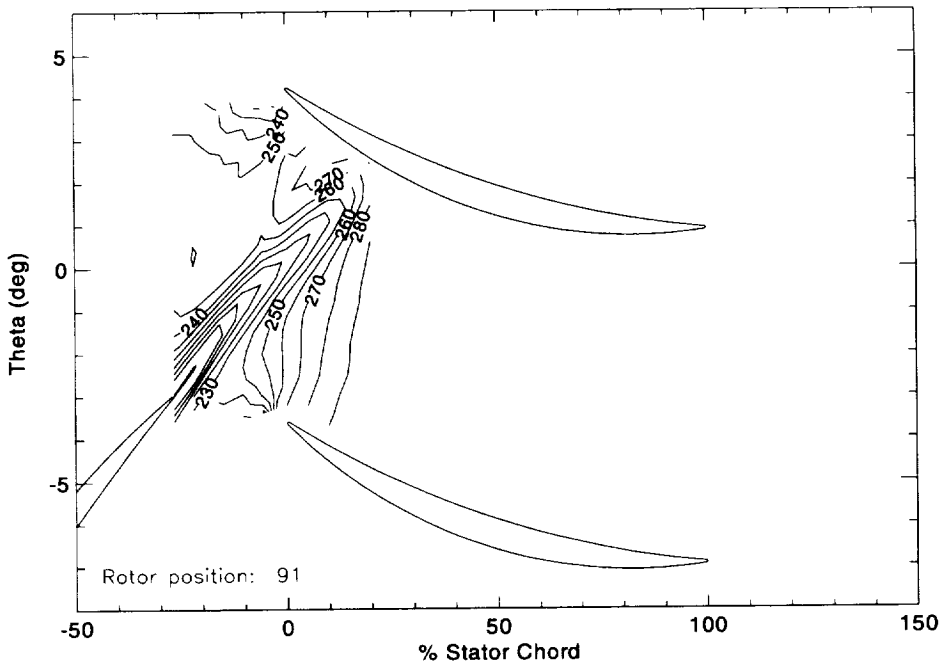

Figure 71. Relative velocity magnitude (m/s) for rotor position 8 of 15 for near stall laser anemometer data.

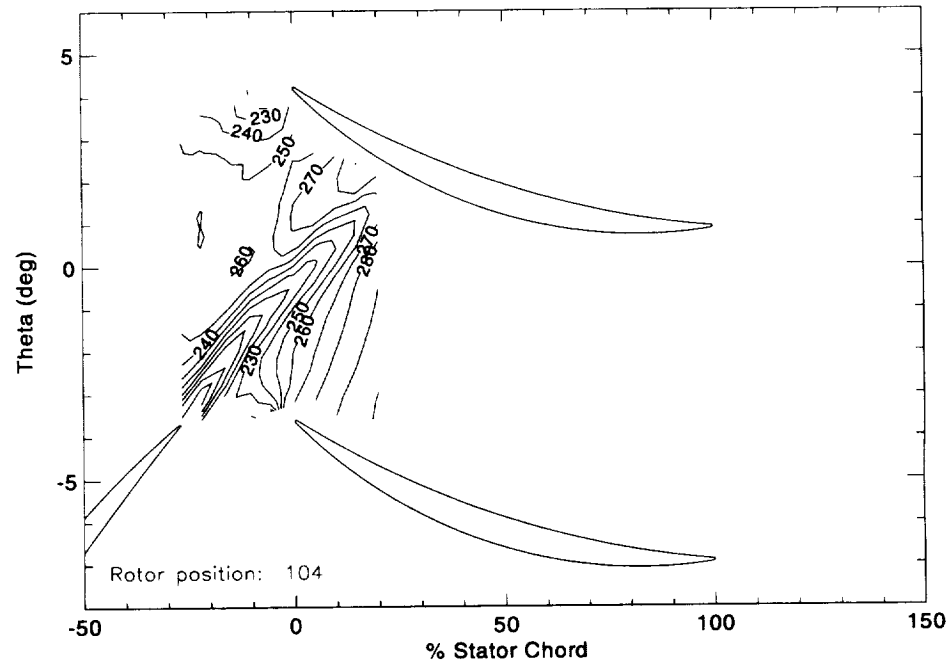

Figure 72. Relative velocity magnitude (m/s) for rotor position 9 of 15 for near stall laser anemometer data.

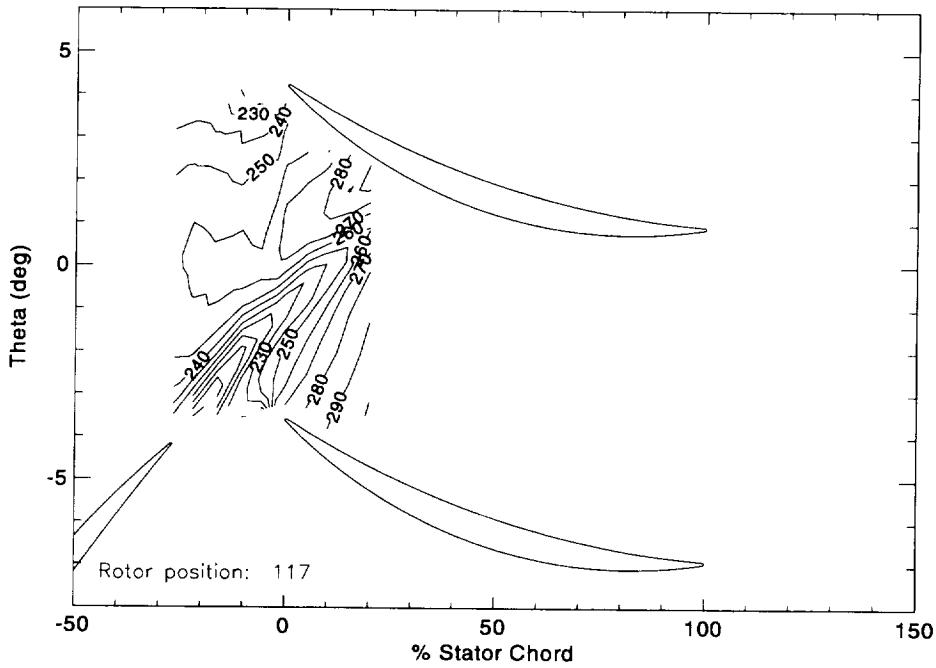

Figure 73. Relative velocity magnitude (m/s) for rotor position 10 of 15 for near stall laser anemometer data.

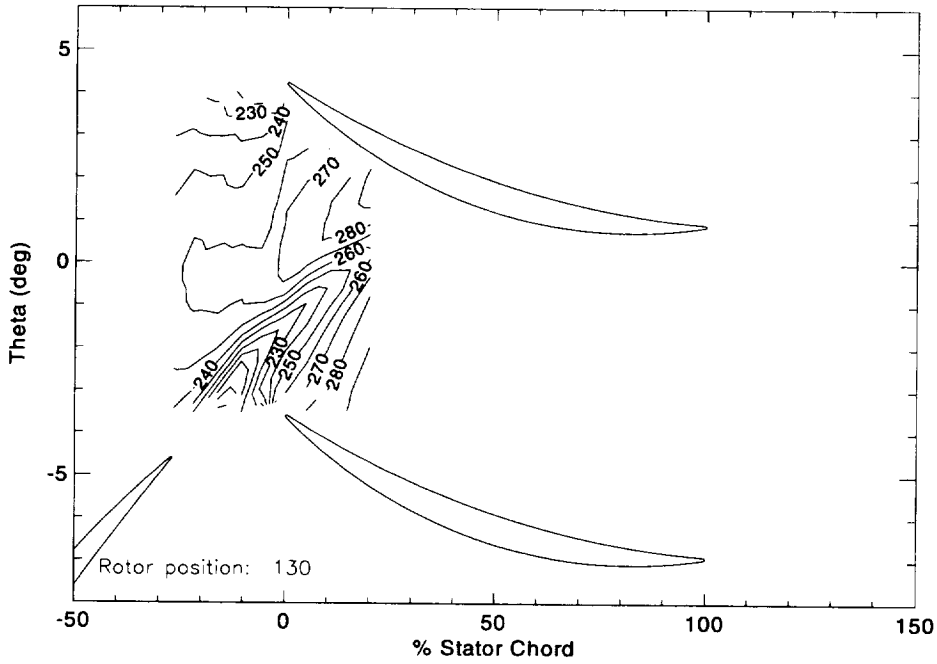

Figure 74. Relative velocity magnitude (m/s) for rotor position 11 of 15 for near stall laser anemometer data.

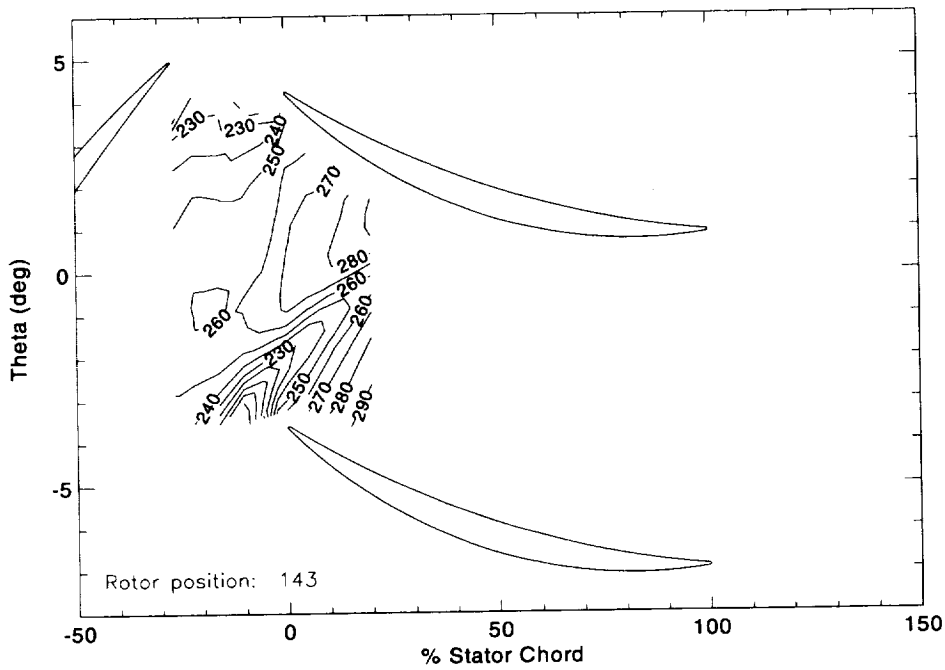

Figure 75. Relative velocity magnitude (m/s) for rotor position 12 of 15 for near stall laser anemometer data.

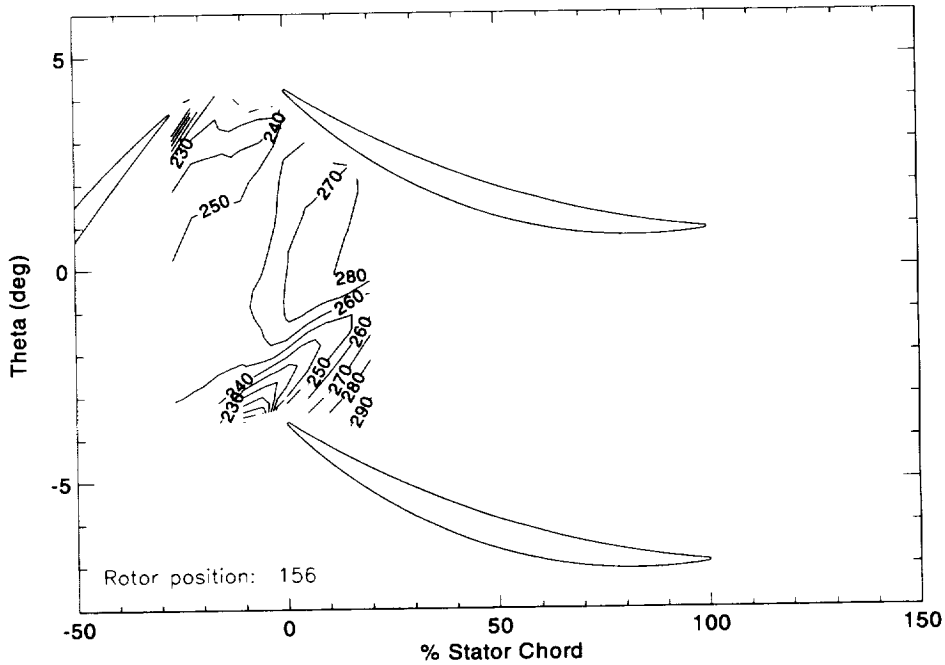

Figure 76. Relative velocity magnitude (m/s) for rotor position 13 of 15 for near stall laser anemometer data.

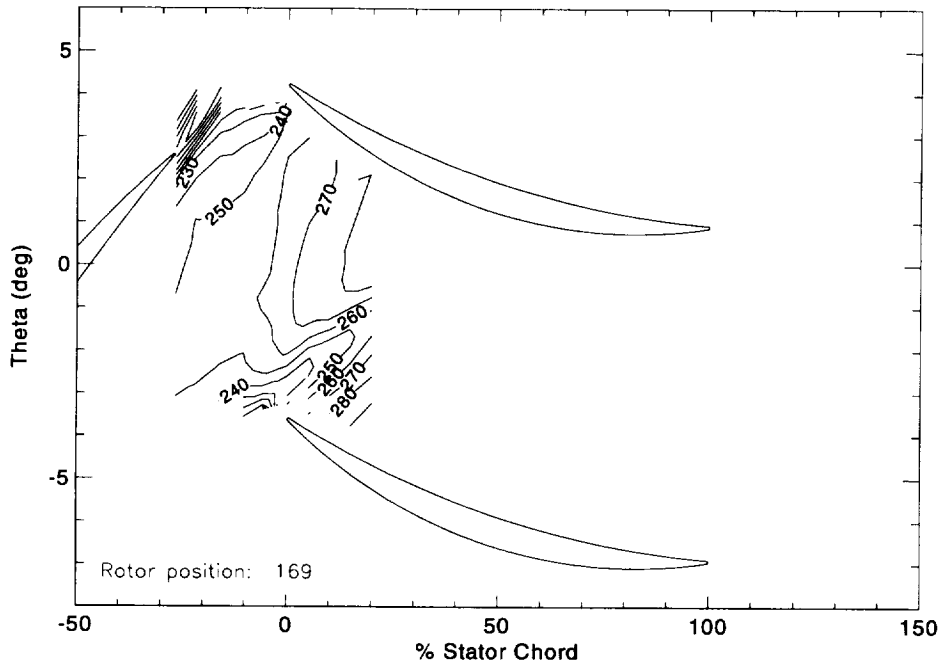

Figure 77. Relative velocity magnitude (m/s) for rotor position 14 of 15 for near stall laser anemometer data.

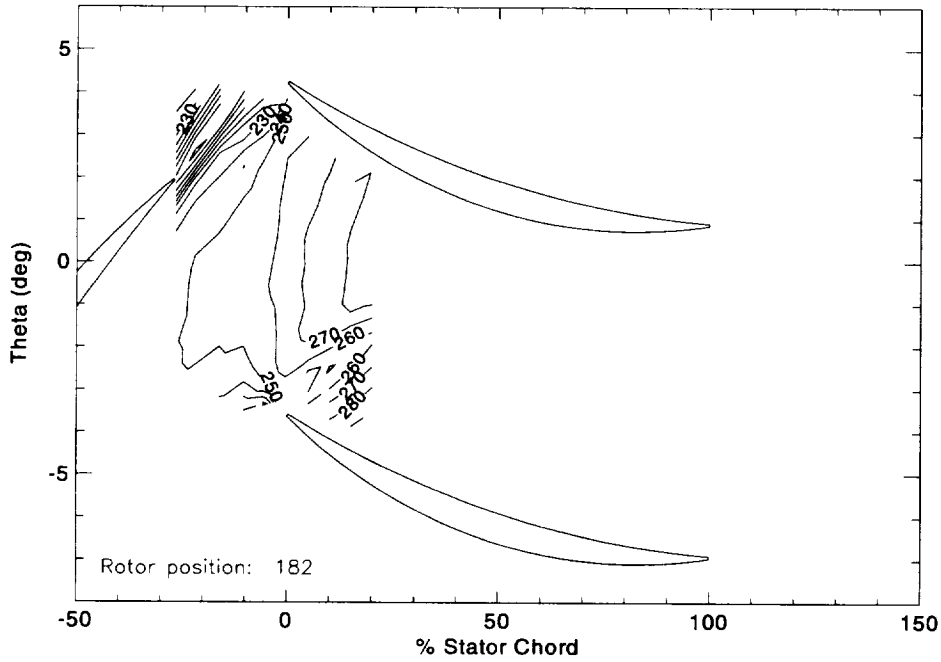

Figure 78. Relative velocity magnitude (m/s) for rotor position 15 of 15 for near stall laser anemometer data.

B.4 Stator Unsteady Kinetic Energy

The following sections consider the LFA data in more detail including presentation of data from additional regions of the flow field where interesting wake decay and/or unsteadiness was observed. This section shows an overview of the disturbance kinetic energy distribution in the entrance region of the stator flow field. The subsequent sections contain more detailed LFA wake profiles from other regions of the flow field.

Figure 79 shows the disturbance kinetic energy distribution in the stator passage for the PE and NS conditions. In general, the DKE decreases with axial position downstream of the rotor trailing edge. In the main body of the thesis the wake decay model was used to predict the wake decay through the midpitch location of the stator passage and results from the model were compared to the DKE at midpitch. Some other observations can be made from the DKE distribution shown in Figure 79. At the rotor trailing edge the DKE distribution is relatively uniform in the circumferential direction and a region of high DKE exists close to the suction surface stator leading edge for the NS case. Detailed wake velocity profiles of rotor wakes in the rotor/stator gap region are shown in the next section.

B.5 Wake Character in the Rotor/Stator Gap

Figures 80 and 81 show the rotor wake profiles at the trailing edge plane along an extension of the 4%, 50%, and 87% stator pitch line. Only small differences in the velocity profile shape are noticeable with changing circumferential position for both the PE and NS case. This is again circumstantial evidence that the stator row influence on the rotor is minimal. A full unsteady simulation to be completed in the future should help to more definitively clarify this.

Figures 82 and 83 show how the character of the rotor wake has changed by the time it reaches the stator leading edge plane. The velocity field of the wakes that approach the pressure surface and suction surface of the stator is very distorted and attenuated by the interaction with the stator stagnation point.

A region of high disturbance kinetic energy appears on the suction surface just downstream of the leading edge for the NS case. Figure 84 shows the wake velocity profiles for this position. The large velocity fluctuation appears to be caused by an unsteady separation induced by the high incidence flow of the wake passing over the leading edge. This observation was made with the help of the unsteady simulations.

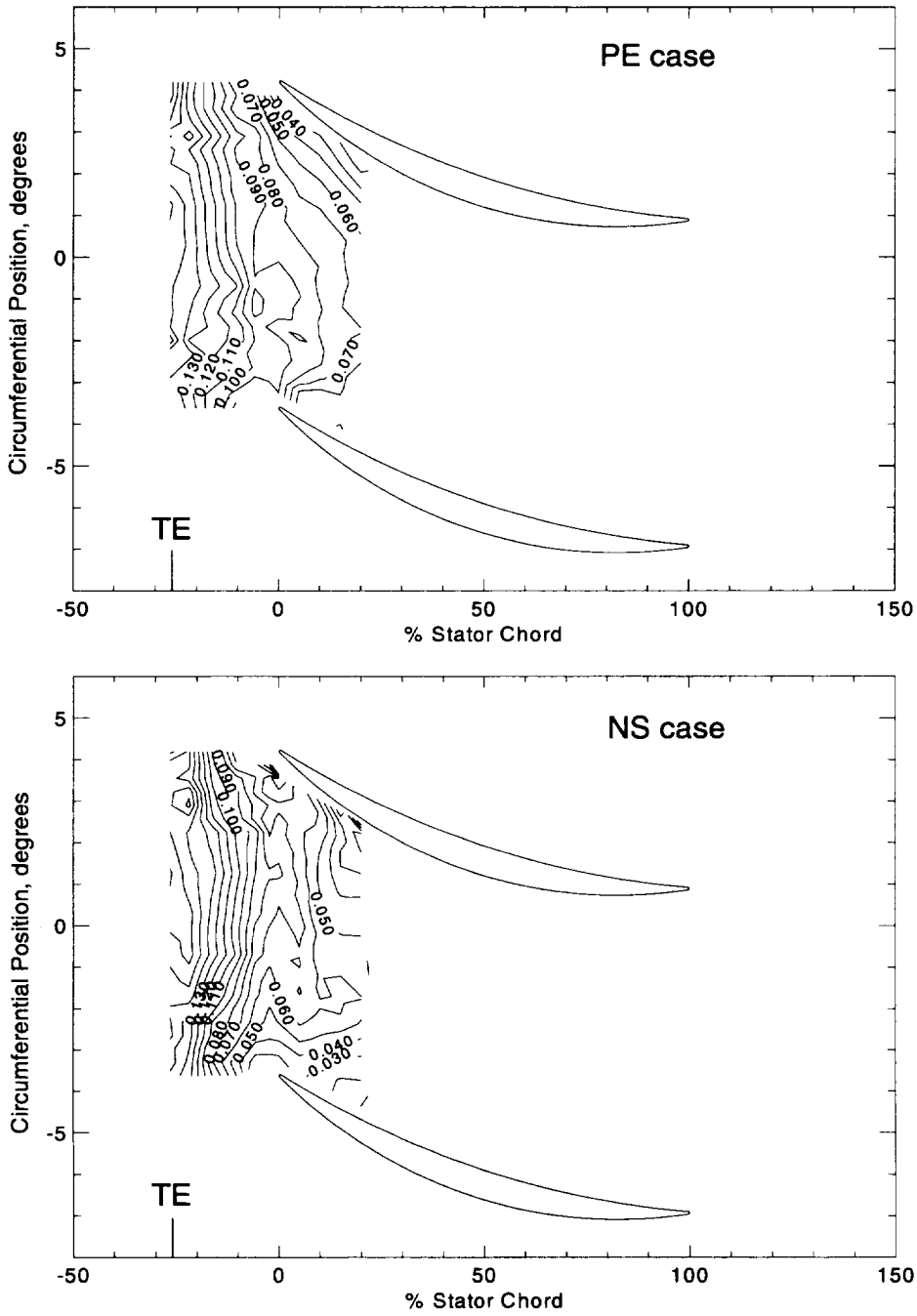

Figure 79. Distribution of disturbance kinetic energy in the stator passage calculated from the LFA data for the PE and NS cases.

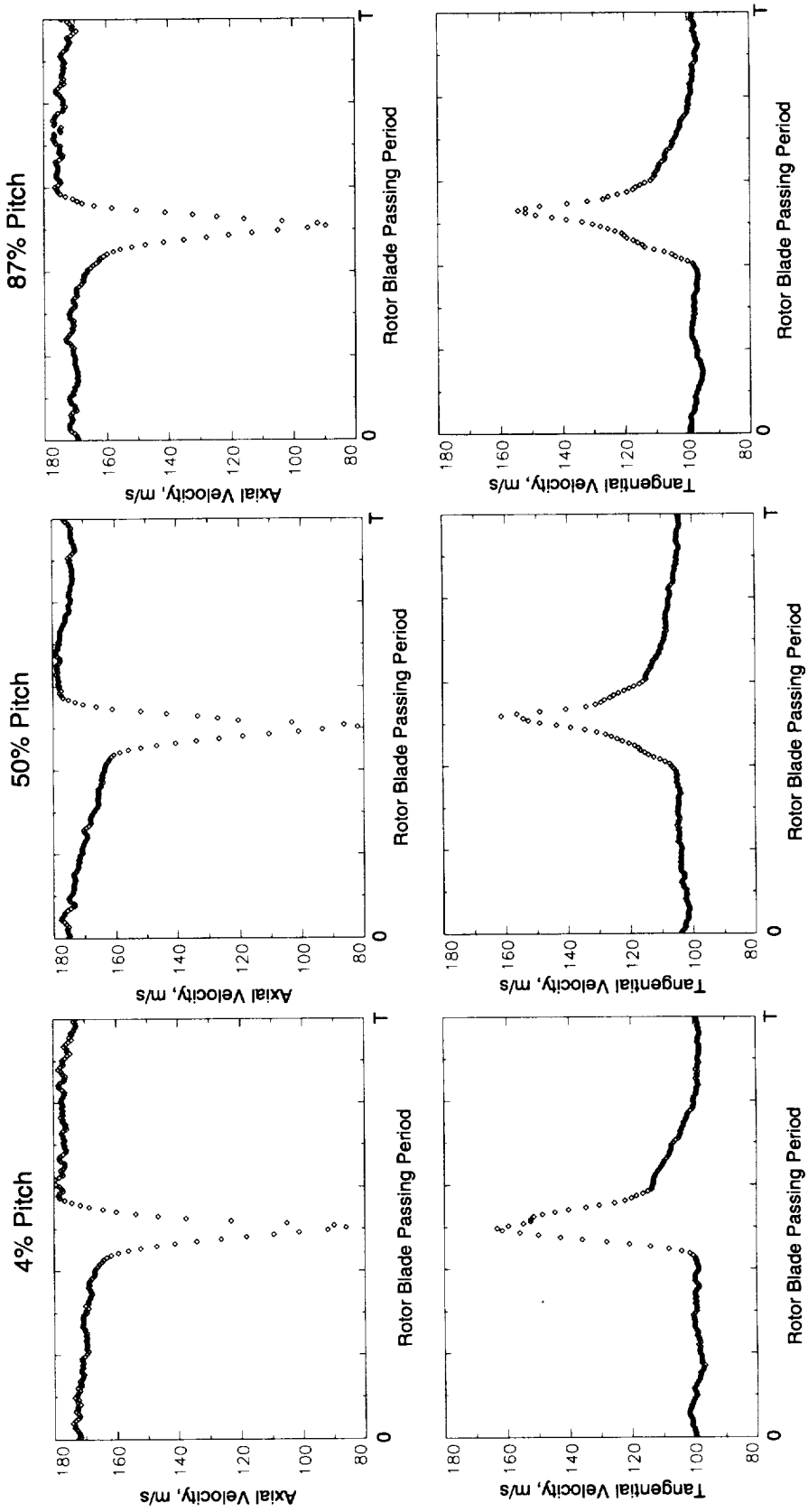

Figure 80. Rotor wake profiles at the rotor trailing edge plane for the PE LFA data.

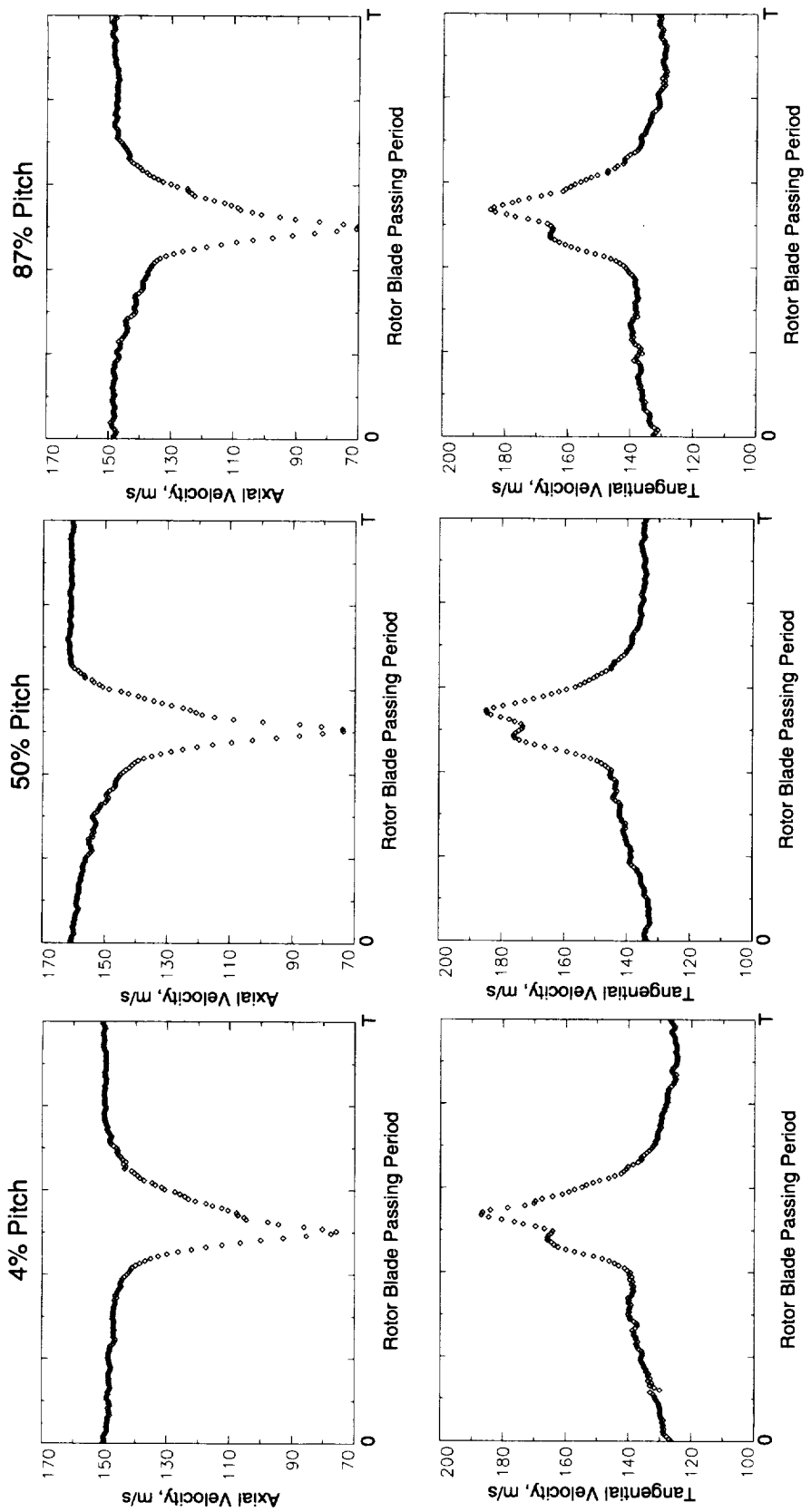

Figure 81. Rotor wake profiles at the rotor trailing edge plane for the NS LFA data.

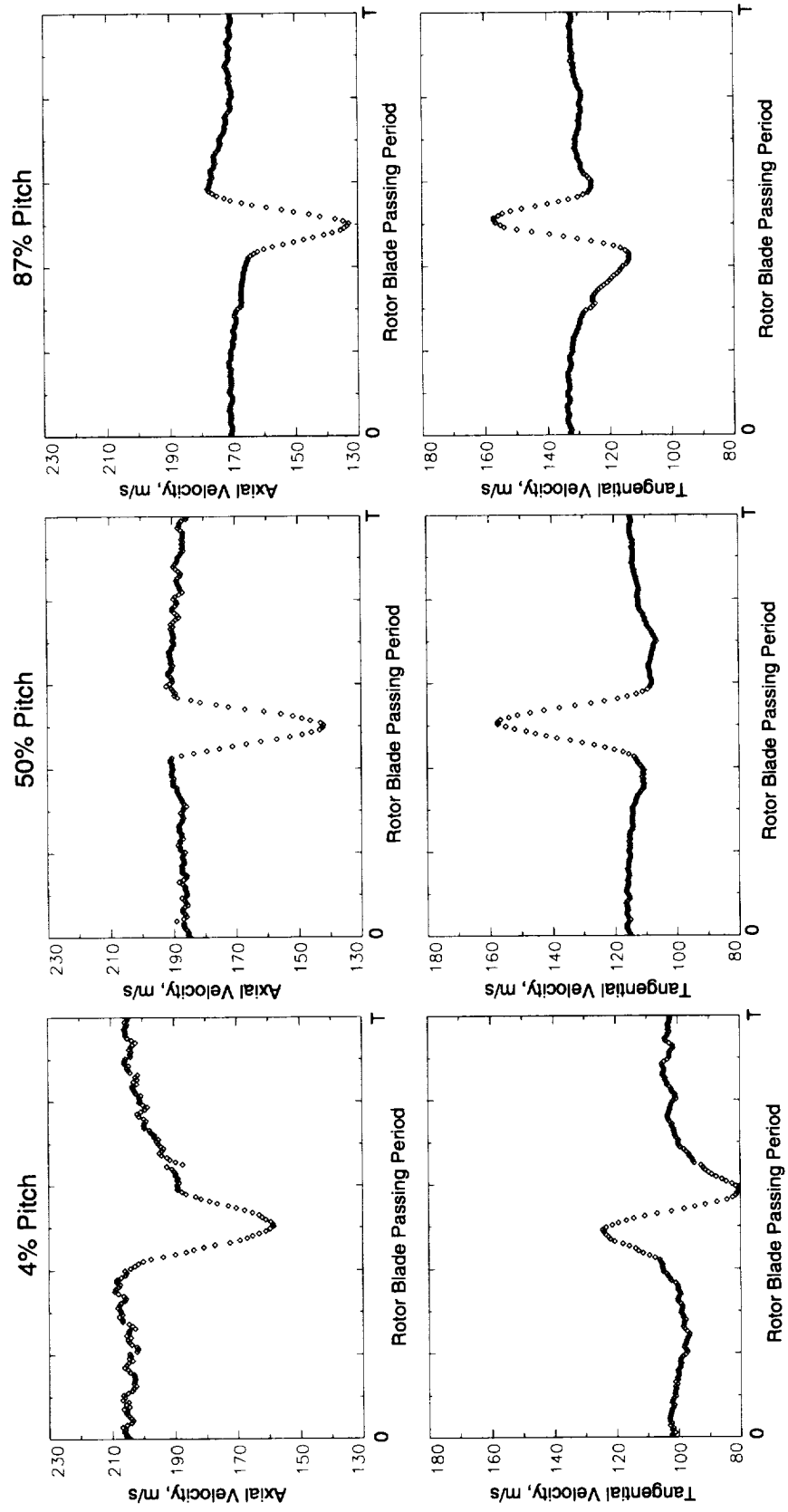

Figure 82. Rotor wake profiles at the stator leading edge plane for the PE LFA data.

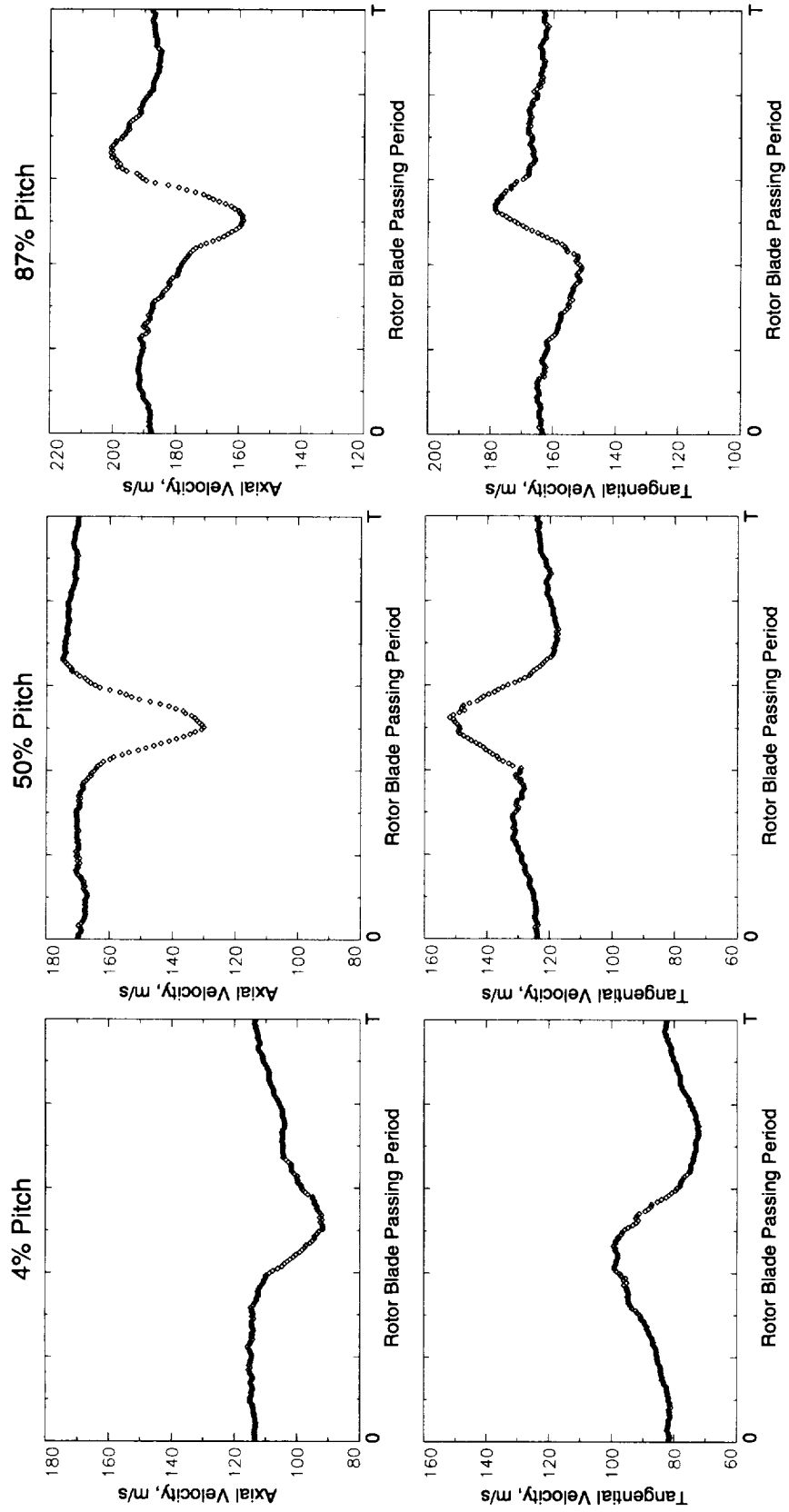

Figure 83. Rotor wake profiles at the stator leading edge plane for the NS LFA data.

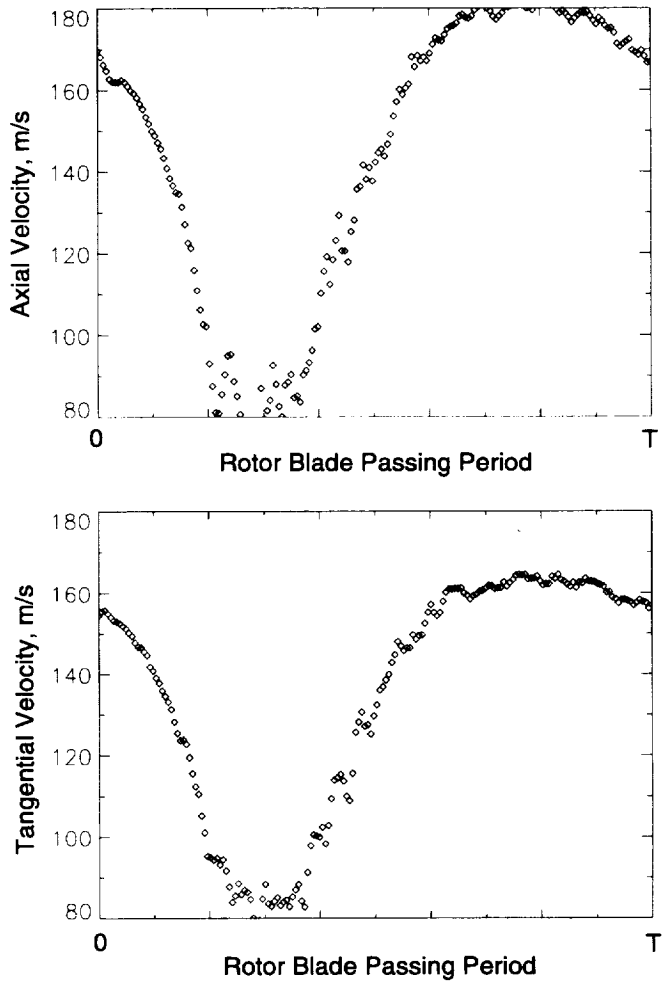

Figure 84. Velocity profile at 96% stator pitch at the stator leading edge plane for the NS LFA data.

B.6 Stator Wake Unsteady Behavior

Figure 85 shows the distribution of DKE at the 90% and 120% stator chord planes. High unsteadiness is present in the shear layers of the stator wake. The stator wakes are relatively narrow so the contribution of the stator wake unsteadiness to the total unsteadiness at 120% chord is small. Figures 86 and 87 show the rotor wake velocity traces for different circumferential locations in the stator wake. The traces from the stator wake edges agree with the traces from the midpitch shown in the body of the thesis which indicated that the rotor wakes are mostly decayed by the stator exit. Velocity traces in the shear layer near the bottom of the stator wake show an unusual two-cycle per rotor blade passing period behavior. These relatively

large velocity fluctuations are responsible for the high unsteadiness values. Because the velocity traces are ensemble averaged, these velocity fluctuations are related to the rotor blade passing period.

Stauter el. al. also observed high levels of unsteadiness in the stator wake which they attributed to remnants of rotor wakes which had gathered in the stator boundary layer. However, in this case the cross-pitch survey at 90% stator chord shown in Figure 85 only indicates increased DKE close to the suction surface in the PE case. Analysis of the unsteady simulations indicates that the source of the unsteadiness may be due to velocity fluctuations which were generated by the wake/stator leading edge interaction and are convected with the boundary layer. This may be the cause for some of the increased unsteadiness for the PE case. The NS case did not show increased unsteadiness in the stator boundary layers and therefore unsteadiness coming from the wake/stator leading edge interaction seems unlikely.

Another possible source of unsteadiness in the stator wakes is generation of unsteadiness at the stator trailing edge due to time varying loading on the stator blade. This would cause vorticity to be shed at the stator trailing edge. More investigation of this phenomenon is planned with the full unsteady simulation which will contain results from multiple stator passages.

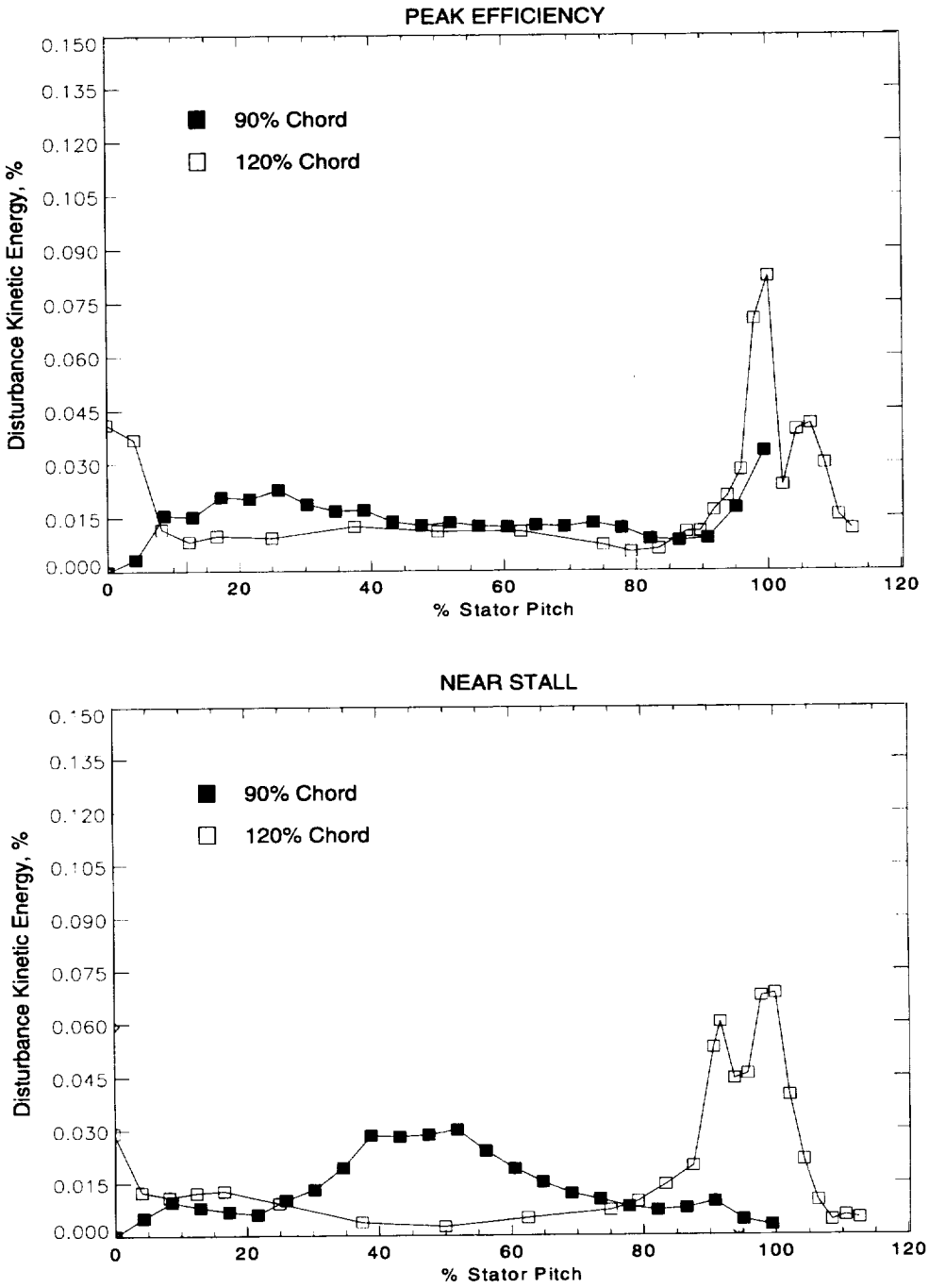

Figure 85. DKE distribution at 90% and 120% stator chord for the PE and NS LFA data.

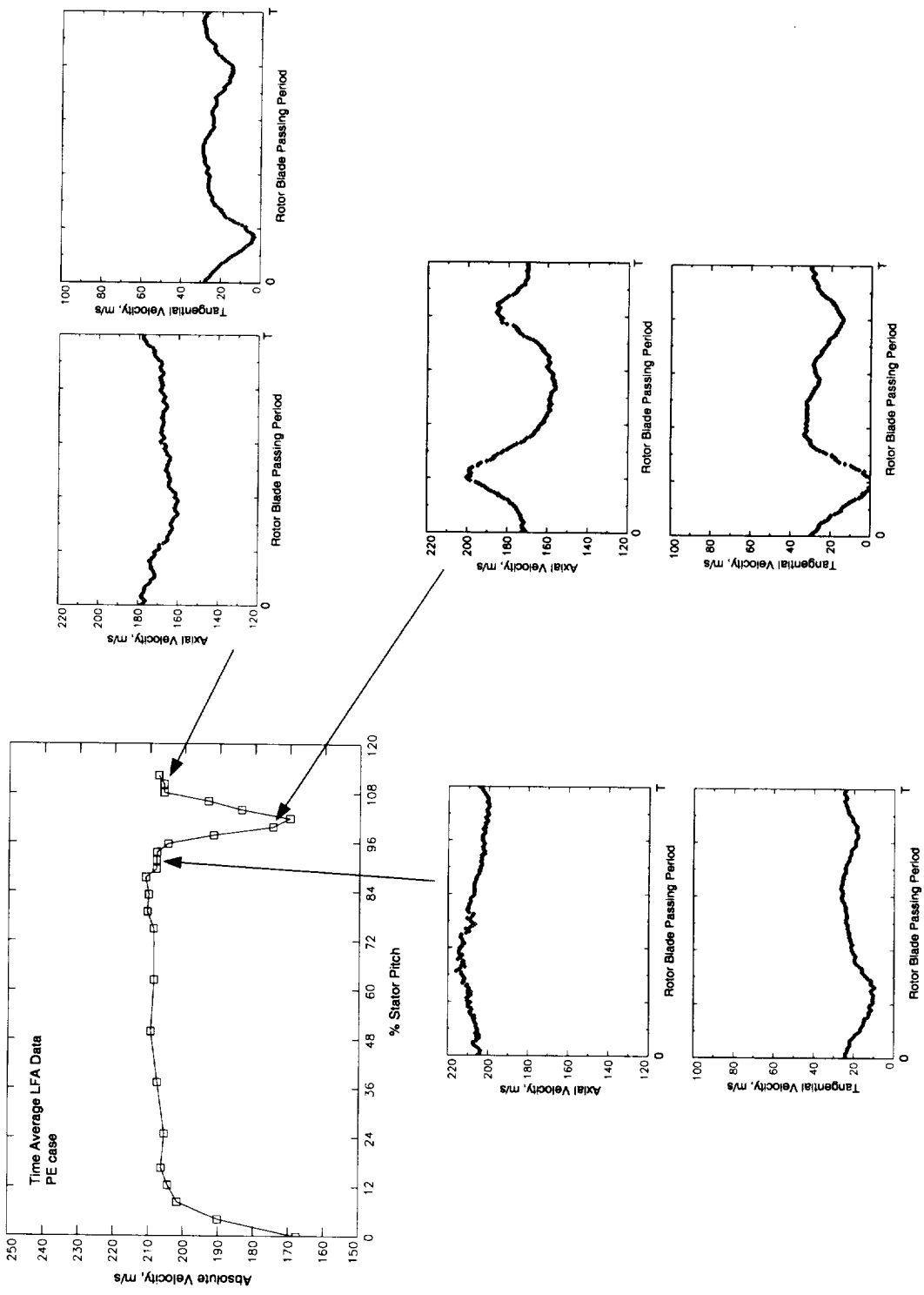

Figure 86. Detailed velocity traces in the stator wake at 120% stator chord for the PE LFA data.

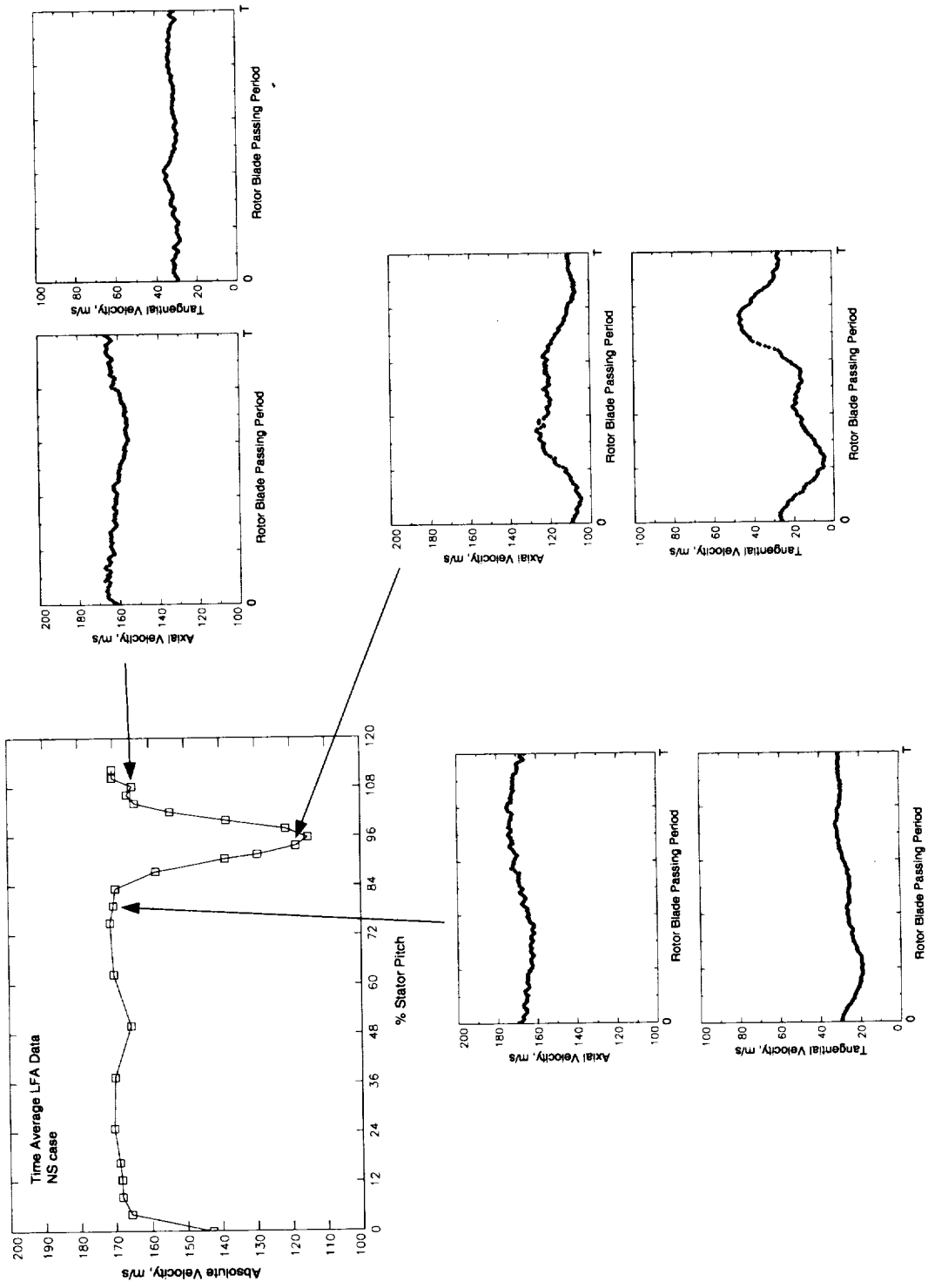

Figure 87. Detailed velocity traces in the stator wake at 120% stator chord for the NS LFA data.

B.7 Rotor Only Data: Peak Efficiency

The following figures show rotor wake profiles from the rotor in isolation test.

Peak Efficiency

Rotor Trailing Edge

Not Available

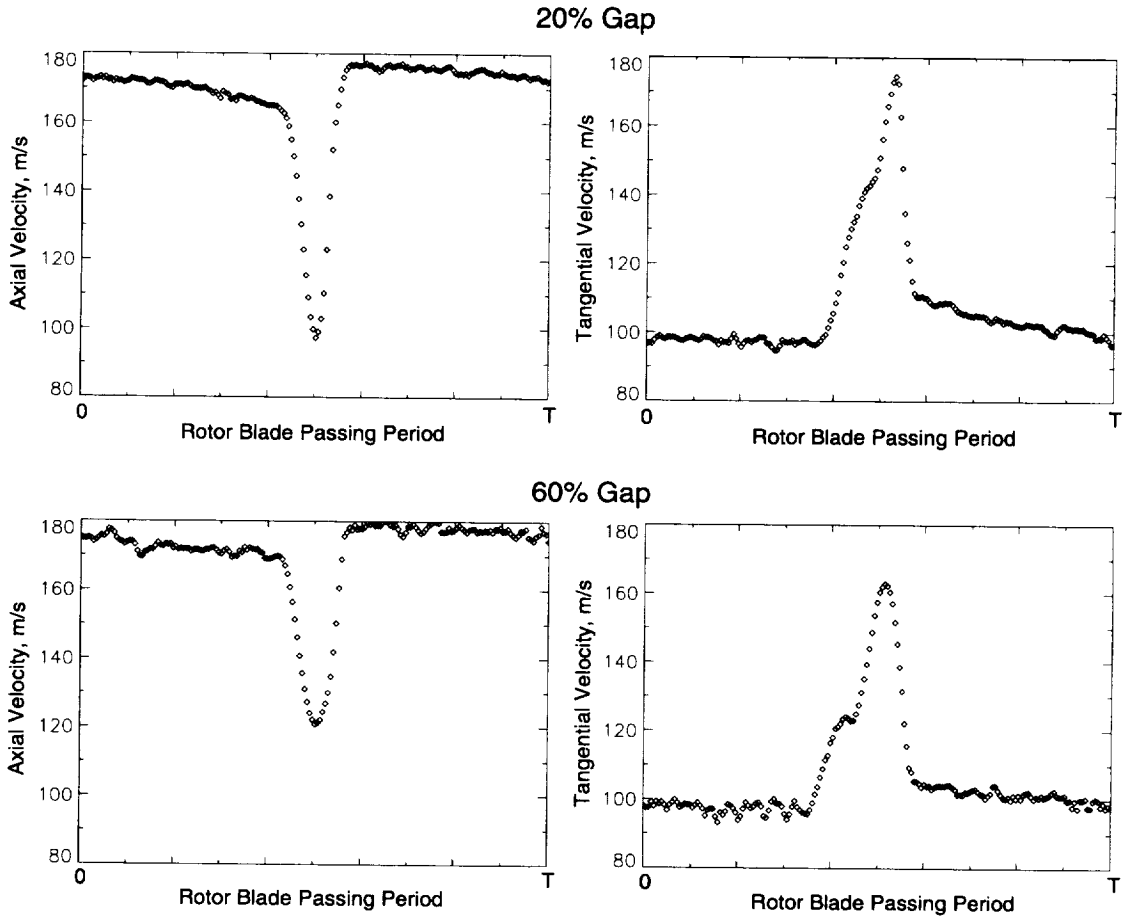

Figure 88. Rotor wake profiles in the rotor/stator gap for the peak efficiency rotor in isolation test.

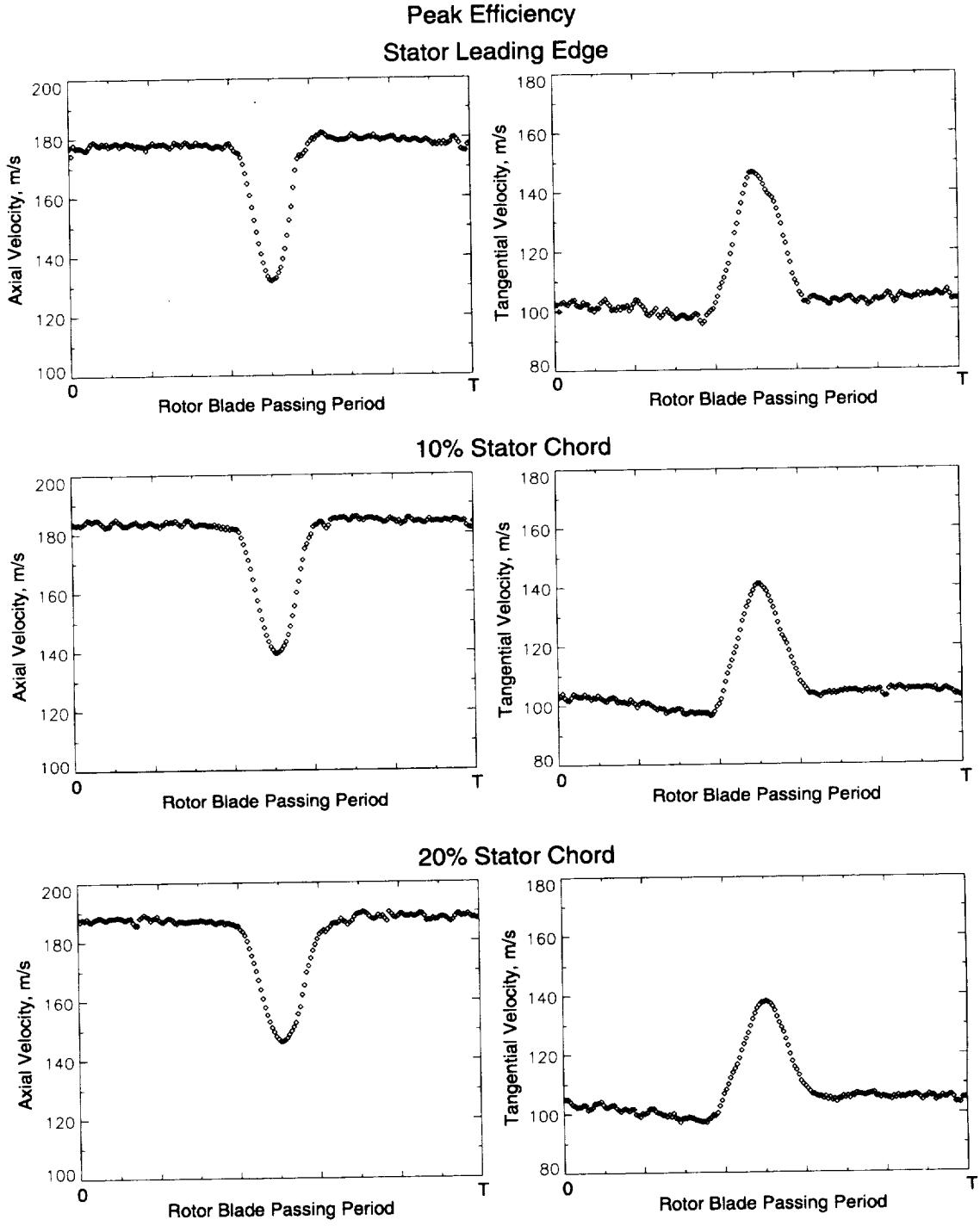

Figure 89. Rotor wake profiles at the stator passage entrance for the peak efficiency rotor in isolation test.

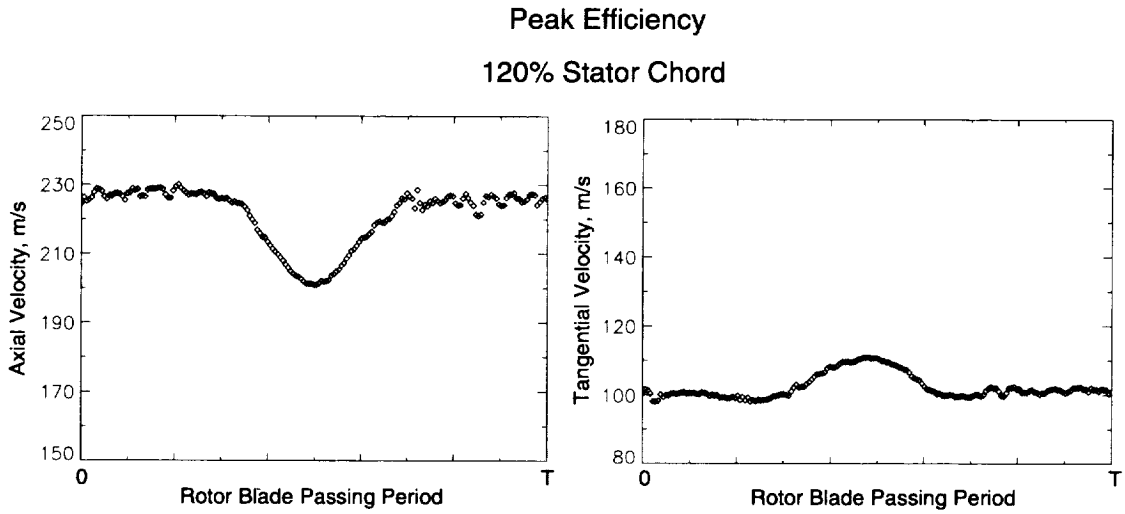

Figure 90. Rotor wake profile downstream of the stator passage for the peak efficiency rotor in isolation test.

B.8 Rotor Only Data: Near Stall

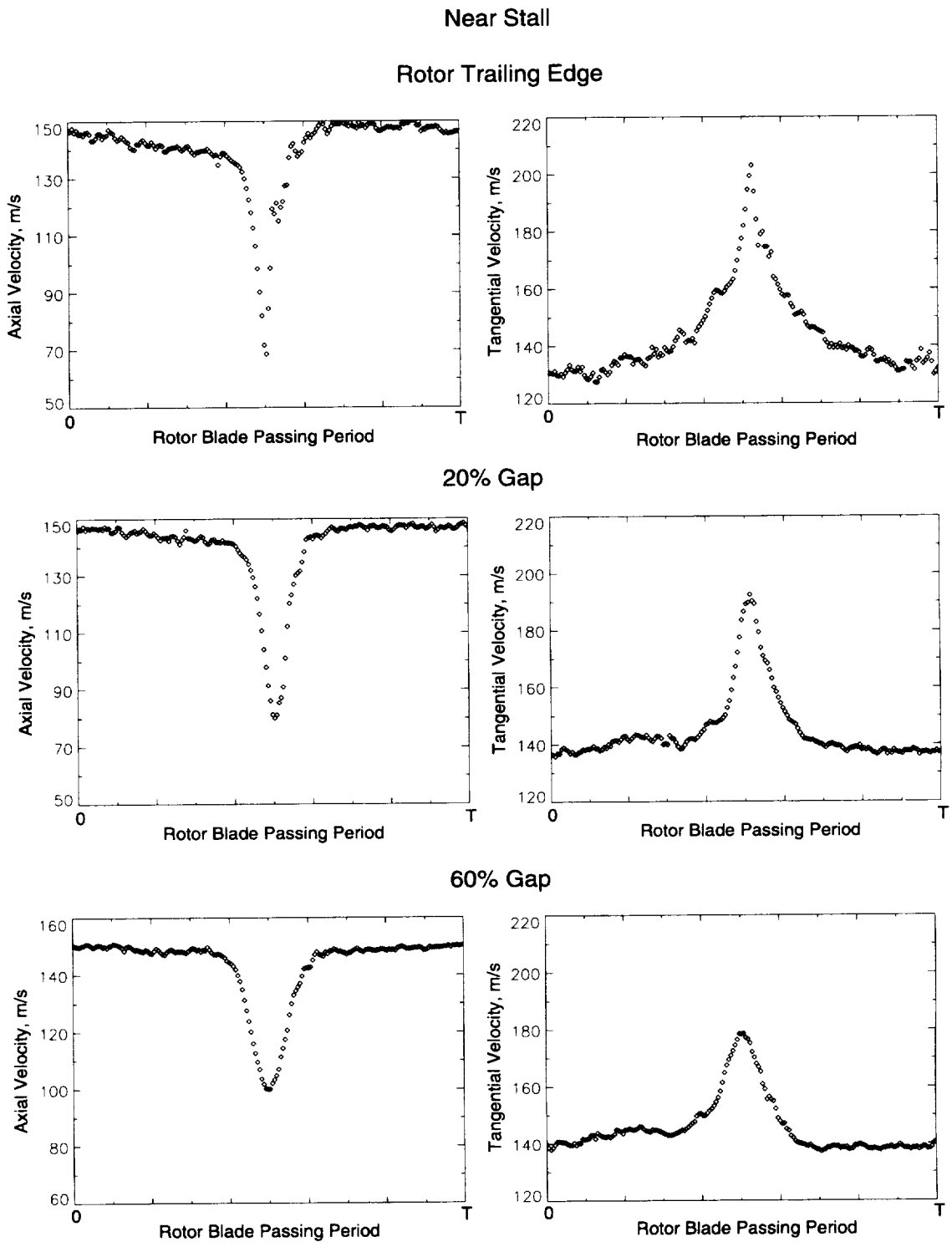

Figure 91. Rotor wake profiles in the rotor/stator gap for the near stall rotor in isolation test.

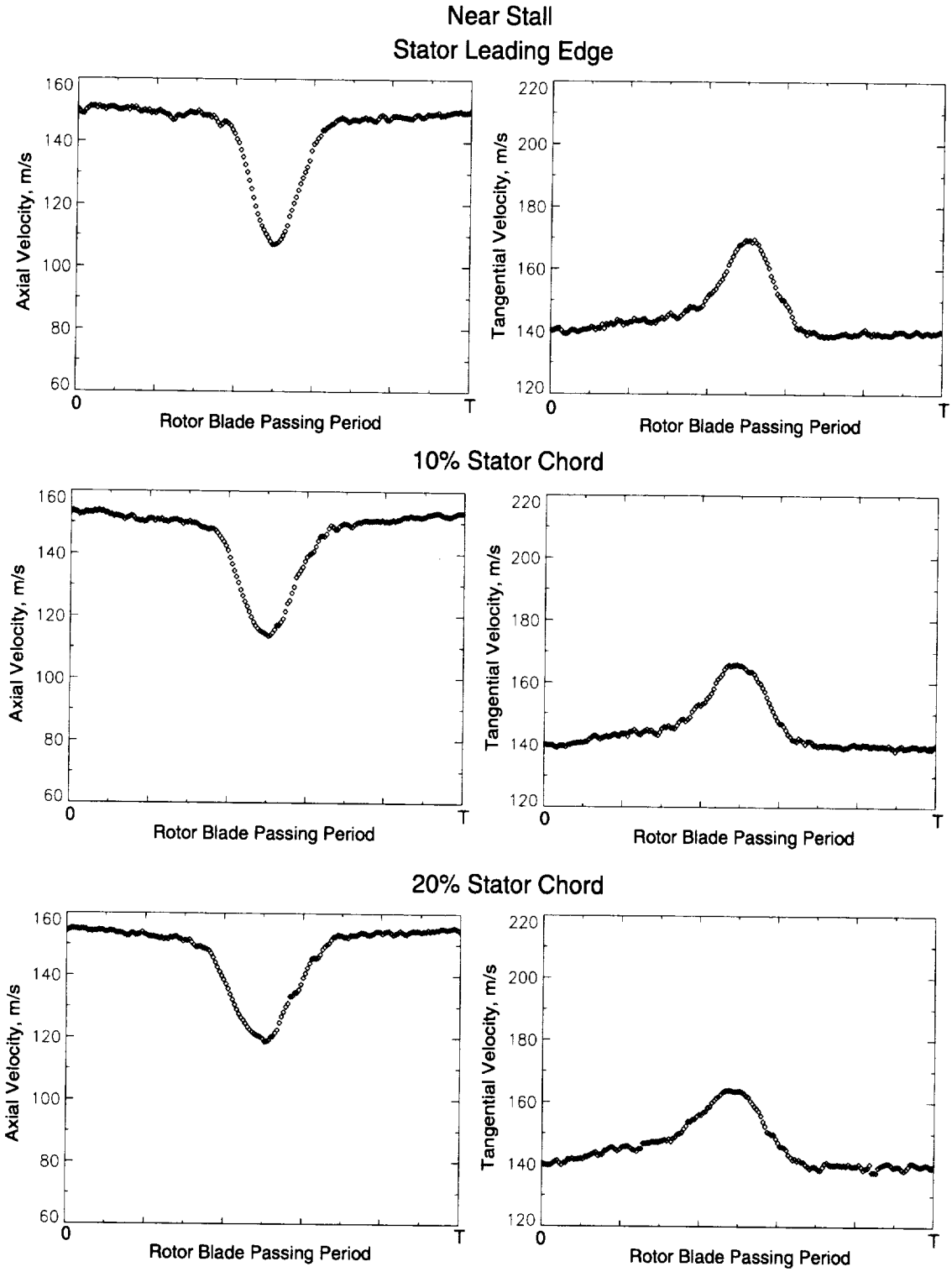

Figure 92. Rotor wake profiles in the entrance to the stator passage for the near stall rotor in isolation test.

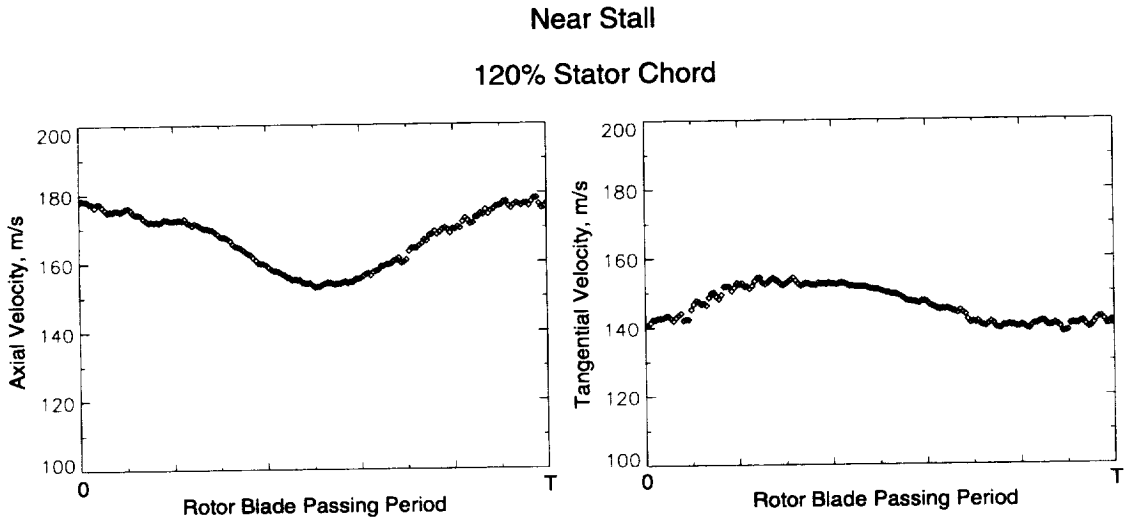

Figure 93. Rotor wake profiles downstream of the stator passage for the near stall rotor in isolation test.

APPENDIX C: SIMULATION RESULTS

This chapter contains contour plots of relative velocity magnitude at the same time steps of the rotor blade passing period as the LFA data. Radial velocities ARE included in the calculation. Note that there are only 14 plots here. The 1st and 15th plots in the LFA data are at essentially the same time step and likewise the 15th plot of the simulation results would be identical to the 1st.

C.1 Peak Efficiency Simulations

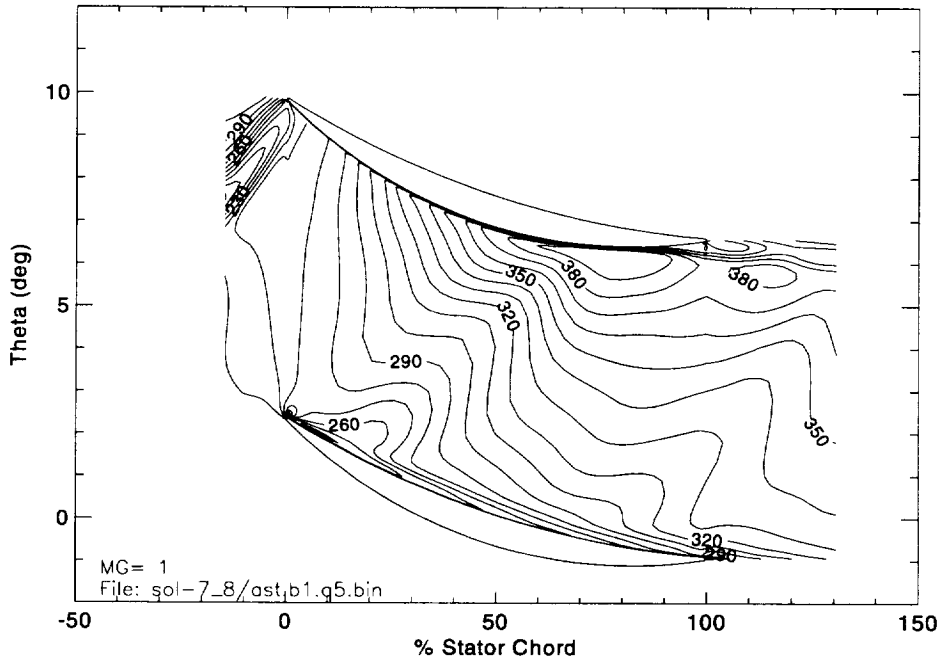

Figure 94. Relative velocity magnitude (m/s) for rotor position 1 of 15 for peak efficiency MSU-TURBO simulation.

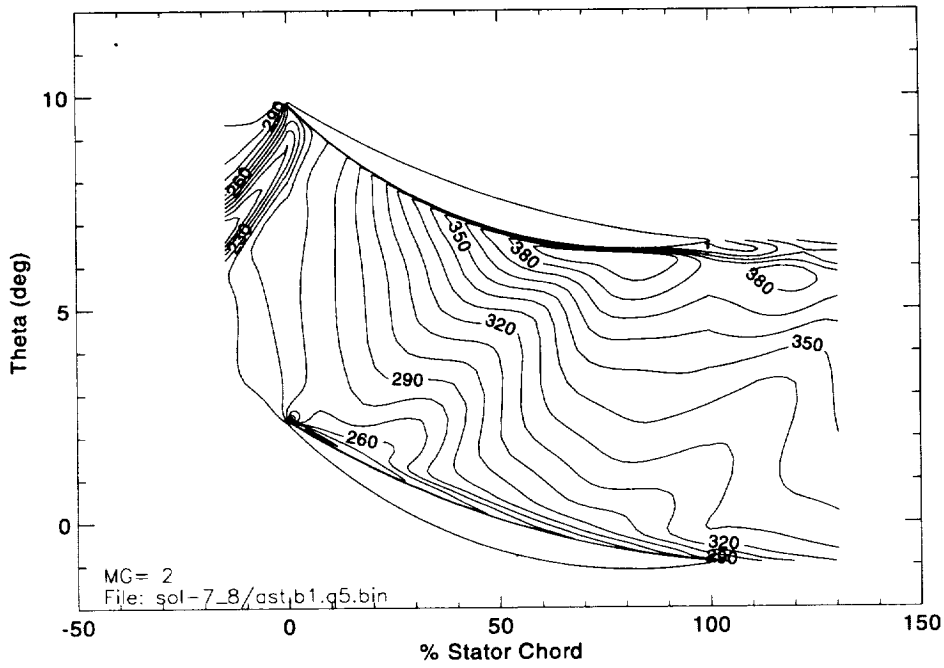

Figure 95. Relative velocity magnitude (m/s) for rotor position 2 of 15 for peak efficiency MSU-TURBO simulation.

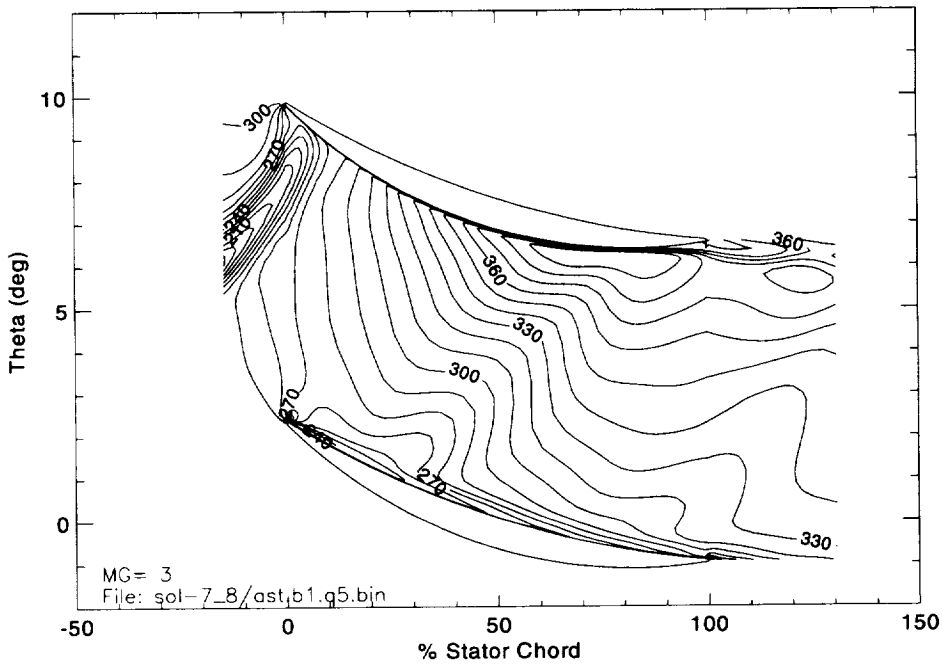

Figure 96. Relative velocity magnitude (m/s) for rotor position 3 of 15 for peak efficiency MSU-TURBO simulation.

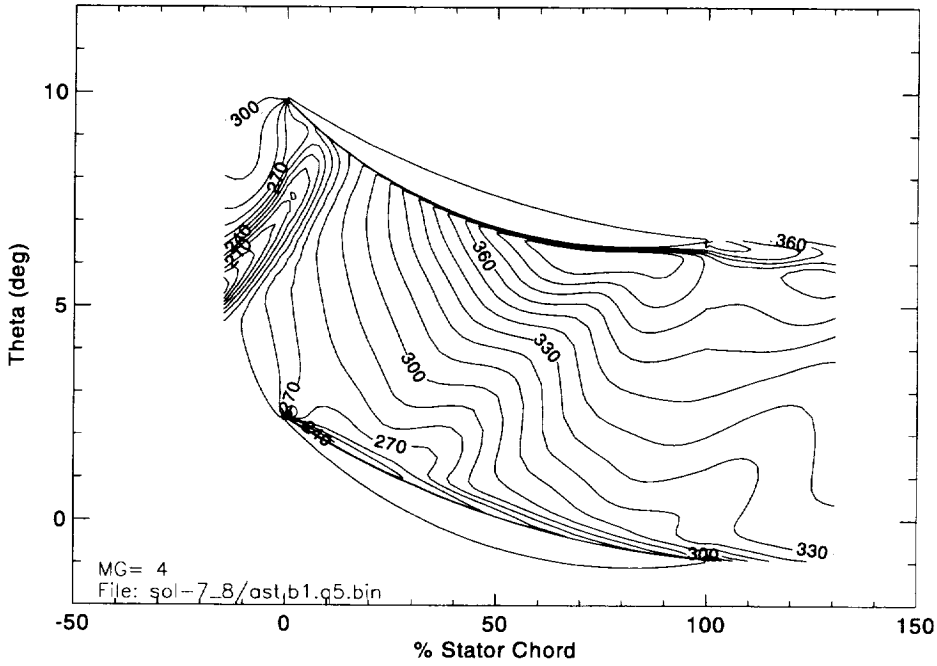

Figure 97. Relative velocity magnitude (m/s) for rotor position 4 of 15 for peak efficiency MSU-TURBO simulation.

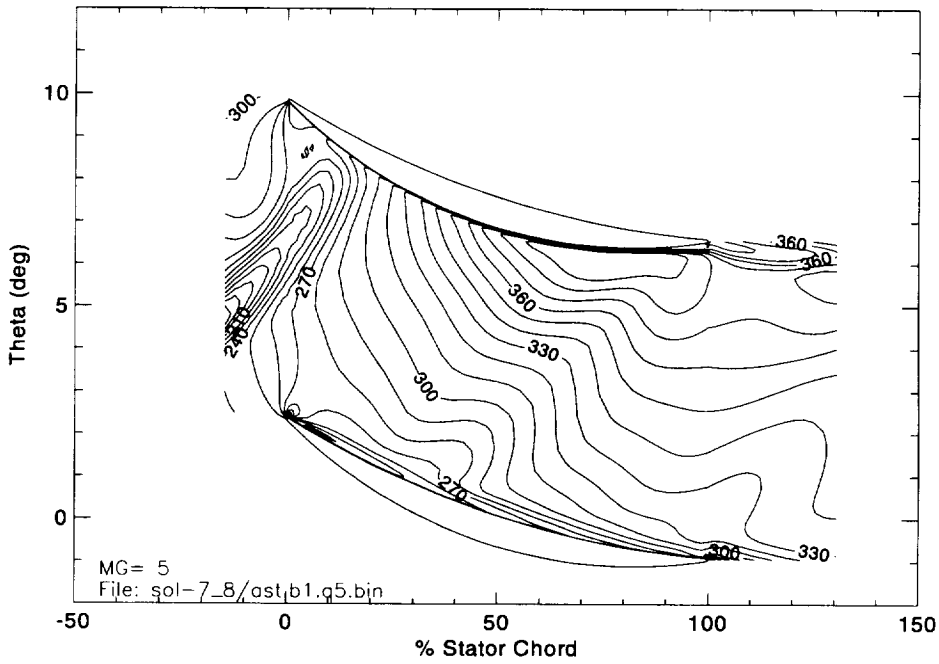

Figure 98. Relative velocity magnitude (m/s) for rotor position 5 of 15 for peak efficiency MSU-TURBO simulation.

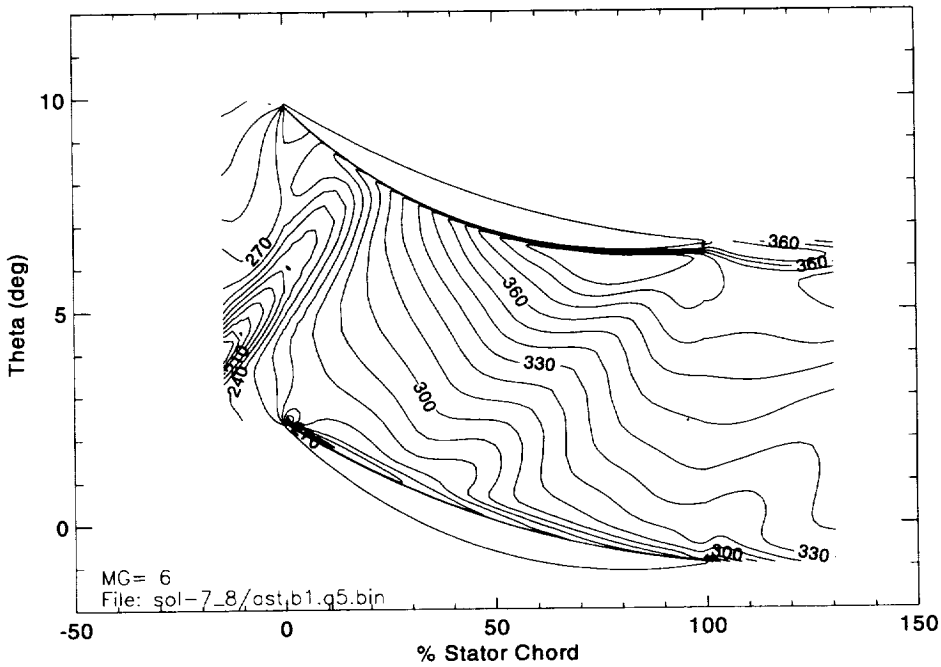

Figure 99. Relative velocity magnitude (m/s) for rotor position 6 of 15 for peak efficiency MSU-TURBO simulation.

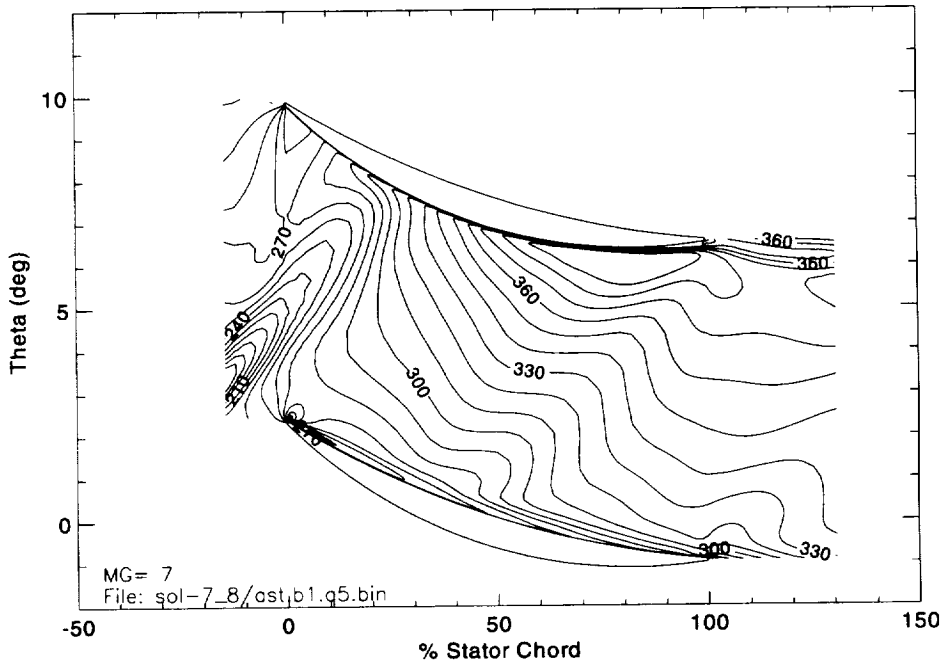

Figure 100. Relative velocity magnitude (m/s) for rotor position 7 of 15 for peak efficiency MSU-TURBO simulation.

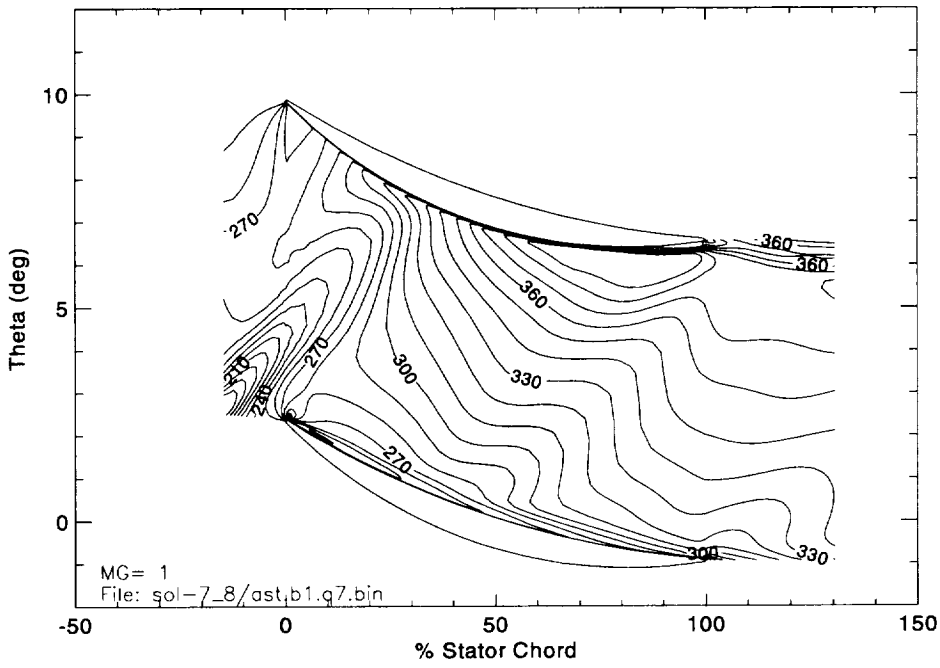

Figure 101. Relative velocity magnitude (m/s) for rotor position 8 of 15 for peak efficiency MSU-TURBO simulation.

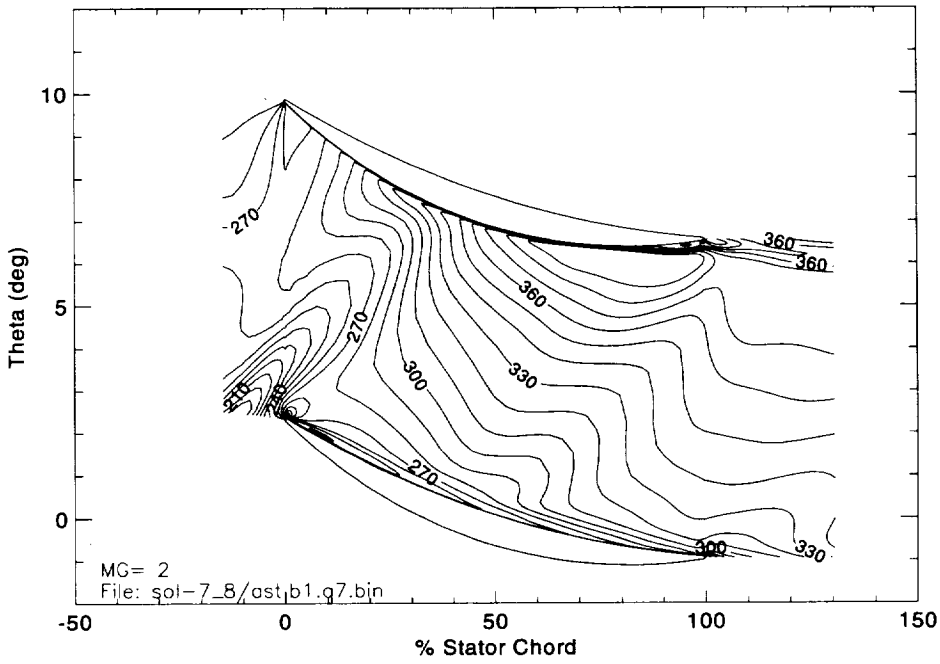

Figure 102. Relative velocity magnitude (m/s) for rotor position 9 of 15 for peak efficiency MSU-TURBO simulation.

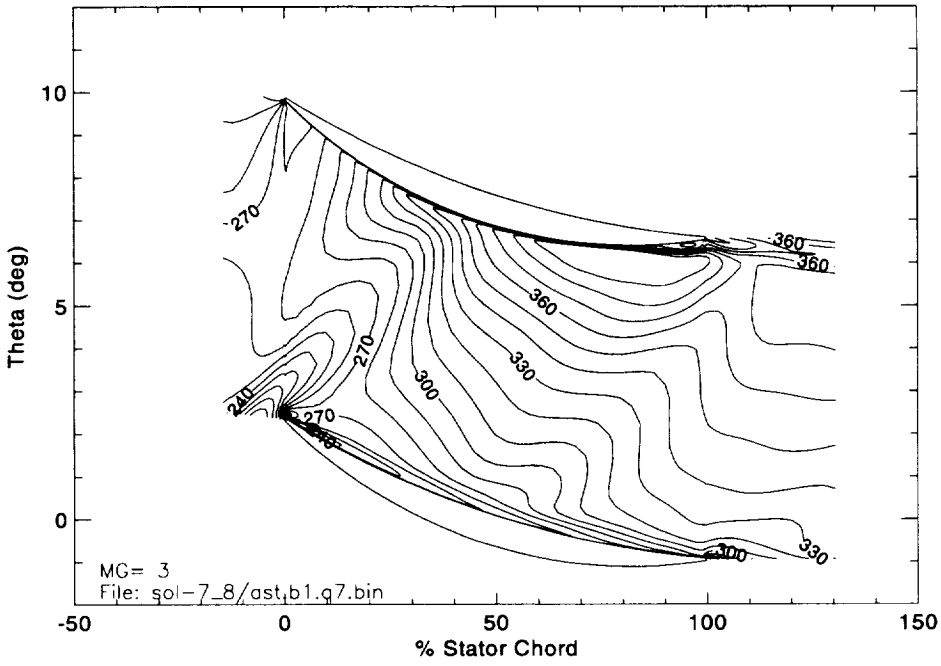

Figure 103. Relative velocity magnitude (m/s) for rotor position 10 of 15 for peak efficiency MSU-TURBO simulation.

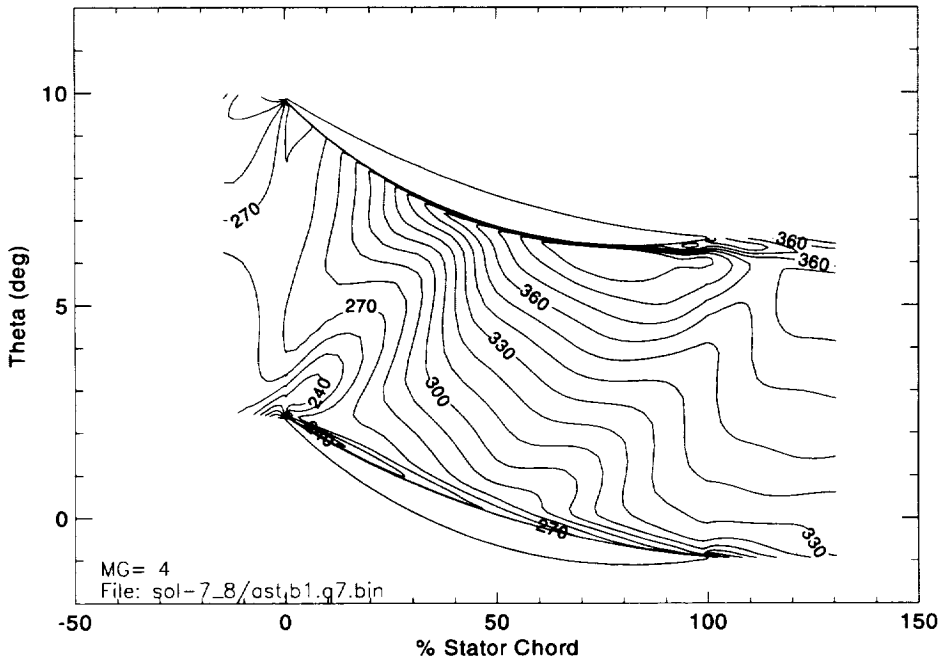

Figure 104. Relative velocity magnitude (m/s) for rotor position 11 of 15 for peak efficiency MSU-TURBO simulation.

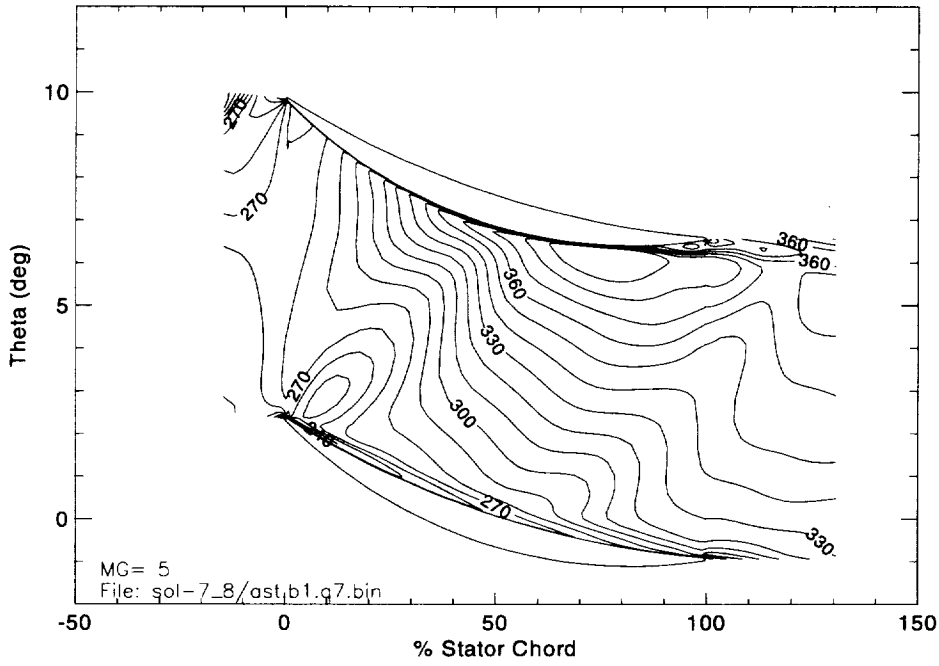

Figure 105. Relative velocity magnitude (m/s) for rotor position 12 of 15 for peak efficiency MSU-TURBO simulation.

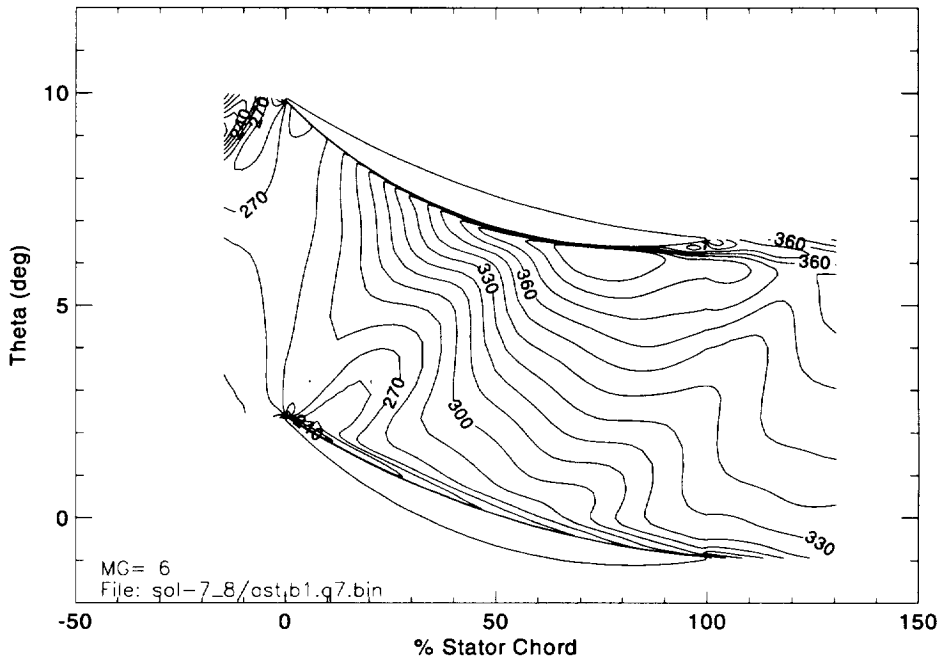

Figure 106. Relative velocity magnitude (m/s) for rotor position 13 of 15 for peak efficiency MSU-TURBO simulation.

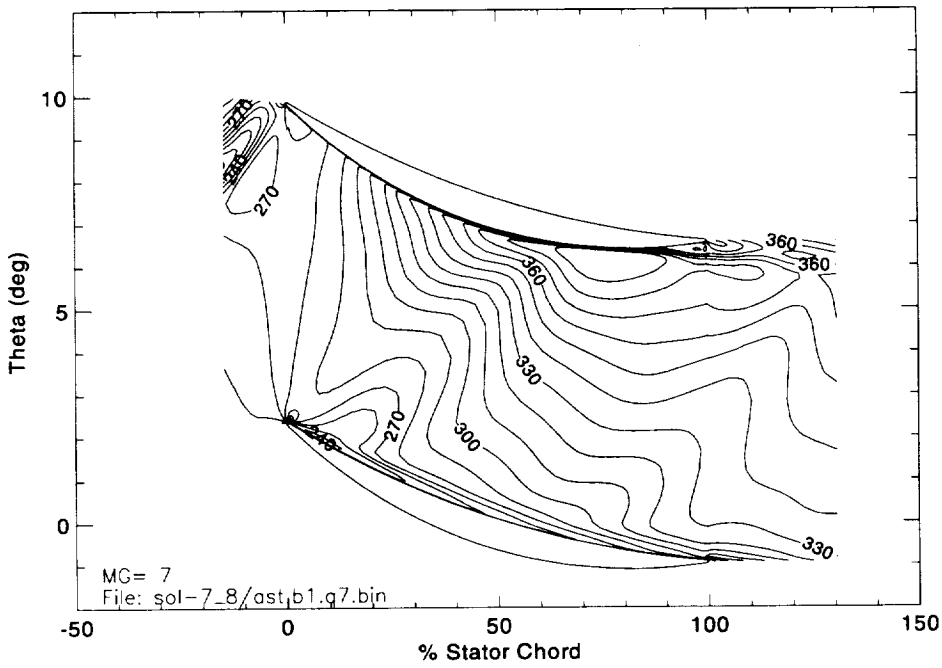

Figure 107. Relative velocity magnitude (m/s) for rotor position 14 of 15 for peak efficiency MSU-TURBO simulation.

C.2 Near Stall Simulations

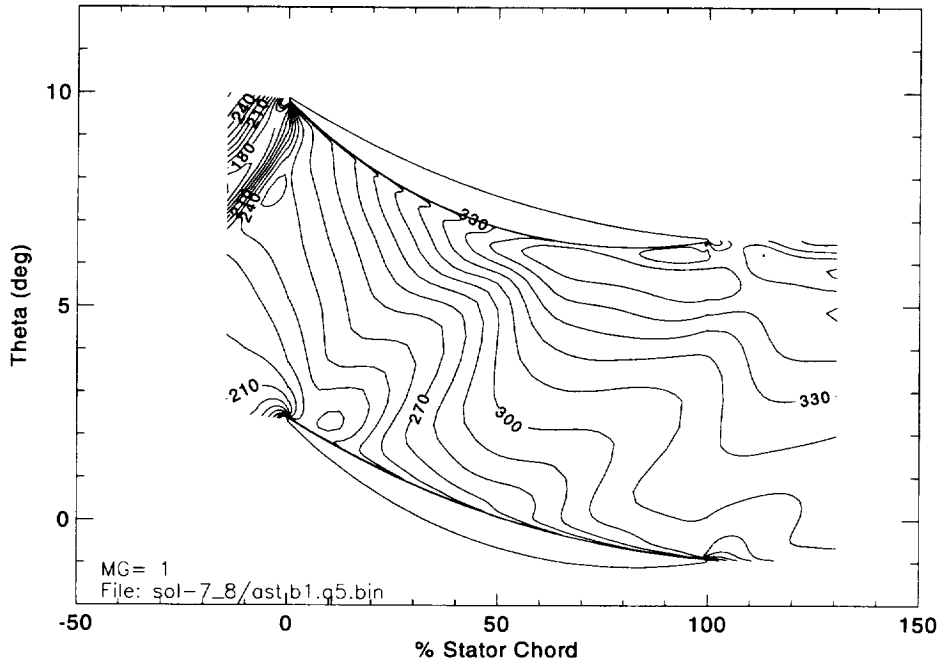

Figure 108. Relative velocity magnitude (m/s) for rotor position 1 of 15 for near stall MSU-TURBO simulation.

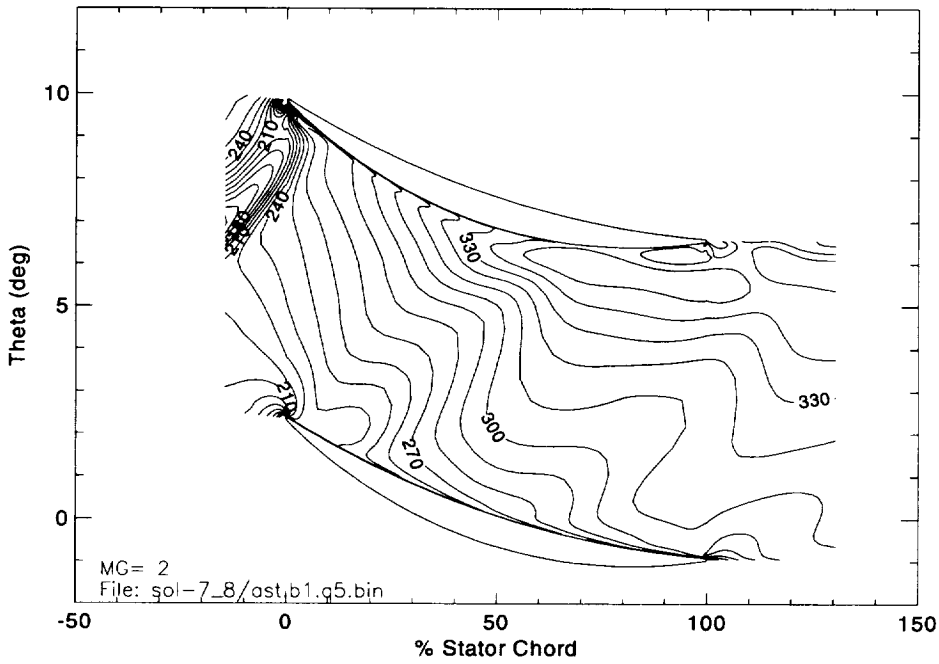

Figure 109. Relative velocity magnitude (m/s) for rotor position 2 of 15 for near stall MSU-TURBO simulation.

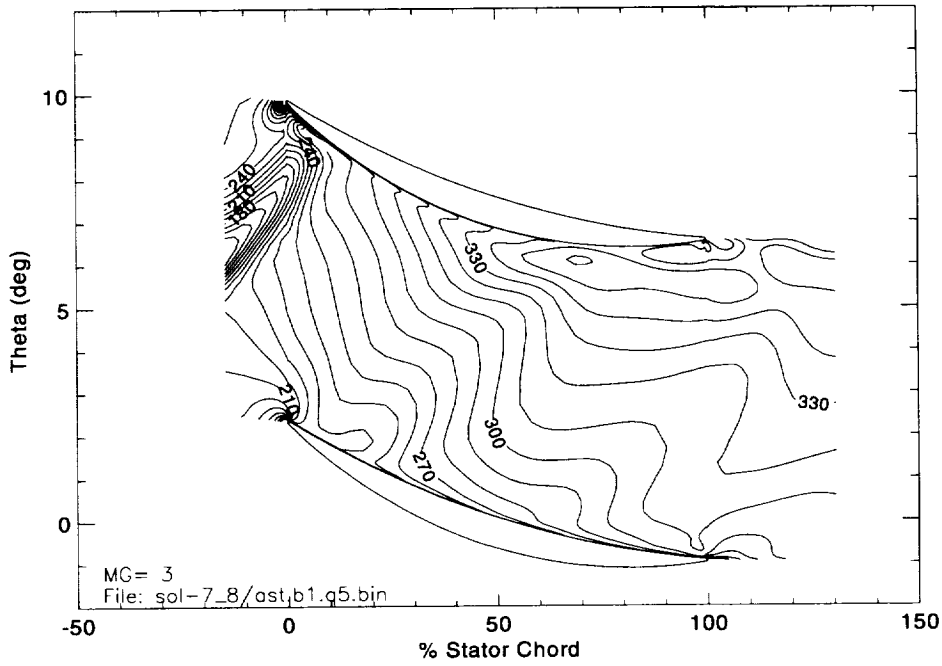

Figure 110. Relative velocity magnitude (m/s) for rotor position 3 of 15 for near stall MSU-TURBO simulation.

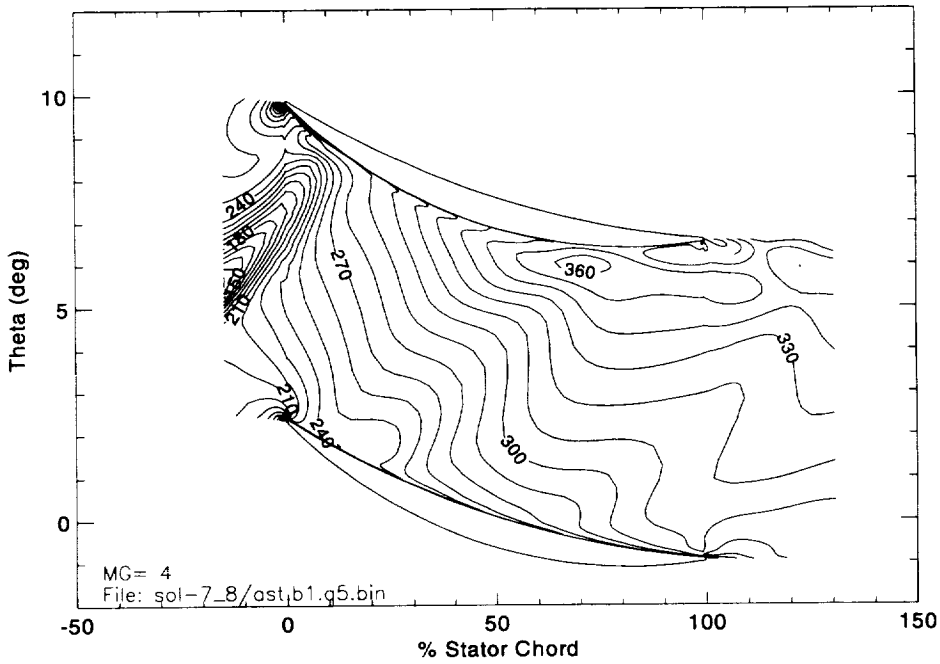

Figure 111. Relative velocity magnitude (m/s) for rotor position 4 of 15 for near stall MSU-TURBO simulation.

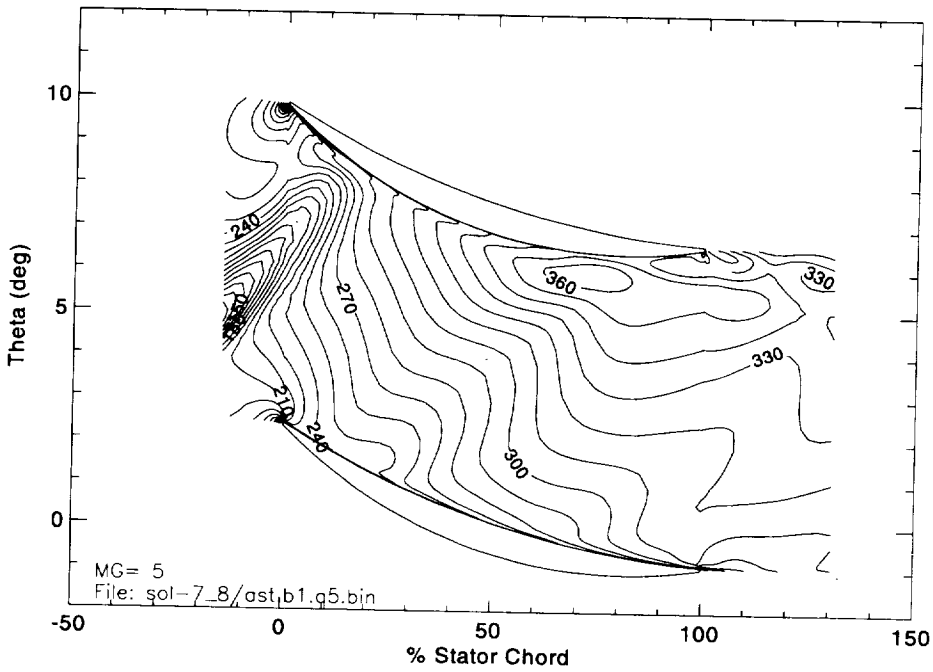

Figure 112. Relative velocity magnitude (m/s) for rotor position 5 of 15 for near stall MSU-TURBO simulation.

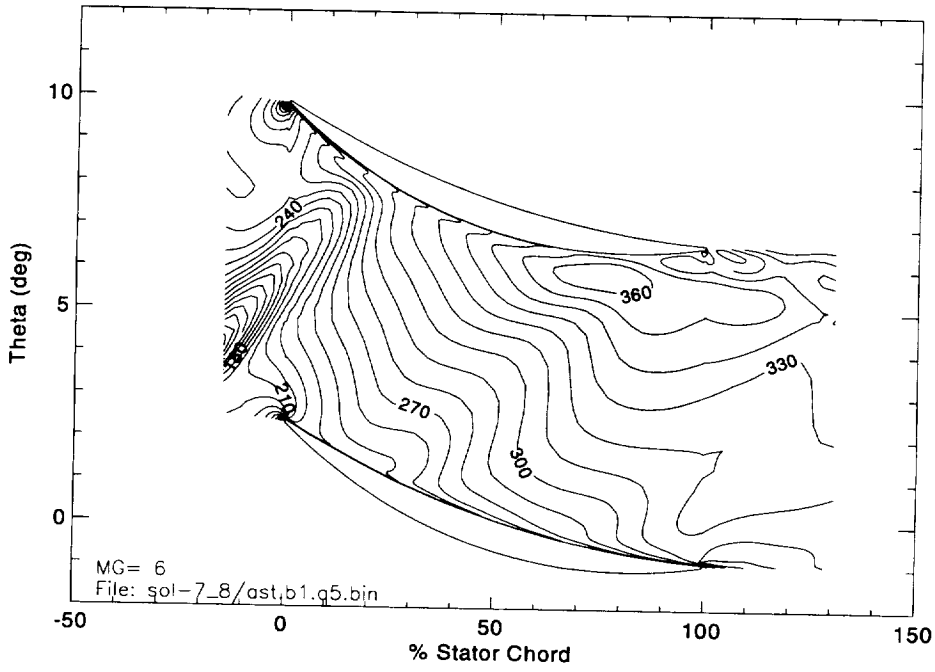

Figure 113. Relative velocity magnitude (m/s) for rotor position 6 of 15 for near stall MSU-TURBO simulation.

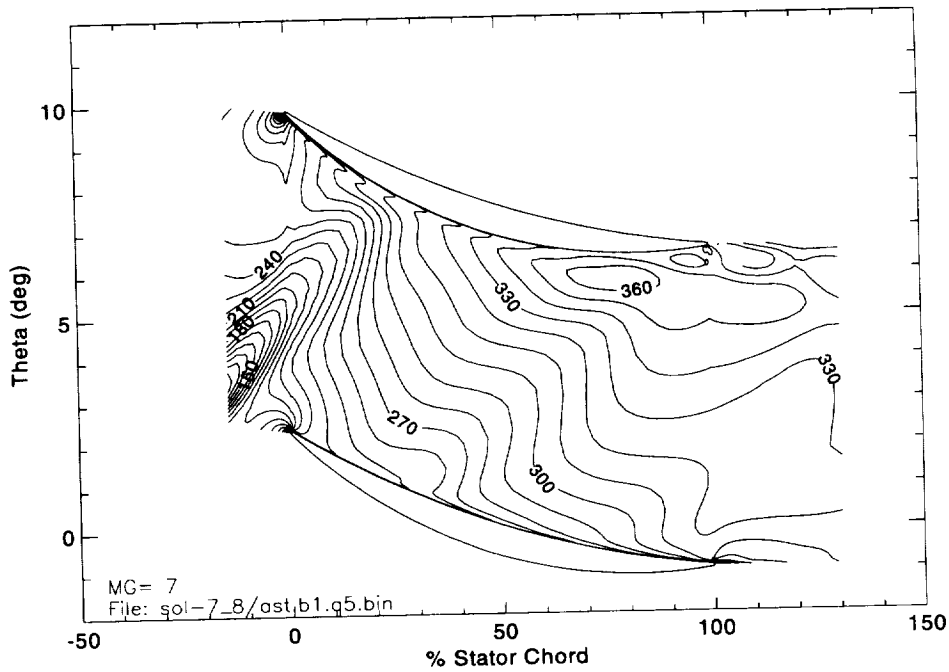

Figure 114. Relative velocity magnitude (m/s) for rotor position 7 of 15 for near stall MSU-TURBO simulation.

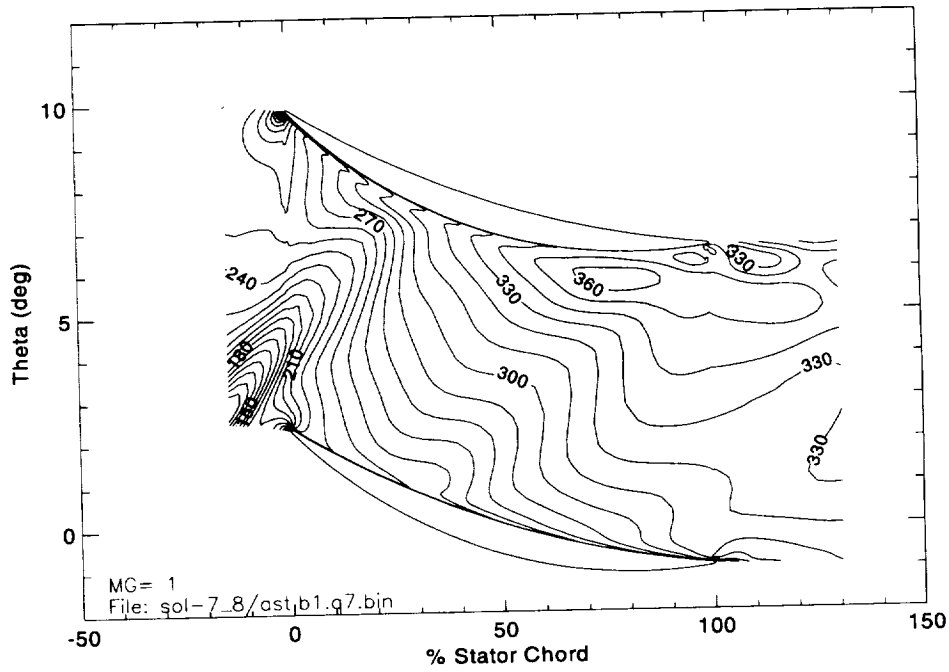

Figure 115. Relative velocity magnitude (m/s) for rotor position 8 of 15 for near stall MSU-TURBO simulation.

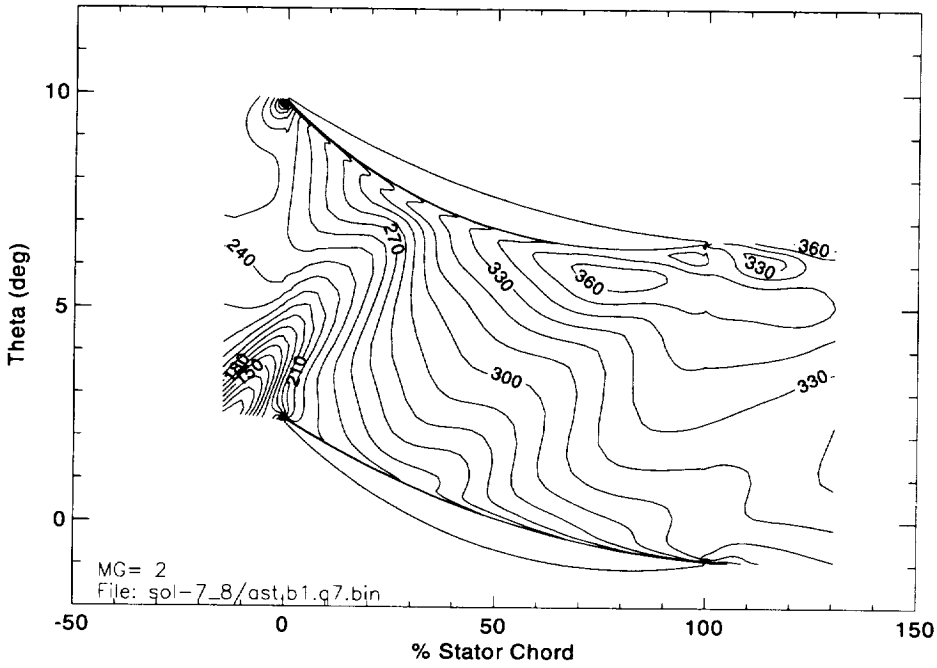

Figure 116. Relative velocity magnitude (m/s) for rotor position 9 of 15 for near stall MSU-TURBO simulation.

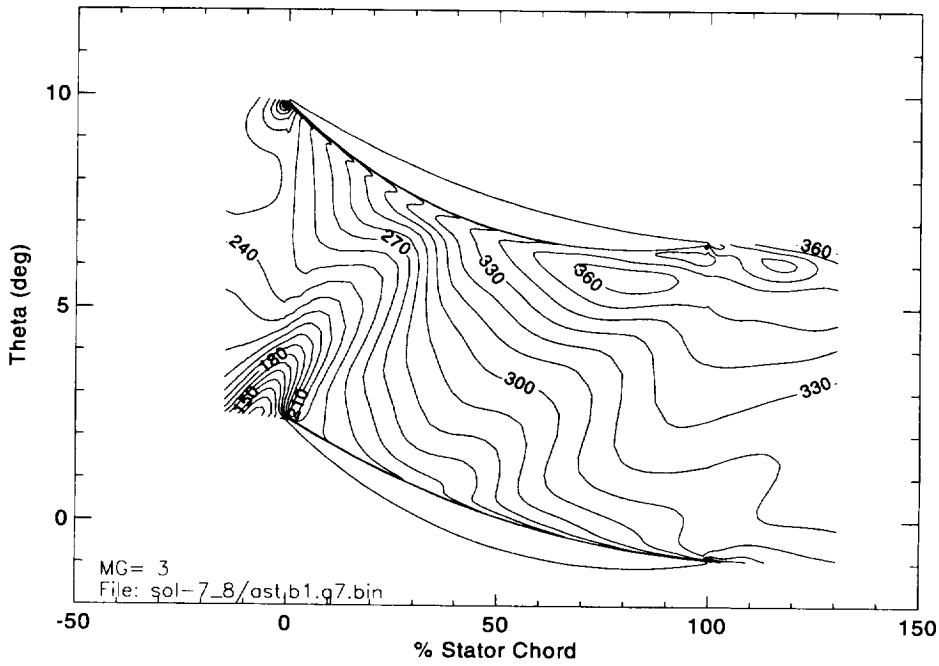

Figure 117. Relative velocity magnitude (m/s) for rotor position 10 of 15 for near stall MSU-TURBO simulation.

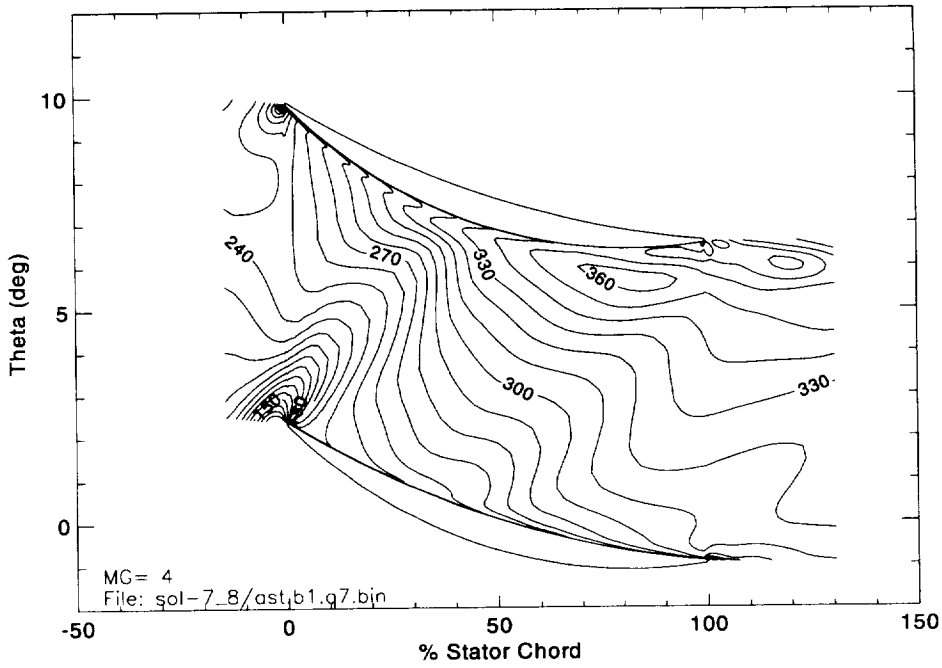

Figure 118. Relative velocity magnitude (m/s) for rotor position 11 of 15 for near stall MSU-TURBO simulation.

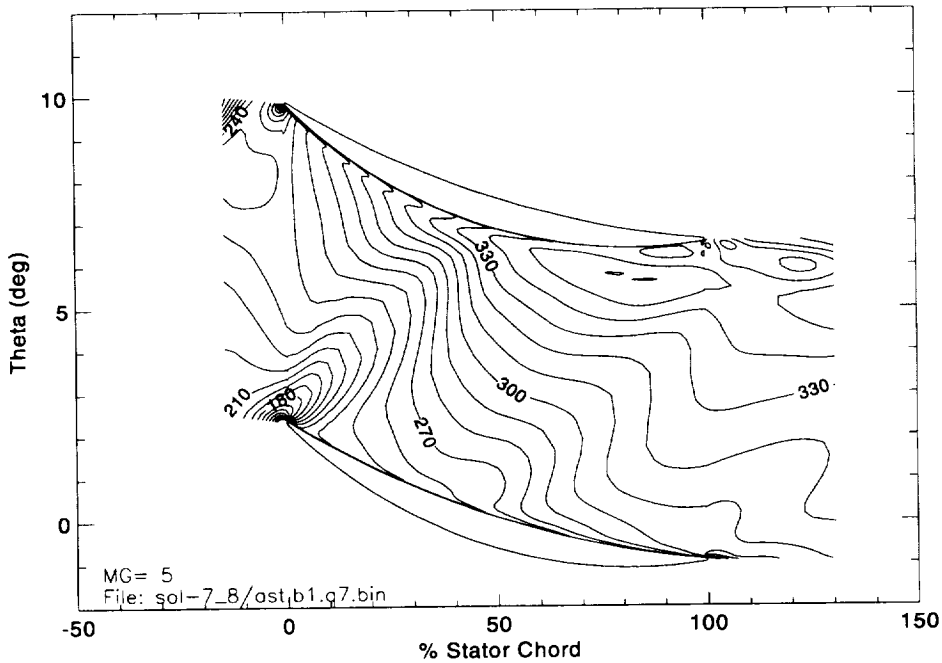

Figure 119. Relative velocity magnitude (m/s) for rotor position 12 of 15 for near stall MSU-TURBO simulation.

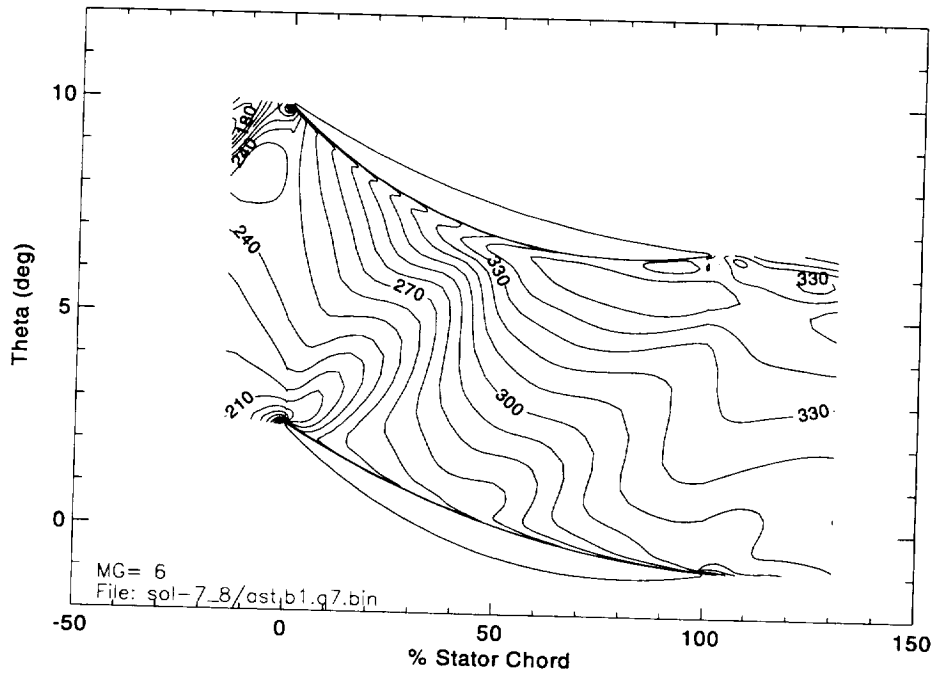

Figure 120. Relative velocity magnitude (m/s) for rotor position 13 of 15 for near stall MSU-TURBO simulation.

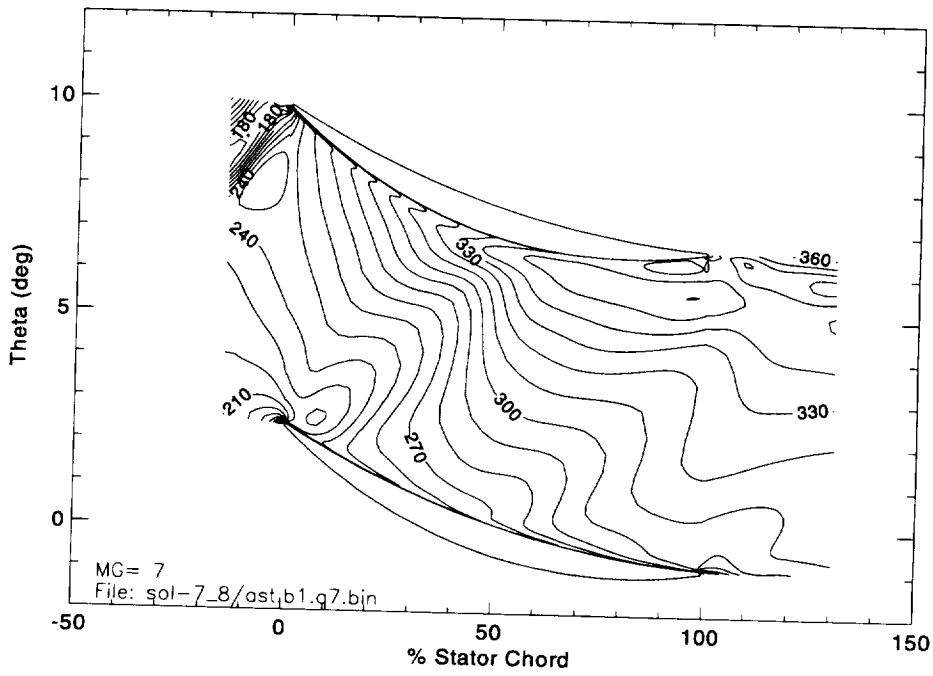

Figure 121. Relative velocity magnitude (m/s) for rotor position 14 of 15 for near stall MSU-TURBO simulation.

REFERENCES

Adamczyk, J. J., "Model Equation for Simulating Flows in Multistage Turbomachinery," ASME Paper No. 85-GT-226, 1985.

Adamczyk, J. J., "Wake Mixing in Axial Flow Compressors," ASME Paper No. 96-GT-029, 1996.

Adamczyk, J. J., Celestina, M. L., and Chen, Jen Ping, "Wake-Induced Unsteady Flows: Their Impact on Rotor Performance and Wake Rectification," Journal of Turbomachinery, Vol. 118, No. 1, 1996b, pp. 88-95.

Chen, J. P., Celestina, M. L., and Adamczyk, J. J., "A New Procedure for Simulating Unsteady Flows Through Turbomachinery Blade Passages," ASME Paper No. 94-GT-151, 1994.

Denton, J. D., "Loss Mechanisms in Turbomachines," Journal of Turbomachinery, Vol. 115, No. 4, 1993, pp. 621-656.

Denton, J. D., and Cumpsty, N. A., "Loss Mechanisms in Turbomachines," IMechE Paper No. C260/87, 1987.

Deregel, P. and Tan, C. S., "Impact of Rotor Wakes on Steady-State Axial Compressor Performance," ASME Paper No. 96-GT-253, 1996.

Ding, K., "Flow Measurements Using a Laser-Two-Focus Anemometer in a High-Speed Centrifugal and a Multistage Axial Compressor," presented at the Winter Annual Meeting of ASME, Phoenix, Arizona, November, 1982.

Dunker, R. J., "Flow Measurements in the Stator Row of a Single-Stage Transonic Axial-Flow Compressor with Controlled Diffusion Stator Blades", AGARD CP-351, Viscous Effects in Turbomachines, 1983.

Hathaway, M. D., "Unsteady Flows in a Single-Stage Transonic Axial-Flow Fan Stator Row," NASA TM 88929, December 1986.

Hathaway, M. D., Suder, K. L., Okiishi, T. H., Strazisar, A. J., and Adamczyk, J. J., "Measurements of the Unsteady Flow Field Within the Stator Row of a Transonic Axial-Flow Fan: II- Results and Discussion," ASME Paper No. 87-GT-227, 1987.

Hill, P. G., Schaub, U. W., and Senoo, Y., "Turbulent Wakes in Pressure Gradients," ASME

Journal of Applied Mechanics, December 1963, pp. 518-524.

Hobbs, D. E., Wagner, J. H., Dannenhoffer, J. F., and Dring, R. P., "Experimental Investigation of Cascade Wakes," ASME Paper No. 82-GT-299, 1982.

Kemp, N.H. and Sears, W.R., "On the Wake Energy of Moving Cascades," Journal of Applied Mechanics, June, 1956, pp. 262-268.

Kerrebrock, J. L. and Mikolajczak, A. A., "Intra-Stator Transport of Rotor Wakes and Its Effect on Compressor Performance," ASME Journal of Engineering for Power, October 1970, pp. 359-368.

Koch, C. C., and Smith, L. H. Jr., "Loss Sources and Magnitudes in Axial-Flow Compressors," Journal of Engineering for Power, July 1976, pp. 411-424.

Kool, P. and Hirsch, Ch., "A Prediction Scheme for the Decay of a Turbomachine Blade Wake," ASME Paper No. 82-GT-273, 1982.

Mikolajczak, A. A., "The Practical Importance of Unsteady Flow," in AGARD CP-177, *Unsteady Flow Phenomena in Turbomachinery*, 1975.

Nakayama, A., "Curvature and Pressure-Gradient Effects on a Small Defect Wake," Journal of Fluid Mechanics, Vol. 175, 1987, pp. 215-246.

Poensgen, C. and Gallus, H. E., "Three-Dimensional Wake Decay Inside of a Compressor Cascade and Its Influence on the Downstream Unsteady Flow Field," ASME Paper No. 90-GT-21, 1990.

Raj, R. and Lakshminarayana, B., "Characteristics of the Wake Behind a Cascade of Airfoils," Journal of Fluid Mechanics, Vol. 61, 1973, pp. 707-730.

Reid, L. and Moore, R. D., "Design and Overall Performance of Four Highly Loaded, High-Speed Inlet Stages for an Advanced High-Pressure-Ratio Core Compressor," NASA TP 1337, October 1978a.

Reid, L. and Moore, R. D., "Performance of Single-Stage Axial-Flow Transonic Compressor With Rotor and Stator Aspect Ratios of 1.19 and 1.26, Respectively, and with Design Pressure Ratio of 1.82," NASA TP 1338, November 1978b.

Schlichting, H., Boundary Layer Theory, McGraw Hill Publishing Company, New York, re-issue 1987.

Sherman, Frederick S., Viscous Flow, McGraw-Hill Publishing Company, New York, 1990.

Smith, L.H., "Secondary Flow in Axial-Flow Turbomachinery," ASME Transactions, Vol. 77,

No. 7, 1955.

Smith, L. H. Jr., "Wake Dispersion in Turbomachines," Journal of Basic Engineering, September 1966, pp. 688-690.

Smith, L. H. Jr., "Casing Boundary Layers in Multistage Axial-Flow Compressors," Flow Research in Blading, edited by L. S. Dzung, Elsevier Publishing Company, Amsterdam, 1970.

Smith, L. H. Jr., "Wake Ingestion Propulsion Benefit," Journal of Propulsion and Power, Vol. 9, No. 1, Jan.-Feb. 1993, pp. 74-82.

Smith, L. H. Jr., 1996 in, "Discussion of ASME Paper No. 96-GT-029: Wake Mixing in Axial Flow Compressors," 1996 ASME Turbo Expo, Birmingham, England, June 10-13.

Stauter, R. C., Dring, R. P., and Carta, F. O., "Temporally and Spatially Resolved Flow in a Two-Stage Axial Compressor: Part 1-Experiment," ASME Journal of Turbomachinery, Vol. 113, 1991, pp. 212-226.

Strazisar, A. J., Wood, J. R., Hathaway, M. D., and Suder, K. L., "Laser Anemometer Measurements in a Transonic Axial-Flow Fan Rotor," NASA TP 2879, November 1989.

Suder, K.L., "Experimental Investigation of the Flow Field in a Transonic, Axial Flow Compressor with Respect to the Development of Blockage and Loss," PhD Dissertation, Case Western Reserve University, Cleveland, OH, 1996.

Tweedt, D. L., Hathaway, M. D., and Okiishi, T. H., "Multistage Compressor Stator/Rotor Interaction," Journal of Propulsion, Vol. 1, No. 6, Nov-Dec., 1985, pp. 449-455.

Valkov, T. and Tan C. S., "Control of the Unsteady Flow in a Stator Blade Row Interacting with Upstream Moving Wakes," Journal of Turbomachinery, Vol. 117, No. 1, 1995, pp. 97-105.

Verhoff, V., "Three-Dimensional Laser Window Formation," NASA Reference Publication 1280, 1992.

Williams, M. C., "Inter and Intrablade Row Laser Velocimetry Studies of Gas Turbine Compressor Flows," ASME Journal of Turbomachinery, Vol. 110, July 1988, pp. 369-376.

REPORT DOCUMENTATION PAGE

Form Approved
OMB No. 0704-0188

Public reporting burden for this collection of information is estimated to average 1 hour per response, including the time for reviewing instructions, searching existing data sources, gathering and maintaining the data needed, and completing and reviewing the collection of information. Send comments regarding this burden estimate or any other aspect of this collection of information, including suggestions for reducing this burden, to Washington Headquarters Services, Directorate for Information Operations and Reports, 1215 Jefferson Davis Highway, Suite 1204, Arlington, VA 22202-4302, and to the Office of Management and Budget, Paperwork Reduction Project (0704-0188), Washington, DC 20503.

1. AGENCY USE ONLY (*Leave blank*)	2. REPORT DATE	3. REPORT TYPE AND DATES COVERED
	February 1998	Final Contractor Report

4. TITLE AND SUBTITLE

Study of a Wake Recovery Mechanism in a High-Speed Axial Compressor Stage

5. FUNDING NUMBERS

WU–523–26–33–00
NAG3–1302

6. AUTHOR(S)

Dale E. Van Zante

7. PERFORMING ORGANIZATION NAME(S) AND ADDRESS(ES)

Iowa State University
Ames, Iowa 50011

8. PERFORMING ORGANIZATION REPORT NUMBER

E–11045

9. SPONSORING/MONITORING AGENCY NAME(S) AND ADDRESS(ES)

National Aeronautics and Space Administration
Lewis Research Center
Cleveland, Ohio 44135–3191

10. SPONSORING/MONITORING AGENCY REPORT NUMBER

NASA CR—1998-206594

11. SUPPLEMENTARY NOTES

This report was submitted as a dissertation in partial fulfillment of the requirements for the degree Doctor of Philosophy to Iowa State University, Ames, Iowa 50011, 1997. Project manager, Kenneth L. Suder, Turbomachinery and Propulsion Systems Division, organization code 5810, (216) 433–5899.

12a. DISTRIBUTION/AVAILABILITY STATEMENT

Unclassified - Unlimited
Subject Categories: 07 and 34 Distribution: Nonstandard

This publication is available from the NASA Center for AeroSpace Information, (301) 621–0390.

12b. DISTRIBUTION CODE

13. ABSTRACT ***(Maximum 200 words)***

This work addresses the significant differences in compressor rotor wake mixing loss which exist in a stage environment relative to a rotor in isolation. The wake decay for a rotor in isolation is due solely to viscous dissipation which is an irreversible process and thus leads to a loss in both total pressure and efficiency. Rotor wake decay in the stage environment is due to both viscous mixing and the inviscid strain imposed on the wake fluid particles by the stator velocity field. This straining process, referred to by Smith (1993) as recovery, is reversible and for a 2D rotor wake leads to an inviscid reduction of the velocity deficit of the wake. A model for the rotor wake decay process is developed and used to quantify the viscous dissipation effects relative to those of inviscid wake stretching. The model is verified using laser anemometer measurements acquired in the wake of a transonic rotor operated in isolation and in a stage configuration at near peak efficiency and near stall operating conditions. Additional insight is provided by a time-accurate 3D Navier Stokes simulation of the compressor stator flow field at the corresponding stage loading levels. Results from the wake decay model exhibit good agreement with the experimental data. Data from the model, laser anemometer measurements, and numerical simulations indicate that for the rotor/stator spacing used in this work, which is typical of core compressors, rotor wake straining (stretching) is the primary decay process in the stator passage with viscous mixing playing only a minor role. The implications of these results on compressor stage design are discussed.

14. SUBJECT TERMS

Turbomachinery; Axial compressor

15. NUMBER OF PAGES

162

16. PRICE CODE

A08

17. SECURITY CLASSIFICATION OF REPORT	18. SECURITY CLASSIFICATION OF THIS PAGE	19. SECURITY CLASSIFICATION OF ABSTRACT	20. LIMITATION OF ABSTRACT
Unclassified	Unclassified	Unclassified	